The Permeation Behavior of Nanoparticles in Lipid Membranes

by

Changjiang Liu

A dissertation submitted in partial fulfillment
of the requirements for the degree of
Doctor of Philosophy
(Biophysics)
in the University of Michigan
2020

Doctoral Committee:

       Assistant Research Scientist, Paolo Elvati, Co-Chair
       Professor, Angela Violi, Co-Chair
       Assistant Professor, Jeremy Scott VanEpps
       Associate Professor, Sarah Veatch
       Assistant Professor, Kevin Wood

Changjiang Liu

desmliu@umich.edu

ORCID iD: 0000-0003-3272-0689

DEDICATION

This dissertation is dedicated to my family of Mr Liu, Wen and
Ms Huang, Xiaoyu and Ms Yu, Ketian.

ACKNOWLEDGMENTS

PREFACE

Starting from a new perspective of the interaction between nanoparticles and lipid membranes, I developed a systematic model for predicting the fate of nanoparticles once in contact with a lipid membrane. By factorizing the contribution from nanoparticles and lipid membranes, the model allowed the inclusion of data from multiple sources including experimental measurement, computational properties, and theoretical prediction, and can predict the time of entry of particles in the membrane at high confidence. The simplicity of the model allows also for fast screening of drug candidates for their bioavailability. The generality of the parameters in the model allows the application to various conditions, which were presented as examples in this thesis.

TABLE OF CONTENTS

Chapters

LIST OF FIGURES

LIST OF TABLES

LIST OF APPENDICES

APPENDIX

LIST OF ABBREVIATIONS

LDA low-density area

MD molecular dynamics

FEP free energy pertubation

NPs nanoparticles

GQD graphene quantum dot

DPPC 1,2-dipalmitoyl-sn-glycero-3-phosphocholine

DPPE 1,2-dipalmitoyl-sn-glycero-3-phosphoethanolamine

DPPS 1,2-dipalmitoyl-sn-glycero-3-phosphatidylserine

POPC 1-palmitoyl-2-oleoyl-sn-glycero-3-phosphatidylcholine

POPE 1-palmitoyl-2-oleoyl-sn-glycero-3-phosphatidylethanolamine

POPI 1-palmitoyl-2-oleoyl-sn-glycero-3-phosphatidylinositol

POPS 1-palmitoyl-2-oleoyl-sn-glycero-3-phosphatidylserine

PMCL2 1,2-dipalmitoyl-1'-palmytoil-2'-cis-9,10-methylenehexadecanoyl-cardiolipin

PVCL2 1,10-palmitoyl-2,20-vacenoyl-cardiolipin

PYPI 1-hexadecanoyl-2-hexadecenoyl-sn-glycero-3-phosphatidylinositol

PSM palmitoylsphingomyelin

Chl cholesterol

ABSTRACT

The number of engineered nanoparticles for applications in the biomedical arena has grown tremendously over the last years due to advances in the science of synthesis and characterization. For most applications, the crucial step is the transport through a physiological cellular membrane. However, the behavior of nanoparticles in a biological matrix is a very complex problem that depends not only on the type of nanoparticle, but also on its size, shape, phase, surface charge, chemical composition and agglomeration state. In this thesis, I introduce a streamlined theoretical model that predicts the average time of entry of nanoparticles in lipid membranes, using a combination of molecular dynamics simulations and statistical approaches. The uniqueness of the model lies in the ability to identify four parameters that separate the contributions of nanoparticle characteristics (*i.e.*, size, shape, solubility) from the membrane properties (density distribution and dynamics). This factorization allows the inclusion of data obtained from both experimental and computational sources, as well as a rapid estimation of large sets of permutations in membranes. The robustness of the model is supported by experiments carried out in lipid vesicles encapsulating graphene quantum dots as nanoparticles. The model is applied to the study of various nanoparticles, biological membranes (*i.e.*, mammalian cellular organelles, viral envelopes), and environmental conditions. Overall, this work contributes to the understanding and prediction of interactions between nanoparticles and lipid membranes, responding to the high level of interest across multiple areas of study in modulating intracellular targets, and the need to understand and improve the applications of nanoparticles and to assess their effect on human health (*i.e.*, cytotoxicity, bioavailability).

CHAPTER 1

Introduction

The transport of substances across lipid membranes is a biological process of great importance. Molecules that can readily cross cell membranes are frequently needed in biological research and medicine. Examples of permeable molecules that are useful for biological research include protein inhibitors, crosslinking molecules, indicators of ion concentrations, and various fluorescent dyes. In medicine, numerous drugs are small molecules acting on intracellular targets, and for most of the routes of administration, cell membrane permeation is required for a drug molecule to reach the cytoplasm of the cells.

In the case of small organic compounds, it is possible to tune their physicochemical characteristics to facilitate passage through the plasma membrane. Lipophilicity can be increased by avoiding the presence of ionizable groups, and the number of hydrogen-bonded donors can be reduced by N– or O–alkylation. However, this is not the case for most macromolecules, such as proteins or nanoparticles (NPs), whose hydrophilicity and large size hamper direct diffusion through the membrane lipid bilayer [65]. These limitations are especially frustrating in biomedicine. Indeed, recently there has been a blooming of applications in the biomedical arena due to advances in the science of synthesis and characterization of nanoscale engineered particles. Tunable geometric, optical, and surface properties of organic and inorganic nanomaterials enable engineering for several applications, such as drug delivery [44, 14, 88], controlled-release [14, 54], deep tissue imaging and sensing of cellular behavior [53, 82, 1, 52, 111].

NPs can be delivered by various entry routes, including oral administration [77, 29], vaccina-

tion [83], and aerosol-based drug delivery [19, 12, 5], depending on the therapeutic requirement. However, one of the crucial steps of NP uptake is transport across a physiological cellular membrane. The semipermeable nature of lipid membranes represents a selective barrier to passive diffusion and small apolar compounds can cross the membrane at appreciable rates. Passive selectivity arises from the forces and fluctuations present across the membrane environment and it is not actively regulated by the cell.

In general, cells do not permit access of polar macromolecules to their cytosol, and phospholipid membranes constitute an effective barrier. Nonetheless, over the years several systems have been reported to give cytoplasmic access to biomacromolecules, most notably cell-penetrating peptides [102], supercharged proteins [114, 78] and different types of NPs [56, 92, 89].

When discussing nanoparticles in biological membranes, it is critical to make some categorization based on the size of the particle relative to the typical scales of the membranes. For particles with the smallest dimension larger than the membrane thickness, approximately above $10-15\,\text{nm}$, the permeation is generally controlled by membrane deformation [22] and endocytosis [33]. Smaller nanoparticles can instead cross the membrane by passive transport, that is by displacing, sometimes irreversibly, the lipids or by diffusing in the hydrophobic region of the membrane and then on the other side. At the smaller end, below what is classified as a nanoparticle, small molecules (*e.g.*, oxygen or water) can cross the membrane by using the small free volume pockets that are generated as part of the normal thermal fluctuations [106]. Finally, while size plays an important role, the behavior of NPs in the biological matrix depends also on their type, shape, surface chemistry, chemical composition, and agglomeration state.

1.1 Existing models of membrane permeation and their limitations

1.1.1 Solubility-diffusion model

Over the years, several models have been proposed to describe the process of passive permeation of NP entering the cellular membrane, from the late 19*th* century solubility-diffusion model [71, 62] to its recent derivations such as triple-layer model [68], MD based approaches [84, 112, 73] and state-transition model [79]. The solubility-diffusion model, developed independently by Overton and Meyer, assumes the whole membrane as a homogeneous layer of hydrophobic hydrocarbons with a constant permeability, where the permeation process was described directly by the Fick's first law of diffusion as molecules move down concentration gradients. The seminal contribution of this model to biology is the recognition that the permeability of cells to many different solutes is proportional to the partition coefficients of the solute from water into organic phases [100]. More hydrophobic the solutes are, the more efficient it can partition into the membrane [59]. While this model has its advantage in terms of simplicity and it has been widely applied to the study of the permeation of small molecules, such as oxygen and water, it does not take into consideration the dynamic motion of the bilayer membrane structure [74] and lacks the inclusion of the variation of physical structure of the lipid bilayer. Overall, the agreement between the computed permeability and agrees with experiments for lipid bilayers is only in the orders of magnitude. Also, the bilayer thickness assumed by the model was often found in disagreement with experimental measurements, indicating that the computed mechanism of permeation was not a simple process of diffusion.

1.1.2 Improved solubility-diffusion model

A simple improvement to the solubility-diffusion model is the triple-layer model [68], that describes the mechanism of permeation using Fick's first law and considers the membrane as a

combination of homogeneous slabs, where a hydrophobic layer is embedded by two layers of hydrophilic ones. One can easily adapt different parameters of thickness, solubility, and diffusivity for the two types of layers for the variation of lipid compositions of different head groups and aliphatic chains and reach better accuracy for the prediction in the permeability for different lipid bilayers. Using modern computational power, one can approximate the lipid membrane with an even finer structure by increasing the number of layers [84, 112, 73] to approximate the diffusivity and solubility of the NP at different heights inside the membrane.

In summary, these methods, despite being successful in many applications, still lack in the consideration of 1) the dynamics of lipid packing which changes at different composition and environmental conditions [108, 61] and 2) the geometric shape of NPs [109], resulting in large prediction errors for particles of various sizes and shapes, membranes of different compositions, membranes being deformed by external forces, or when membrane phase-changes are involved. Also, the computational approaches are often limited by the geometric size of the NP. For large NP of complex geometry, it may take very long computational time to reach ergodicity for the membrane-NP system by sampling all the potential configurations of the NP in the membrane. Sometimes even with the implementation of some accelerated sampling techniques, such as umbrella sampling [90], Monte Carlo sampling [36], and Metadynamics [47], the system still incurs the curse of dimension of too many degrees of freedom that the system needs to sample.

1.1.3 Head-group gated model

Another group of studies present in the literature has focused on the molecular interactions between lipids and NPs from molecular level, as one of the main steps that control the permeation barrier [66, 7, 112]. This head-group gating effect was theoretically studied by Xiang *et al.* [109, 108], where the concept of free surface area mediating the permeation was suggested for the first time. The article also suggested an empirical distribution of the free surface areas of an exponential shape, and mentioned that barrier of permeation being related to the permeate size. Vamparys *et al.* provided molecular insights into multiple definitions of the free surface area as well as the the area

distribution [94] and found the exponential distribution from statistics. By studying lipid packing from molecular level, the model enabled the estimation of the effect of various types of lipids in the membranes, membrane phase changes, and external forces that were applied to the membrane. While promising, the free surface area model, is still hard to apply as it has several critical shortcomings. For example, the shape of NP was not considered for the permeation. These models had no bias against two NPs of the same weight but different geometric shapes. However, in the permeation process, the one with a smaller cross-sectional area are often preferred [51]. Also, these studies on the free surface areas didn't discusse the lifetime distributions of the free surface areas, resulting in a gap between the static distribution to the kinetics of the permeation process.

1.1.4   Empirical models

Beyond these models on passive permeation, there are also models and approaches to discussing the effect of forming transient pore, lipid flip, and permeation assisted by membrane channels [59]. However, these processes are either too slow or too specific. In practice, there are also some empirical models being developed with no prior knowledge of the physical mechanism of permeation, such as the most commonly used "rule of five" [50] and some QSAR/QSPR models [26, 110, 32]. However, the predicted permeability is only accurate to the order of magnitude. Sources contributing to the error of QSAR include 1) the incorporation of too many descriptors that are not related to the permeation problem, and 2) strong dependency on the quality (extensiveness and consistency) of the training set.

1.2   Overview of the LDA model

In this thesis, I present a theoretical model that is able to predict the average time of permeation of NPs through the hydrophilic region of a lipid membrane, using a combination of molecular dynamics (MD) and ad hoc analysis. The major contributions of this work are the identification of four parameters to describe the permeation process and the factorization of the contributions

that are only dependent on the characteristics of NPs (*e.g.*, size, shape), properties of the lipid membrane (*e.g.*, free surface area) from the ones that depend on both (solubility). This separation has two main benefits: it allows the use of data obtained from both experimental (*e.g.*, partition coefficients, NPs' shape measures) and computational sources (membrane surface dynamics) as they become available, and it makes possible a rapid estimation of large sets of systems by using existing data. This model is validated using both experimental data collected in systems composed of vesicles and NPs, as well as all-atom MD simulations, obtaining in all cases agreement well within measurement error. The model is interested across multiple areas of study in modulating intracellular targets, evaluating the effect of NP on human health (*i.e.*, cytotoxicity, bioavailability), and in the early phases of drug discovery for screening drugs of inefficient permeation.

The following chapters are organized as follows: Chapter 2 describes the development of the low-density-area (LDA) model as applied to rigid NPs entering phosphatidylcholine membranes, in Chapter 3 the LDA model is extended to consider various biological membranes and nanoparticles with a flexible shape. Chapter 4 introduce another type of biological membrane, the coronavirus envelope, and the LDA model is then applied to the permeation of a variety of drugs through the viral membrane. The final chapter reports the details of the molecular dynamics simulations used to develop the LDA model and information on how the biological membranes and transmembrane protein were modeled in this study.

CHAPTER 2

Development of LDA Model for Membrane Permeation

In this chapter, I present the observation of the low-density areas in simulation and its role in the NP permeation process. Based on the correlation, I developed a physical model of permeation that factorized the contribution of the NP and membranes. The metrics of the low-density areas is then compared to the similar concepts in literature in Section 2.3. In the last section of this chapter, I present the validations of the model based on experimentally measured leakage of NP through lipid vesicles, and the time of entry of NP in lipid membranes collected from unbiased MD simulations.
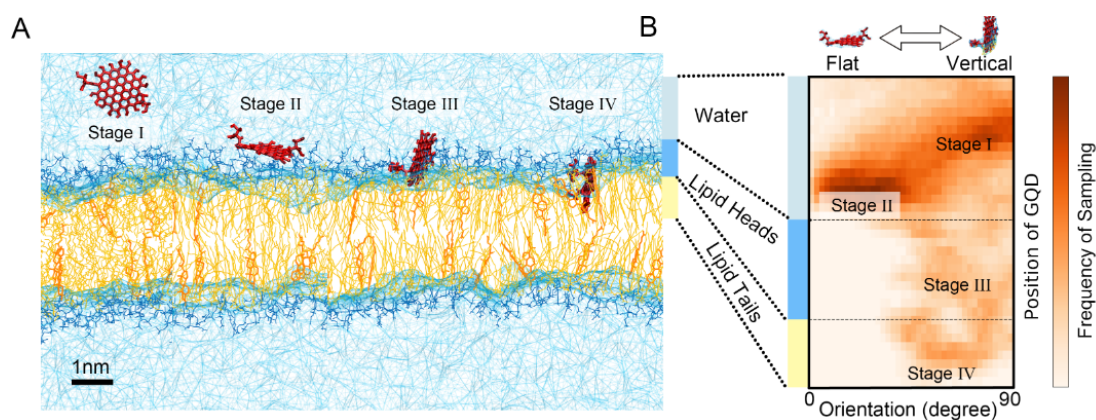
Figure 2.1: Permeation of a 2-nm cys-GQD in a lipid bilayer. The process can be separated in four phases (A), in which position and orientation of the permeant strongly correlate (B).

2.1 Low-density areas are related to the permeation of NP in simulation

To identify trends in membrane permeation that can be used for our model, I performed several independent MD simulations of different NPs in a 1-palmitoyl-2-oleoyl-sn-glycero-3-phosphatidylcholine (POPC)/cholesterol (Chl) bilayer (10:1 concentration ratio). The ratio represents the typical composition of a mammalian cellular membrane [96].

As for NPs, I focused our study on carbonaceous NPs since they have been widely utilized in many health-related fields like drug delivery [44, 14, 88], cancer therapy [14, 54], wound disinfection [85], biolabeling [53, 82, 1] and biosensing [52, 111], due to their low cytotoxicity, high photoluminescence and easy surface functionalization. Specifically, a buckminsterfullerene, a curved OH-terminated GQD and GQD functionalized with two cysteine groups (cys-GQD) were used [86]. This selection covers NPs of similar size, but different shape and hydrophilicity.

Analysis of MD trajectories shows that the process of permeation can be divided in four stages, summarized in Figure 2.1A,B: **I.** The NP reaches the membrane surface *via* diffusion. **II.** The NP diffuses over the water-membrane interface. **III.** The NP enters the hydrophilic region of the lipid bilayer. **IV.** The NP permeates the hydrophobic region of the lipid bilayer. These stages are not strictly sequential. For example, from Stage II, the NP can go to either Stage I or III, or, depending on the NP's properties, Stage II or III may be a long-lived state that does not further evolve in a given time frame.

The first transition (from Stage I to Stage II) is controlled in most conditions by the diffusion of the NP in the environment close to the membrane surface, due to the presence of an unstirred layer [4]. As this environment can be strongly affected by the species (*e.g.*, proteins and saccharides) that surround many biological membranes, and it is largely independent of the bilayer composition, I decided to restrict the focus of our model to the other transitions.

When analyzing the progress from Stage II to Stage III, I consistently observed a drop in the membrane surface density in the proximity of the particle (Figure 2.2, Figure 2.3 and Figure 2.4).
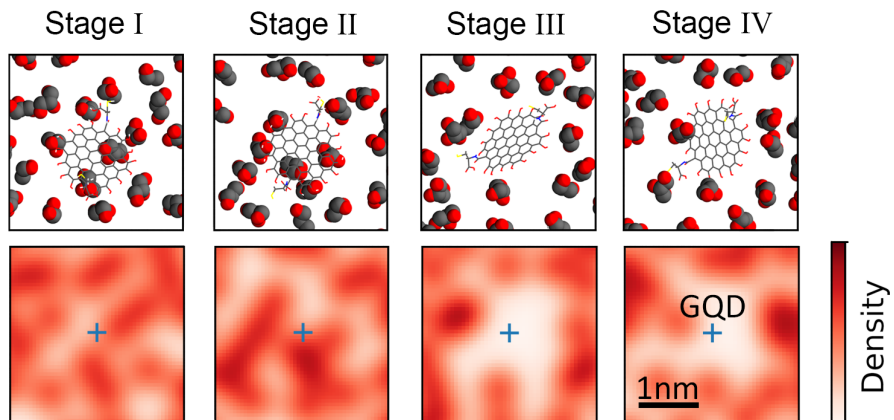
Figure 2.2: Lipid head-groups positions and surface lipid density show the LDA in the lipid-head region formed around the GQD during stage III.
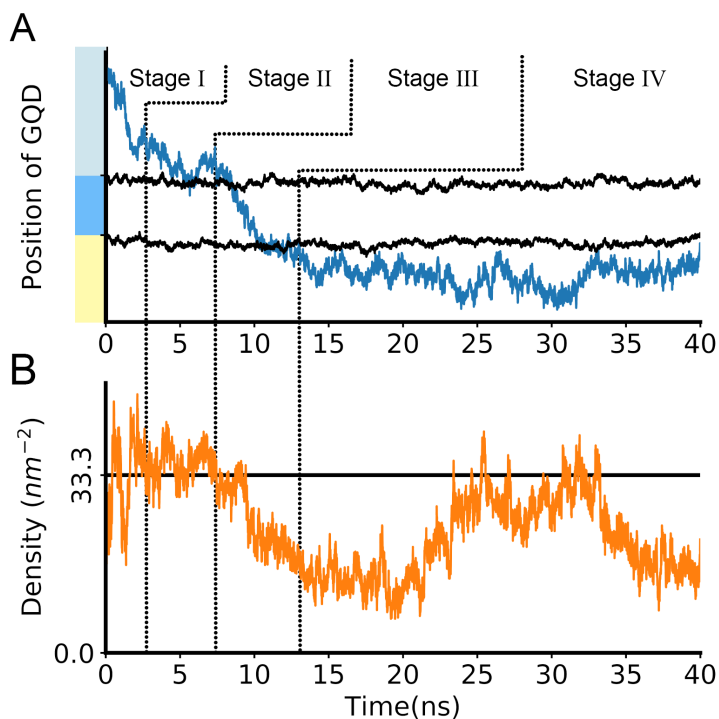
Figure 2.3: The time evolution of the cys-GQD distance from the membrane central plane (A) with the average atomic density of the membrane surface around the GQD (B).

At the same time, for non-spherical NPs (*e.g.*, cys-GQD), the transition is characterized by a change in the orientation of the NP, namely from parallel to perpendicular to the membrane plane (Figure 2.1B), in agreement with previous works [86, 91, 11]. In order to determine whether the
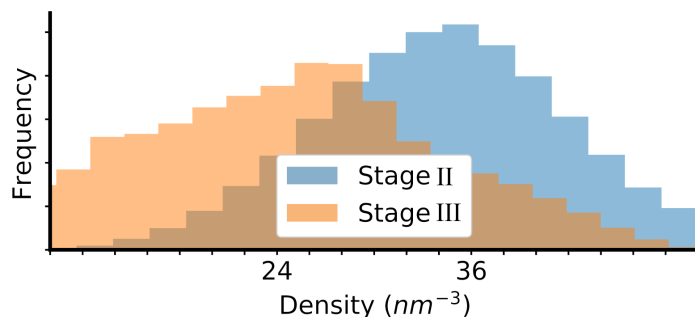
Figure 2.4: The average distribution of the density around GQD during stage II and stage III.

decrease in local density of the membrane surface was caused by the presence of NPs, I computed the membrane density distribution and dynamics both in absence and presence (close proximity) of NPs.
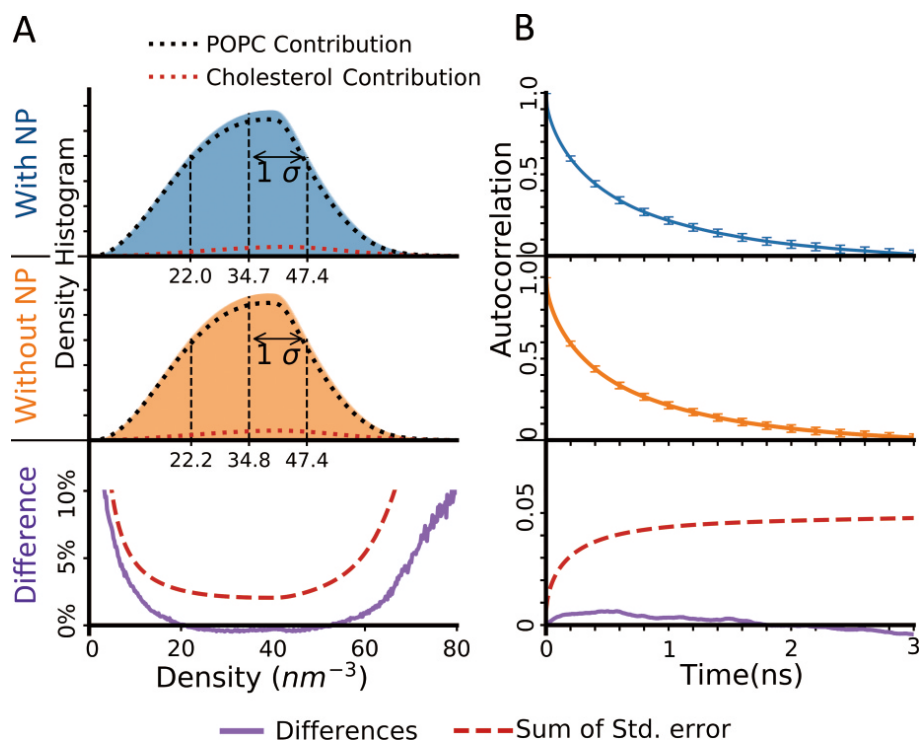
Figure 2.5: Effect of the presence of NPs (three different NPs, see text for details) on a POPC/cholesterol (ratio 10:1) bilayer density. Error bars (95 % confidence interval) shown only for selected points for clarity.

The result (Figure 2.5) shows that neither the density distribution nor the autocorrelation is significantly affected by the presence of the NPs selected in this work, as the difference between

the curves (purple) is always smaller than the standard error (dashed, red). This result suggests that the local change in density is due to the internal dynamics of the lipid bilayer, *e.g.*, thermal fluctuations. It is important to note that I do not exclude that different NPs can affect the local membrane density, most likely if strong Coulombic interactions are present. This is the case for compounds like graphene oxide nanosheets and a wide variety of cationic NPs, which are known to induce pore formation, membrane thinning and membrane erosion [91, 22, 113, 48]. However, as I will show below, the effect on permeation due to induced membrane changes can be modeled as a subset of the more complex case of fluctuations driven density changes that I observed.

2.2 Permeation model based on low-density areas

Based on the insights gained from MD simulations illustrated above, I developed a simplified model for the permeation of nanoparticles in biological membranes. The model describes the permeation as a gated entry model, in which the single process is regulated by the chance of the NP to encounter low-density areas (LDAs) on the membrane surface and by the solubility of the NP in the hydrophobic phase. Once the NP reaches the membrane surface, the process can be summarized as follows (Figure 2.6):

1. The NP that is in proximity of the membrane surface may encounter a local LDA of lipids with the right shape to allow the NP to permeate, with a probability P_{LDA}. P_{LDA} is generally dependent only on the membrane properties (*e.g.*, composition, surface tension). For NPs that perturb the local density, this probability should be modified.

2. If the LDA is large enough to allow NP permeation, the process is now controlled by its affinity with the lipid tails, P_T.

3. If permeation does not occur, the NP can leave the membrane surface or stay in proximity of the membrane long enough for a new independent "permeation attempt" (two previous steps) to occur. To approximate the time elapsed between two independent permeation attempts, here I use the LDA decorrelation time, τ_{LDA}, during which the thermal fluctuations generate

11
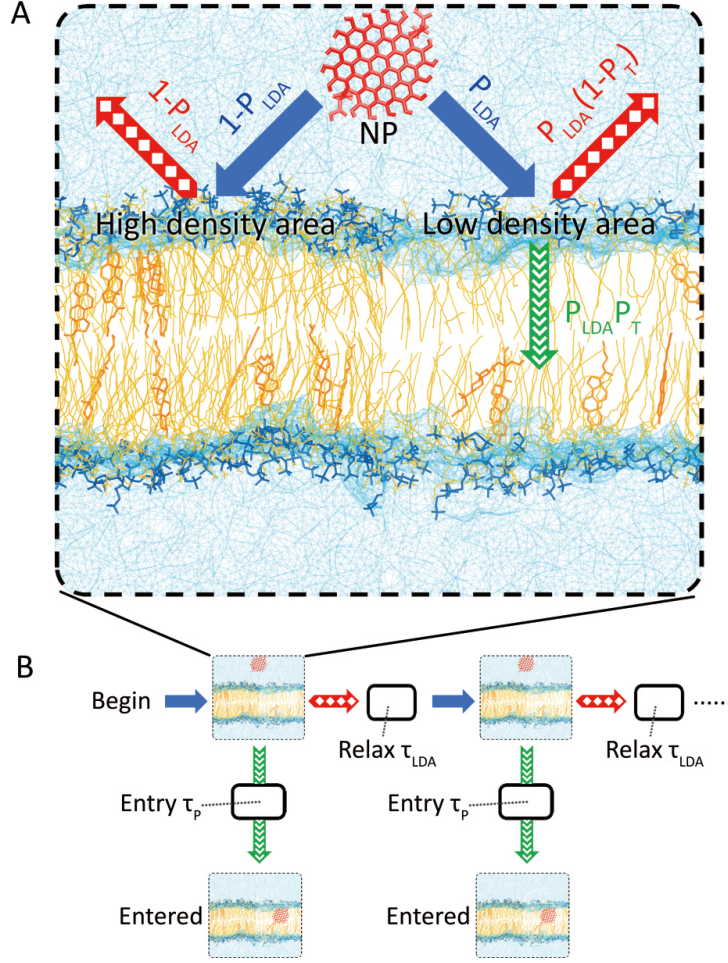
Figure 2.6: Schematic representation of the proposed permeation model. (A) The probability of entry controlled by P_{LDA} and P_T. (B) The diagram of time evolution. See text for the detailed description.

a new decorrelated distribution of LDAs on the membrane. Moreover, if I assume a condition of steady state, the probability of a NP diffusing away from the membrane is the same as the ones of a different NP reaching the membrane.

Based on this description, the average time of entry t_{entry} can be estimated as:

$$t_{entry} = \sum_{n=0}^{\infty}[(1-P)^n P(\tau_p + n\tau_{LDA})]$$
$$= \tau_p + \tau_{LDA}\frac{1-P}{P} \tag{2.1}$$

where τ_p is the average time for the NP to diffuse from the lipid head region to the lipid tail region

12

and P is the probability defined as:

$$P = P_T \cdot P_{LDA} \tag{2.2}$$

Below I discuss in detail all the four parameters reported in Eq. 2.1 and Eq. 2.2.

2.2.1 Thermodynamic probability (P_T)

The affinity of a particle with the lipid tail P_T describes the probability of the NP to move from the hydrophilic (headgroups region) to the hydrophobic phase. This factor is therefore related to the solubility of the NP in the membrane and can be estimated using the partition coefficient K_D of the NP in water/lipid as:

$$P_T = \frac{K_D}{1 + K_D} \tag{2.3}$$

This term agrees with the observed strong correlation between the permeability of NP in different biological membranes and the NP water/membrane partition coefficient [112, 70, 104].

K_D can be obtained from both computational and experimental techniques or approximating with a simpler system, *e.g.*, the water/octanol partition coefficient. Multiple theoretical models have been proposed to estimate the water/octanol partition coefficient. For example, Garrido *et al.* [28] used MD simulations to determine the temperature-dependent partition coefficients of different *n*-alkanes obtaining a good agreement with experimental values. Theoretical methods that do not require simulations [67, 63] can also be used to predict the partition coefficient using only the atomistic and structural information of a particle.

2.2.2 LDA probability (P_{LDA}).

P_{LDA} is the probability of finding an LDA of a given size and it is affected by both the properties of NP and membrane. However, for NPs that do not markedly alter the membrane surface dynamics, the contributions of membrane and NP can be separated and the P_{LDA} can be computed from the size and shape distributions of the LDA in the membrane and the size and shape of the NP, as described below.
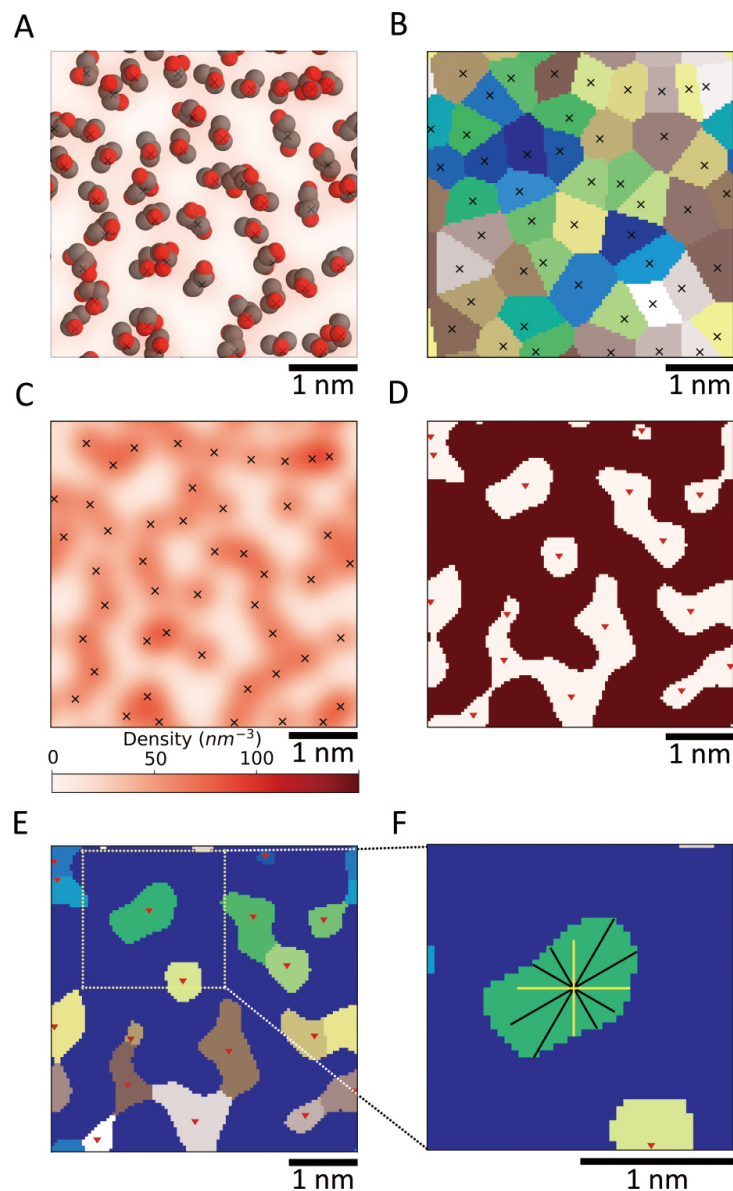
Figure 2.7: Schematic representation of the steps used in the analysis of the lipid density for each sample of the POPC:cholesterol (ratio of 10:1) bilayer (top-down view). See methodology for additional details. (A) Calculation of lipids' COM; atoms at the lipid/water interface are selected to locate the center of mass for each lipid. (B) Voronoi segmentation; crosses show lipids' COM. (C) Continuous density map obtained by applying a Gaussian function centered at each lipid COM. (D) Regions with a density above (light red) and below (dark red) the average water density ($33\,\text{nm}^3$ excluding hydrogen atoms). Down triangles indicate the local density minima. (E) Segmentation of joint LDAs by watershed by flooding on the density contour. (F) Dimensions probing of a single LDA, by sampling on perpendicular directions (*e.g.*, yellow lines) passing through the LDA minimum (only 3 pairs are shown for clarity).

14
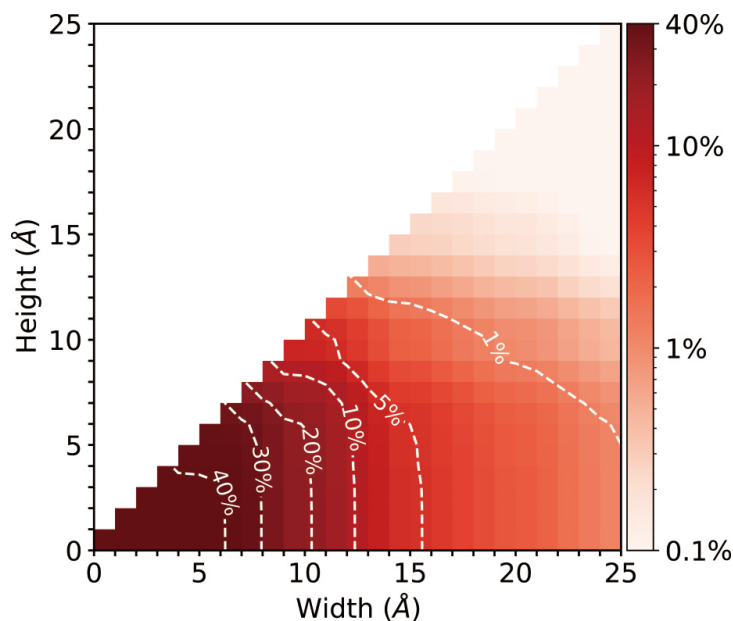
Figure 2.8: Average probability of finding an LDA larger than a given rectangular cross-section, shown as the cumulative histogram in a POPC/cholesterol (10:1) membrane.

The distributions of low-density areas can be computed in different ways, and below I propose an approach that can be extended potentially to experimental techniques, by converting atomistic three-dimensional information to two-dimensional images, which in turn are used to compute the properties of low-density areas. Next, I illustrate all the steps of the procedure by using data from an MD simulation of a POPC:cholesterol (10:1) bilayer at the physiological ionic concentration $(0.15\,\text{M NaCl})$.

For each sample of our simulation, I located the center of mass (COM) of each lipid by considering only the atoms at the water interface (Figure 2.7A). The membrane surface is then segmented using the positions of the COM to build a Voronoi diagram (Figure 2.7B). This partition makes it possible to determine the average area "occupied" by each lipid type under the specific environmental conditions and membrane composition. To obtain a continuous density map, I summed the two-dimensional Gaussian functions centered at the COM of each lipid with a radius dependent on the average membrane area for that type of molecule, *e.g.*, cholesterol, POPC (Figure 2.7C). With these steps, I have transformed the three-dimensional information from atomistic simulations to a continuous two-dimensional density map of the water/membrane interface, similar to the one

that can be obtained from different imaging techniques. Therefore, the following steps can be in general applied to any two-dimensional density map independently from its source.

The next step is to extract the statistics of LDAs' morphology from the two-dimensional density map. I first assign the center of all the LDAs to the local minima in the two-dimensional density (Figure 2.7C); the LDAs are then extended from these centers to the contour line corresponding to the density of water, *i.e.*, $33 \, \text{nm}^3$ (Figure 2.7D). Finally, joint LDAs are separated by a flooding watershed algorithm [103] (Figure 2.7E).

As shown in Figure 2.7E, the shapes of LDAs produced from the segmentation method, described above, are often irregular. To describe these shapes, I draw perpendicular lines starting from the local minimum at 18 different angles (Figure 2.7F). The lengths of these perpendicular lines are then used as descriptors of the shape and size of an LDA. Specifically, these dimensions can also be used as a filter for the size of the permeating particle.

The average filter over all the angles is computed for each LDA and then weighted by the LDA area. The result, normalized by the total membrane area, gives the size-dependent permeation probability for the given two-dimensional density map. Finally, the average over all the samples (*i.e.*, the MD trajectory) gives P_{LDA} as a function of the particle dimensions. One example is shown in Figure 2.8.

To account for the different possible orientations of a particle, I considered a cross-section along the 6 directions defined by the axes of inertia of the particle. To eliminate artifacts due to barbed or oddly-shaped objects, the cross-section was taken $0.28 \, \text{nm}$ from the particle surface, roughly the thickness of one water layer, and then approximated by its circumscribing rectangle. Finally, the sizes of the rectangles are used to compute six values of P_{LDA} that, as an average, represent the overall particle P_{LDA} and can also be used to estimate the preferential orientation during permeation.
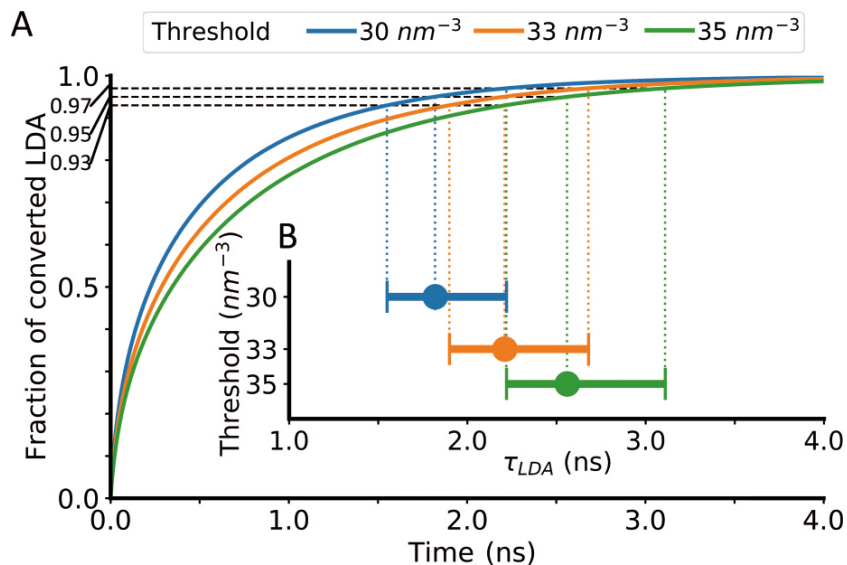
Figure 2.9: Estimated lifetime of LDA, based on the (A) fraction of LDAs that converts to non-LDA over time. (B) τ_{LDA} computed for different thresholds, for 95% LDA lifetime (bar indicate the 93-97% interval).

2.2.3 LDA decorrelation time (τ_{LDA})

As the next step, in order for the model to describe the dynamics of the membrane, I included knowledge on the time evolution of the LDAs. τ_{LDA} is the average time that the membrane surface density takes to decorrelate, which is controlled only by the membrane thermal and pressure fluctuations, under the non-interacting case discussed above. I estimated τ_{LDA} using the thresholded two-dimensional density map (*e.g.*, Figure 2.7D), and measured the shortest time of part of the LDA to transition to a non-LDA. As a measure of the decorrelation, I approximated τ_{LDA} as the characteristic time needed for the 95% conversion from LDA to non-LDA.

Figure 2.9 shows the distribution of the lifetimes and τ_{LDA} for three different surface density thresholds. While there are differences in the curves depending on the threshold value, once a 93-97% conversion interval is considered, taken into account the different sources of error, the results are substantially similar, approaching values close to $2\,\text{ns}$.

In this work, τ_{LDA} is extracted from surface density maps, but it can be derived also from theoretical models or experimental measurements of the fluctuations of the membrane surface [75, 9]. An intuitive comparison of the order of magnitude of the lifetime of LDA to membrane lipid

dynamics is lipid wobble (ns), axial rotation (ns), and lateral diffusion (ns to ms).

2.2.4 Time of permeation (τ_P)

τ_P is the average time that takes the NP to permeate from the lipid heads to the lipid tails when no barrier is encountered. This time usually provides a small contribution to the overall time of entry as compared to τ_{LDA}, as the permeation is limited by the head groups. Numerically τ_P can be approximated based on the diffusion velocity of the NP, or estimated from the size and mass of the NP [37]. However, in the extreme condition of NP being extended in one dimension, such as carbon nanotube and peptide of a long alpha-helical structure, their time of entry can be dominated by this time of permeation, as the particle can easily find an LDA that matches its tip, but the slow speed of diffusion and long length along its longest dimension make the entry extremely slow.

In this work I used the time difference between the formation of an LDA and the entry of the NP obtained from MD trajectories. This approach leads to values approximately between $1\,\mathrm{ns}$ for C60 to $3\,\mathrm{ns}$ for cys-GQD (refer to Figure A.18, Figure A.19, and Figure A.20).

2.3 Comparison between low-density areas and similar concepts in literature

To further explain the concept of LDAs, I compare the LDAs introduced in our model to similar metrics introduced by other researchers. For example, the accessibility surface area presented by Cui *et al.* [17] uses a sphere to probe the voids on the membrane surface [17]. The packing defect introduced by Vamparys *et al.* [94]) calculates the void by projecting the membrane surface to a grid. The metrics of the packing defect were further validated with experiments by using small molecules to probe the existence of the defects [3]. Essentially, these metrics, including the one reported in this article, speak to the atomic density on the membrane surface, which reflects the tightness of lipid packing at the hydrophilic/hydrophobic interface of lipid bilayers.

In the work done by Vamparys *et al.* [94], these metrics are compared accordingly to their
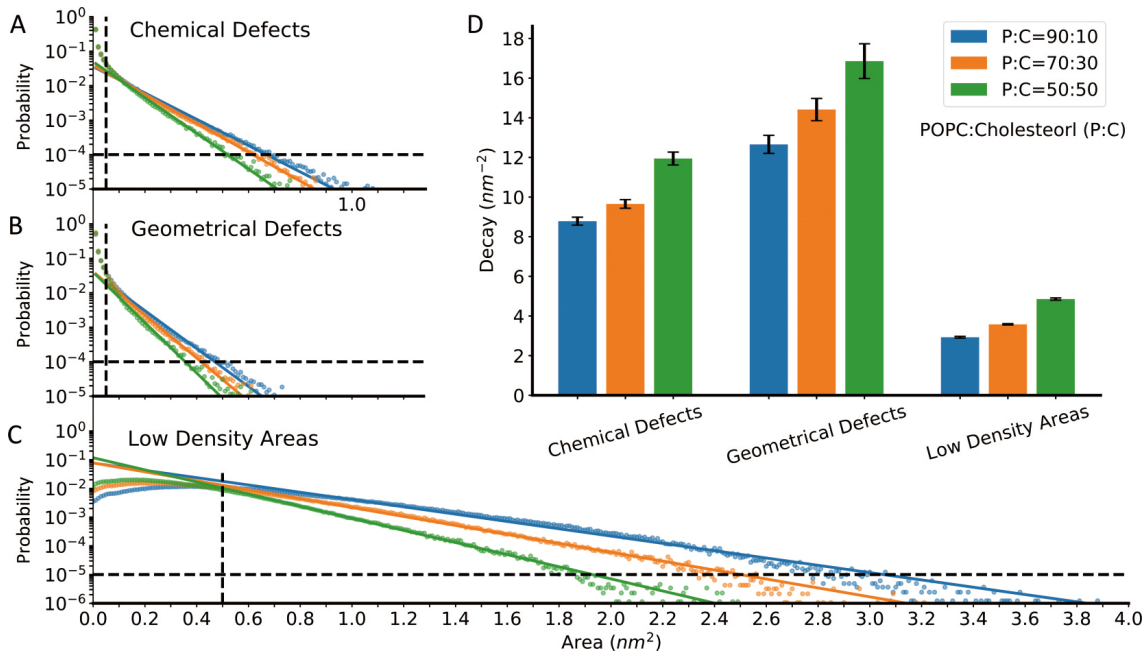
Figure 2.10: Size distribution of packing defects and LDAs in model membranes. The distribution is the probability of finding a defect area or LDA of defined size. Panel (A, B) are for the chemical defects and geometrical defects introduced by Vamparys *et al.* [94] and panel (C) for LDAs introduced in this work. For each metric, I analyze three types of membrane varying in their composition (ratio of POPC:cholesterol). Colors blue represent the POPC:cholesterol=90:10, orange for 70:30, and green for 50:50. Dots represent each sample and solid lines show the exponential function fit. Following the same approach as the original work by Vamparys *et al.* [94], to fit the exponential function for the distribution of the two types of packing defects, I selected only defects larger than $0.05\,\mathrm{nm}^2$ and with probability greater than 10^{-4}. For LDAs, this range of selection is for an area larger than $0.5\,\mathrm{nm}^2$ and with probability greater than 10^{-5}. The black dashed lines in panel (A, B, C) indicate such ranges of selection. Panel (D) compares the exponential decay constants for all the membranes and all the metrics.

distributions of the sizes of defect areas. The results showed that for all these metrics, 1) the sizes of defect areas increase when packing defects are introduced into the lipid bilayer, and 2) the distributions of the sizes of defect areas are roughly exponential.

To assess the similarity between LDA and defect area, in the following I compute the chemical and geometrical defects for three different membranes varying their POPC/cholesterol ratios, following the approach introduced by Vamparys *et al.* [94]. Analyses were performed on 2500 snapshots from 50 ns simulation for each membrane as shown in Figure 2.10. For all lipid compositions, I observed the exponential decay in size for all the distributions, above a minimal size ($0.05\,\mathrm{nm}^2$ for defects, $0.5\,\mathrm{nm}^2$ for LDA) similar to the results presented in the original work [94]. This decay

increases with the amount of cholesterol in the membrane, implying that the cholesterol facilitates the lipid packing in the bilayer, resulting in less packing defects on the membrane surface, in agreement with previous works [2, 42, 72, 43]. These similarities indicate that the metric of LDAs captures similar membrane surface properties as the metrics of packing defects do.

However, the data in Figure 2.10 highlights also some of the differences between these definitions. The most important one is the shape of the curve approaching zero: while the packing defects monotonically decrease as the defect size increases, the LDA distribution shows a maximum of around approximately $0.5\,\mathrm{nm}^2$. The reason for this difference lays in the physical meaning of LDA, namely the free energy cost associated with the membrane density fluctuations. On one hand, any deviation from the average density is not entropically favored. On the other hand, the fluctuations are enthalpically favored for small changes, as the average lipid-lipid distance becomes closer to the one associated with the potential energy minimum, but it then becomes also unfavorable once the repulsive part of the lipid-lipid interactions become prominent. Finally, the typical size of the LDA is about three times larger than the packing defects. This difference is intrinsic in their different definitions, as the packing defects are measuring the voids between atoms, which is a much stricter requirement than the one employed for LDAs that is defined based on density threshold.

2.4   Validation of the LDA model

Table 2.1: Parameters related to the model's prediction for the three NPs.

	τ_P	τ_{LDA}	P_T[1]	P_{LDA}	t_{entry}	$t_{entry,MD}$	$SE_{t_{entry,MD}}$
C60	$1\,\mathrm{ns}$	$2.2\,\mathrm{ns}$	100%	7.91%	$26.0\,\mathrm{ns}$	$26.1\,\mathrm{ns}$	$2.2\,\mathrm{ns}$
Curved-GQD	$1\,\mathrm{ns}$	$2.2\,\mathrm{ns}$	100%	6.39%	$33.2\,\mathrm{ns}$	$33.3\,\mathrm{ns}$	$3.2\,\mathrm{ns}$
Cys-GQD	$1\,\mathrm{ns}$	$2.2\,\mathrm{ns}$	100%	5.41%	$39.5\,\mathrm{ns}$	$39.6\,\mathrm{ns}$	$3.0\,\mathrm{ns}$

[1] K_D is estimated by using the approach outline in [67].

To test the performance of this model, I carried out two comparisons: the first one against statistical observations of all-atom MD simulations, the second *versus* experiments. As currently only
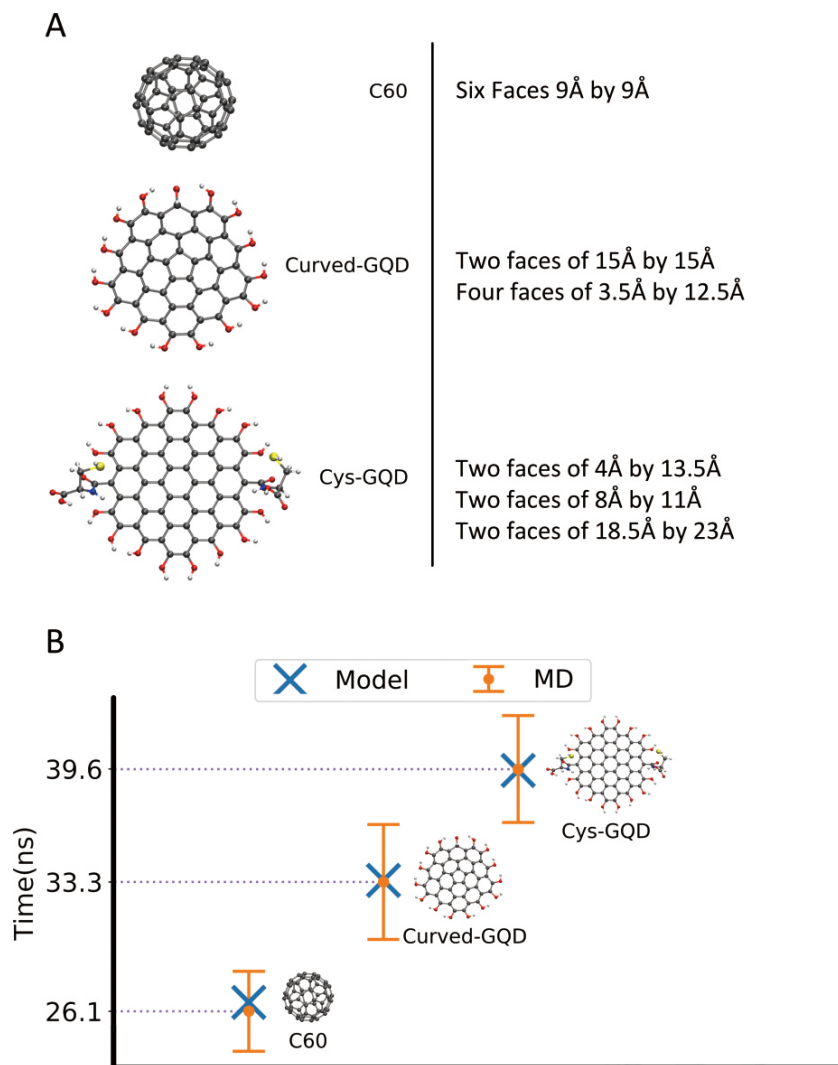
Figure 2.11: Comparison of the average time of permeation predicted from MD simulations and the current model.

P_T is estimated from experimental values, the first comparison establishes the ability of the model to capture the MD process independently of the approximations and simplifications introduced above.

To obtain the times of entry of three different NPs (Figure 2.11 A), I placed the NPs in close proximity of the POPC/cholesterol bilayer (10:1 ratio) while immersed in a NaClsolution at physiological conditions $(0.15\,\mathrm{M})$, and analyzed the results of multiple simulations (between 12 and 16 simulations). The times of entry were collected and fit with an exponential function from which the characteristic time was determined as the average time of entry. The quality of the fit can be

evaluated by the standard error of the time of entry (*via* its Fisher information). The average time of entry and the standard error are listed in Table 2.1, along with other parameters used in the model.

The results are reported in Figure 2.11, which shows that the agreement between the MD and the current model is within 10%. It is worth noting that all the 3 predictions seem to suffer from a negative bias error of about $0.1\,\text{ns}$. Since this term is consistent for all NPs, I attributed that to the factors that depend solely on the membrane, *i.e.*, τ_{LDA}.

Table 2.2: Parameters related to the model's prediction for the three membranes.

P:C	τ_P	τ_{LDA}	P_T	P_{LDA}	t_{entry}
50:50	$1\,\text{ns}$	$0.84\,\text{ns}$	1	$1.6\ 10^{-4}$	$5.2\,\mu\text{s}$
70:30	$1\,\text{ns}$	$1.2\,\text{ns}$	1	$1.1\ 10^{-3}$	$1.0\,\mu\text{s}$
90:10	$1\,\text{ns}$	$1.7\,\text{ns}$	1	$5.0\ 10^{-3}$	$0.31\,\mu\text{s}$

Given the overall excellent agreement between the MD results and the model, I further tested model predictions with experimental measurements of a photoluminescent NP crossing the membrane of lipid vesicles of different compositions. Specifically, I leveraged the linearity of the photoluminescence intensity of a GQD solution with its concentration, by monitoring the decrease in the luminescence of a GQD solution encapsulated in different vesicles, as a measurement of GQD leakage. The lipid vesicles encapsulating with GQD ($0.1\,\text{mM}$), with three different POPC/cholesterol ratios (*i.e.*, 50:50, 70:30 and 90:10), and GQD ranging from 2 nm to 8 nm in diameter, were prepared by double emulsion templated vesicles [58]. Next, the lipid vesicles were moved to a GQD-free solution and the GQD leakage was measured by monitoring the decrease of the photoluminescence of a single lipid vesicle over a one-hour period (Figure 2.12A) from the time the vesicle was moved to a GQD-free solution. Of note, I chose GQD that have a negligible tendency to aggregate, to simplify the interpretation of the experiments. The results, presented in Figure 2.12A,B are the average over 10 independent vesicles.

The kinetic of the GQDs' leakage in a spherical vesicle can be modeled by a first-order dynam-
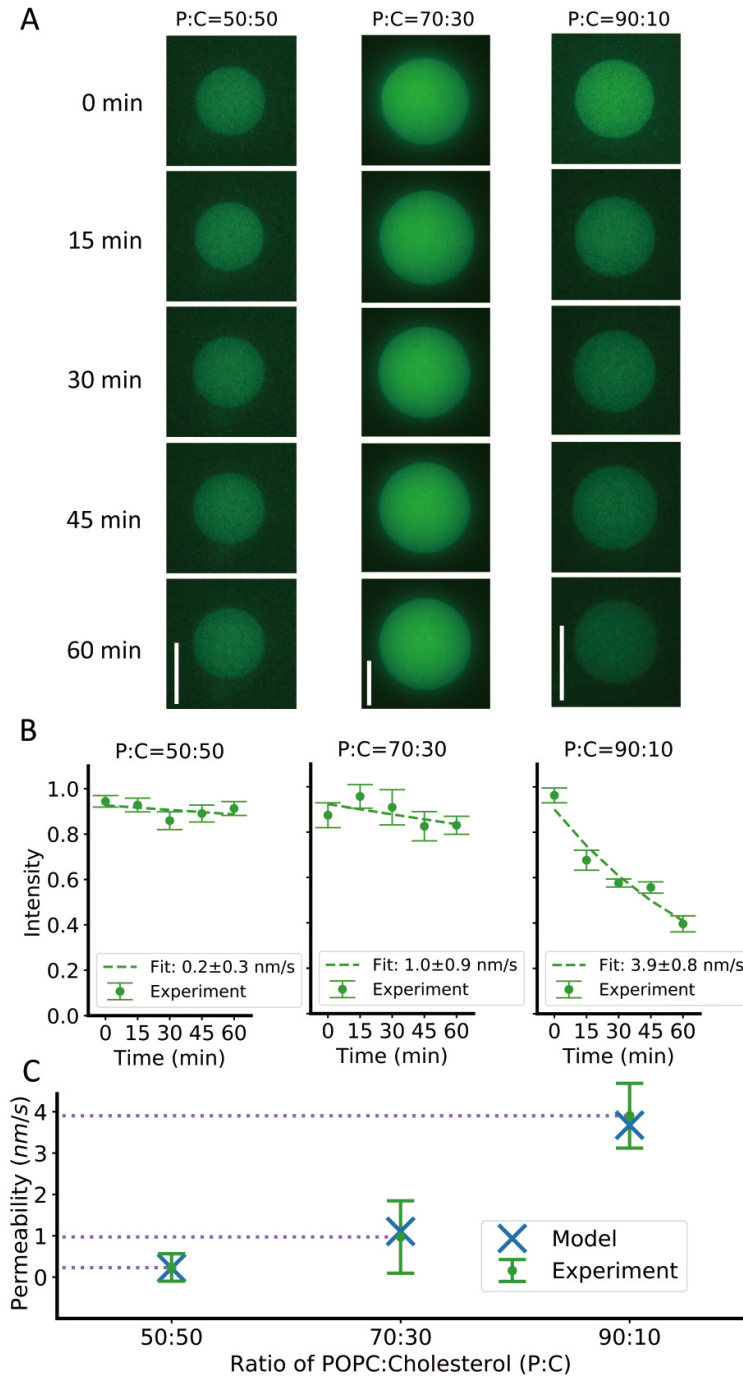
Figure 2.12: Measured GQD leakage from different lipid vesicles. (A) Experimental images of photoluminescence change over a one-hour period. Images were taken every 15 minutes. White scale bar for $50\,\mu\text{m}$. (B) The photoluminescence intensity over one-hour period for GQD encapsulated vesicles with different lipid compositions is indicated. (C) Comparison of the model's predictions to the permeability measured from experiment. (Error bars correspond to one standard deviation.) Experiments credited to Dr. Sagardip Majumder and Prof. Allen Liu.

ics as

$$I(t) = I(0) \exp\left(-\frac{3P}{r}t\right) \tag{2.4}$$

where $I(t)$ is the intensity of the fluorescence over time, P is the permeability of the membrane, r is the radius of the lipid vesicle. I modeled the leakage of GQD as a two-step process, where the GQD first enter the vesicle bilayer and then either diffuse back inside or outside the vesicle. If $I(t)$ is proportional to the GQD concentration inside the vesicle and the bilayer, this model predicts a decrease in intensity-dependent on GQD concentration in the membrane $[\text{GQD}]_M$:

$$\frac{dI}{dt} \propto -k_x[\text{GQD}]_M \tag{2.5}$$

where k_x is the kinetic rate describing the GQD leaving the bilayer. Based on the values of the partition function as well as the difference in timescale between the leakage process and the entry process (seconds or minutes *vs* nanoseconds), I assume that a steady state condition is rapidly reached. Therefore, by comparing Eq. 2.5 with Eq. 2.4, I find that

$$P \propto rk_x/3 = c/t_{entry} \tag{2.6}$$

where c is a constant that depends on the membrane thickness, the partition coefficient and the fraction of particles that go outside the membrane when leaving the membrane and t_{entry} is calculated from our model as reported in Table 2.2. As it is shown in panel c of Figure 2.12, there is a very close match between the permeability obtained with our model and the values computed by fitting the experimental data (dash line in Figure 2.12), further validating the quality of our approach.

CHAPTER 3

Expanding LDA model to Various Conditions

In Chapter 2, the model was introduced and tested with relatively simple lipid profile in membranes (a mixture of POPC and cholesterol) being homogeneously distributed among leaflets at the physiological concentration of ions in water ($0.15\,\mathrm{M}$ NaCl). The NPs that were tested for the model were also rigid in their geometrical shapes.

In this chapter, I extend the model to include various membranes compositions and different ionic strengths. For the nanoparticles, I study the effect of flexible shape. These expansions will add generality to the model so that it can be readily adapted to conditions beyond the cases studied in this thesis. An example for each type of adaptation is presented in the following sections.

3.1 Application to flexible particles

Two parameters in this model were related by the particle, including the P_{LDA} of the probability of finding a comparable LDA which depends on the particle's size, and the P_T of the probability of entry upon meeting the water/lipid interface which depends on the particle's partition coefficient.

For rigid NP in the previous tests, their sizes were represented as the cross-sectional areas of the six faces oriented from the three principal axes of inertia. This size features were then combined with the LDA distribution to calculate the parameter of P_{LDA}, the probability for finding the LDA that matches the areas of the NP.

To define the cross-sectional areas and principal axes for a flexible molecule, a simple approach is to use the potential-energy minimized geometry of the molecule. However, such approach may
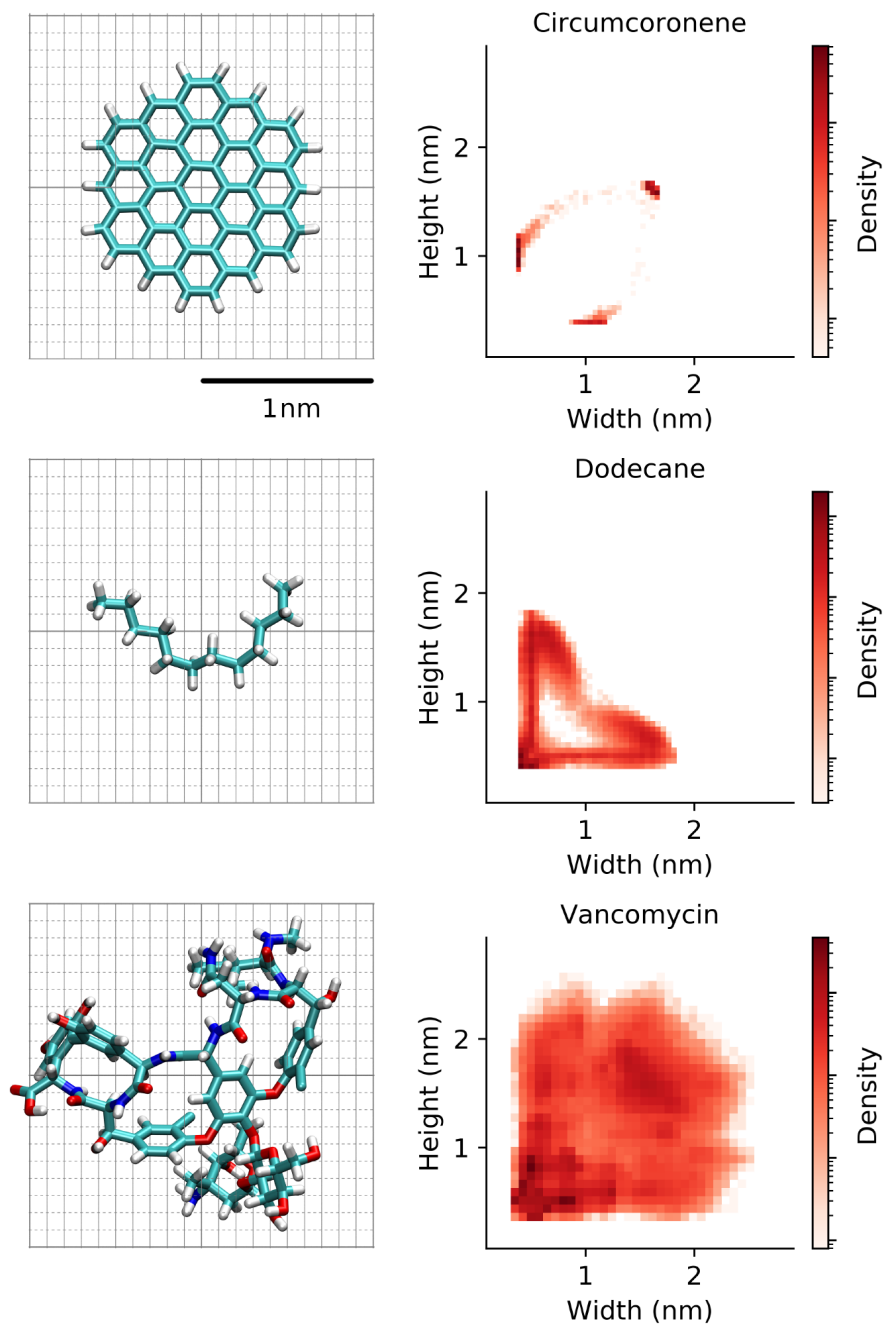
Figure 3.1: Size histograms (left) and cross-sectional areas are measured from the principal axes of inertia (right) of circumcoronene, dodecane, and vancomycin.

result in errors in the size measurement. For example, for a dodecane molecule whose minimized structure is a linear one, this straight geometry has two spiky cross-sectional areas from the two terminals. But at room temperature, dodecane in solvent tend to twist its C-C bonds in favor of in-

creasing entropy of the overall system, resulting in a crunched structure where the spiky terminals are not always accessible for contact. Using the minimized structure would systematically bias for smaller cross-sectional areas and better permeability. Meanwhile, for some other molecules with flexible groups, the extension of these groups as a result of thermal fluctuation creates spikes at the surface of the molecules. These spikes can reach the smaller low-density areas to the hydrophobic region before the rest of the molecular body, which then triggers the process of membrane permeation. Ignoring such effect can result in the underestimation of the permeability of these molecules. In addition to that, for some complicated molecular structures such as RNA and proteins, the 3D structural minimization is a non-trivial problem.

Here rather than to define a static structure with fixed principal axes, I included the flexibility of molecular structure through MD sampling of the dynamic structures of flexible drugs. The cross-sectional areas for each configuration sampled from MD were assembled together to calculate the overall P_{LDA} of the drug for its membrane permeation in this model. Individual P_{LDA}s were calculated for each configuration, from which the average of P_{LDA}s over the whole ensemble was used in the model as the final probability of crossing. By doing so, rare structures that are favored by membrane permeation, once sampled, will be included in probability calculation. In the meantime, this method will require the ergodicity of the MD sampling, which in some cases need to use some specific sampling techniques such as umbrella sampling [90], Monte Carlo sampling [36], Wang-Landau sampling [81], metadynamics [47], and sometimes takes much computational effort.

Below I reported three molecules as examples to illustrate this approach. These molecules included two flexible molecules of dodecane and vancomycin, and a rigid circumcoronene for comparison. The molecular structures for these three molecules are sampled every $10\,\mathrm{ps}$ from a $50\,\mathrm{ns}$ trajectory of unbiased MD simulation in water at $310\,\mathrm{K}$ with $0.15\,\mathrm{M}$ NaCl. The ergodicity was evaluated upon the convergence of the size histogram as shown in Figure 3.1.

As presented in the histograms, the rigid molecules of the circumcoronene had three major peaks in its distribution which corresponded to the cross-sectional areas taken from the three principal axes of inertia. The two flexible molecules had continuous size distributions from nmsq0.25

27

to $1.5\,\mathrm{nm}^2$ for dodecane, and $4\,\mathrm{nm}^2$ for vancomycin.

Table 3.1: Parameters related to the model's prediction for the three flexible particles in the POPC:Cholesterol=90:10 membrane.

Molecule	logP	P_T	P_{LDA}	τ_P	τ_{LDA}	t_{entry}
Circumcoronene	9.09	99%	12%	$1\,\mathrm{ns}$	$1.7\,\mathrm{ns}$	$14\,\mathrm{ns}$
Dodecane	6.1	99%	17%	$1\,\mathrm{ns}$	$1.7\,\mathrm{ns}$	$10\,\mathrm{ns}$
Vancomycin	-3.1	0.08%	14%	$1\,\mathrm{ns}$	$1.7\,\mathrm{ns}$	$17\,\mathrm{\mu s}$

The P_{LDA}s were calculated for these three molecules, each by the average P_{LDA} weighted by the size distribution. Note that the P_{LDA} is a membrane-dependent parameter as well. Here using the profile for the POPC:Cholesterol=90:10 membrane, the P_{LDA}s were 12% for circumcoronene, 17% for dodecane, and 14% for vancomycin, resulting in the predicted time of entry as $14\,\mathrm{ns}$ for circumcoronene, $10\,\mathrm{ns}$ for dodecane, and $17\,\mathrm{\mu s}$ for vancomycin (shown in Table 3.1). The long permeation time for vancomycin was due to its high hydrophilicity.

3.2 Application to different membrane compositions

Lipid composition plays an important role in the physical properties of the membrane, including phase-transition, hydrophobic thickness, surface tension, and permeability [42, 35, 69, 68]. In Chapter 2, I demonstrated the application of the model to POPC:Cholesteorl membranes with different relative ratios of cholesterol. To include membranes of various compositions in this model, here I created a database of 1) homogeneous membranes composed of phospholipid and cholesterol, 2) membranes listed by lipid compositions of organelle membranes of mammalian cells, and 3) membranes of asymmetric leaflets. Results are presented in Figure 3.2 and Figure 3.3.

3.2.1 Membranes as homogeneous mixtures of phospholipids and cholesterols

Figure 3.2 listed 33 membranes of homogeneous mixtures of phospholipid and cholesterol. These membranes differ in the molecular structures of the phospholipids that include the variation in the
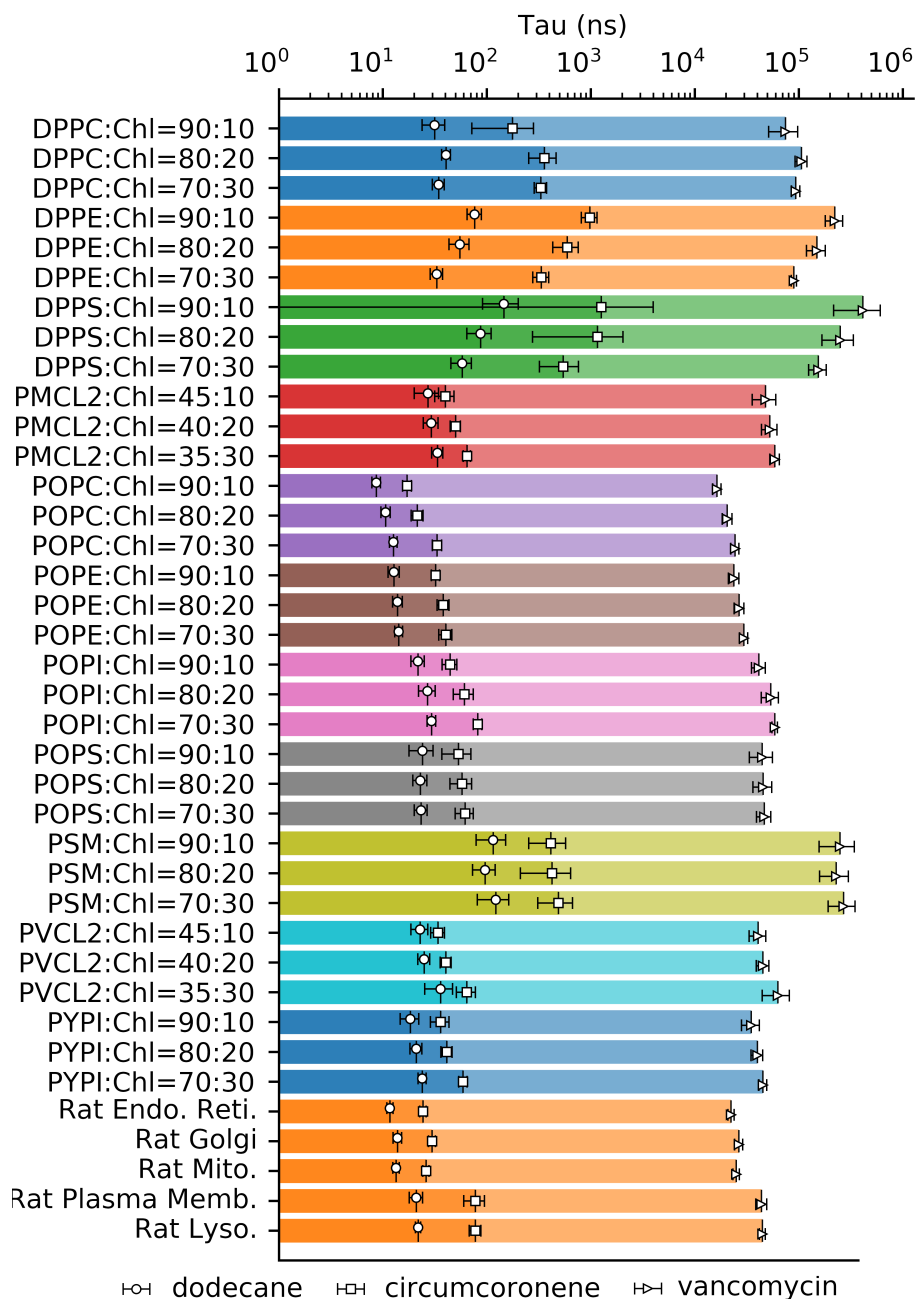
Figure 3.2: Predicted time of entry for multiple membranes and particles. Error bars for 95% confidence interval.

ratio of cholesterol (from 10% to 30%), type of aliphatic chains (DP of 16:0/16:0, PY of 16:0/16:1, and PO of 16:0/18:1), and type of phosphorous groups (PC, PE, PS, PI, SM, CL).

The values reported from Figure 3.2 were the predicted time of entry for the three particles of dodecane, circumcoronene, and vancomycin from Section 3.1. The time of permeation in these

membranes ranges from $10\,\mathrm{ns}$ to $100\,\mathrm{ns}$ for dodecane, and $10\,\mathrm{ns}$ to $1\,\mathrm{\mu s}$ for circumcoronene, and $10\,\mathrm{\mu s}$ to $1\,\mathrm{ms}$ for vancomycin. This result matched the data in Section 3.1 showing dodecane as the most permeable compound among the three structures due to its small size and high hydrophobicity, while vancomycin was the least permeable one due to its hydrophilicity.

A quick comparison among these membranes showed also a good alignment between the current understanding of their physical properties and the predictions of the time of entry. For example, membranes containing shorter and saturated aliphatic chains, such as the 1,2-dipalmitoyl-sn-glycero-3-phosphocholine (DPPC), 1,2-dipalmitoyl-sn-glycero-3-phosphoethanolamine (DPPE) and 1,2-dipalmitoyl-sn-glycero-3-phosphatidylserine (DPPS) membranes, which were known to stay in liquid-ordered phase at room temperature [69, 68], tends to have orders of magnitude of higher time of entry and lower permeability than those membranes with longer and unsaturated aliphatic chains which stays in liquid-disordered phase, such as the POPC, 1-palmitoyl-2-oleoyl-sn-glycero-3-phosphatidylethanolamine (POPE) and 1-palmitoyl-2-oleoyl-sn-glycero-3-phosphatidylserine (POPS) membranes.

The different ratio of cholesterol also shows an interesting effect on various types of lipids. For membranes in liquid-disordered phases with shorter permeation time, such as the POPC, POPE and POPS membranes, the introduction of cholesterols in the membranes increases their permeation time. This observation implies that the lipid packing in the molecular-scale is promoted by the presence of cholesterol in these membranes, leading to higher rigidity of the membrane. The opposite effect is found in membranes in the liquid-ordered phase with longer permeation time, such as the DPPE and DPPS membranes. This result is due to the fact that these lipids are naturally well-packed by their aliphatic chains of the same length and orientation. The presence of cholesterols, however, modifies the situation by introducing cavities inside the membrane, making them more permeable. This finding agrees with the current literature [25, 21].

3.2.2 Membranes of mammalian cellular organelles

Depending on the location of the drug targets, drug molecules often need to come across several biological barriers in order to reach their targets. These barriers include multiple lipid membranes such as the plasma membrane, nuclei membrane, endoplasmic reticulum membrane, and mitochondrial membrane. These membranes often differ in their lipid compositions, resulting in different physical properties such as rigidity, phase transition, and permeability. To make the drug biologically available to their target, it is essential to have information about their permeability in these different membranes systems.

Table 3.2: Lipid composition of membranes[1].

Membrane	POPC	POPE	POPI	POPS	CL	PSM	Cholesterol
Plasma	25	15	5	6	1	11	38
Lysosome	25	9	3	2	1	13	48
Golgi	47	19	11	6	1	7	9
Mitochondrial	43	33	5	1	14	1	4
Endoplasmic Reticulum	56	22	9	2	1	3	7

[1] values represent the number of lipid on each leaflet.

In this chapter, I analyze 5 membranes systems of rat organelles including the plasma membrane, lysosome, mitochondrial membrane, Golgi apparatus, and endoplasmic reticulum membrane. The lipid profiles were retrieved from the experimental value [39], and the number of lipids for each membrane was presented in the Table 3.2. Membranes were prepared, sampled and properties were post-analyzed using the same protocol as for the homogeneous membranes in the 3.2.1. The results were shown in Figure 3.2. These quantities from the figure showed 3 to 4-fold of difference in the time of entry from the least to the most permeable among the five systems, where the lysosome and the plasma membrane were the least permeable membranes among the five systems, in agreement with the fact that the cellular entry was the most difficult step of permeation. After entering the cell, reaching the mitochondrial or Golgi apparatus takes less time, while the endoplasmic reticulum being the easiest to permeate through.

3.2.3 Membranes of asymmetric leaflets
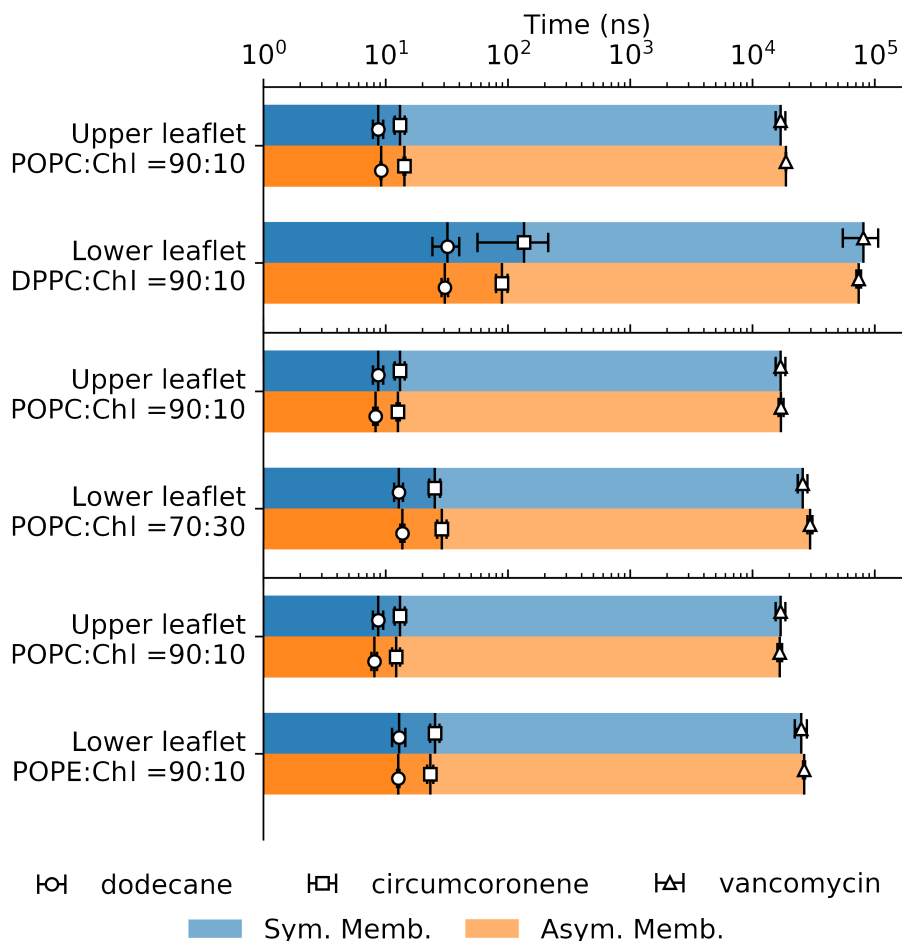
Figure 3.3: Comparison of time of entry for leaflets in asymmetric membranes versus the reference symmetric membranes. Error bars for 95% confidence interval.

Beyond membranes of symmetric leaflets, the model was tested also for membranes of asymmetric leaflets compositions, accounting for variations in the amount of cholesterol (between the POPC membrane with 10% cholesterols and 30%), type of aliphatic chains (between POPC membrane and DPPC membrane), and the head groups (between POPC membrane and POPE membrane). The properties of each leaflet of these asymmetric membranes were then compared to the symmetric ones by the metrics of the LDA statistics and lifetime, represented by the permeation time of model NPs from Section 3.1. The results in Figure 3.3 showed no significant differences between the leaflets in the asymmetric membranes and the symmetric ones, concluding that the

effect of the interleaflet interaction was limited in the lipid packing and the permeability of the leaflet.

An issue about the setup of these asymmetric membranes is the non-equilibrated chemical potential of cholesterols between leaflets, which may lead to diffusion of cholesterols between leaflets [99]. Here the example was meant to sample the dynamics that happened at the nanosecond scale, which was much shorter than the timescale for lipid diffusion.

3.3 Application to various ionic strength in environment

Beyond membranes and particles, the permeation behavior can also influence, and sometimes dominate by some other features of the environmental factors, such as temperature, surface tension, hydration level, and ionic strengths. For example, at environment below the transition temperature, the lipid membrane becomes rigid due to fine lipid packing, resulting in a significant decrease of its permeability [68]. Also, additional surface tension applied to a lipid membrane can increase its packing defect and make the membrane easier to permeate. These conditions are often found from different biological processes, such as different temperatures between body and skin, and the surface tension introduced by the curvature of some cellular organelles. Thus, including the effect of environmental factors in the model is necessary for its applications to these various conditions.

One of the advantages of this general permeation model is its parameters not being built upon any assumption of the environmental conditions. Thus, the model can be easily adapted to various environmental conditions by just estimating the shift of these parameters at any specific condition. Here using an example of environmental ionic strength, I demonstrated the steps of adapting this model to systems at different ion concentrations. The reason for choosing the ionic strength was due to its influence on both the membrane and permeant. While the change of ionic strength of the solution affects the membrane surface dynamics of the low-density areas, it can also change the permeant partition coefficient. For other environmental conditions often only one side could be significantly affected.

3.3.1 Contribution of the NP
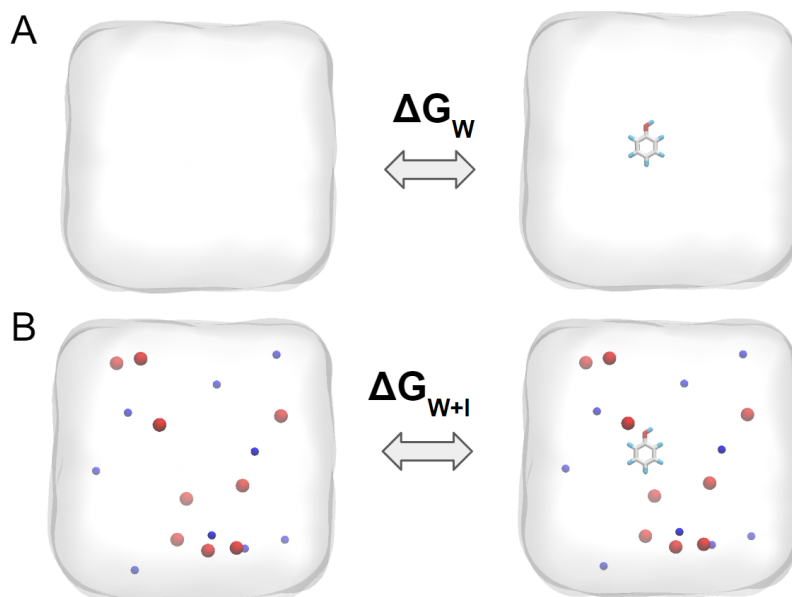
Figure 3.4: Illustration of the alchemical simulations for calculating the change of partition coefficient. A) the change of free energy for introducing the particle to water environment. B) the change of free energy for introducing the particle to environment of water with ion.

In the model, the partition coefficient of the particle is used to calculate the P_T of the chance of entering the lipid side once the particle is placed on the water/lipid interface. Methods for acquiring partition coefficient include both experimental measurement and theoretical calculation from different levels of quantum, classical, coarse-grained, and empirical, in decreasing of difficulty in calculation [16]. Practically for the application purpose, it is often favored to use empirical models for fast estimation. For example, the XLogP [15], ALogP [87], MLogP [67] work with organic compounds and have shown great accuracy in their predictions.

These standard methods for acquiring partition coefficients usually give the values between pure water and octanol. At different ionic strength, the partition coefficient can be affected either through the electrostatic interaction between ions and particle or the protonation of the particle, resulting in the shift of partition coefficient from its standard value in pure water. Given μ_W as the chemical potential of a particle in pure water, and μ_{W+I} as the chemical potential in water with ion, and μ_O as the chemical potential in octanol, the partition coefficient $P_{O/W}$ and $P_{O/(W+I)}$ can

be represented by these quantities as

$$P_{O/W} = exp(-\frac{\mu_O - \mu_W}{k_B T})$$ (3.1)

and

$$P_{O/(W+I)} = exp(-\frac{\mu_O - \mu_{W+I}}{k_B T})$$ (3.2)

Combine Eq. 3.1 and Eq. 3.2, the difference between the two partition coefficients can be written as

$$\Delta logP = log(P_{O/(W+I)}) - log(P_{O/W})$$
$$= log(e)\frac{\mu_{W+I} - \mu_W}{k_B T}$$ (3.3)

And interestingly, this result is independent of the type of second solvent. The difference of chemical potential of $\mu_{W+I} - \mu_W$ can be applied to calculate the partition coefficient shift in any other type of lipid.

To estimate the difference of chemical potential, here I introduced the alchemical method as demonstrated in Figure 3.4. The detailed setup of the two alchemical simulations were introduced in the methodology. In general, here for each particle to be evaluated, two alchemical simulations were performed, one for inserting the particle into a water box, and another for inserting it into an ionized water box. During the process of insertion, change of free energy was probed. The difference between the free energies of $\Delta G_{W+I} - \Delta G_W$ was calculated to present the measurement of the difference of chemical potential, $\mu_{W+I} - \mu_W$.

From another perspective of the ΔGs, the insertion of the particle into each environment includes the cost of free energies from 1) the volume occupation of the particle, 2) the interaction between particles and water, and 3) the interaction between ion and particle. The first two sources

of contributions are shared between the two alchemical simulations, while the third one exists only in the second simulation (Figure 3.4B), which is the change of the chemical potential due to the presence of ion.
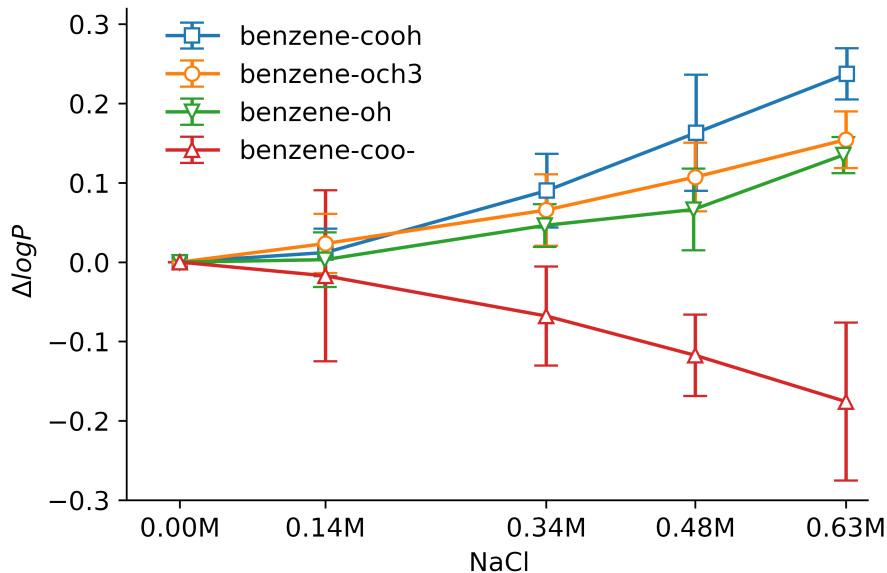
Figure 3.5: Partition coefficient at different ionic strengths for four benzene-derived molecules. Error bar is the difference between the forward and backward FEP calculations.

To demonstrate the alchemical simulations, here I selected four particles of benzene derivatives as examples. The FEP method was used to introduce the particle into water and water+ion systems respectively. Totally five ion concentrations were tested at $0\,\mathrm{M}$, $0.14\,\mathrm{M}$, $0.34\,\mathrm{M}$, $0.48\,\mathrm{M}$ and $0.63\,\mathrm{M}$ of NaCl. The difference of free energy between each non-zero concentration with the pure water was calculated and presented in Figure 3.5, which showed that the change of partition coefficient in different ionic strength was readily captured by this alchemical approach.

The shift of $\Delta logP$ for these particles also showed an interesting trend. The most charged particle was the benzene with carboxyl group which also had the highest change in the partition coefficient, while the less charged ones with hydroxy or methoxy group had relatively less change. In opposite, benzene with protonated carboxyl group showed a negative change, implying its preference for high ionic strength.

3.3.2 Contribution of the lipid membrane
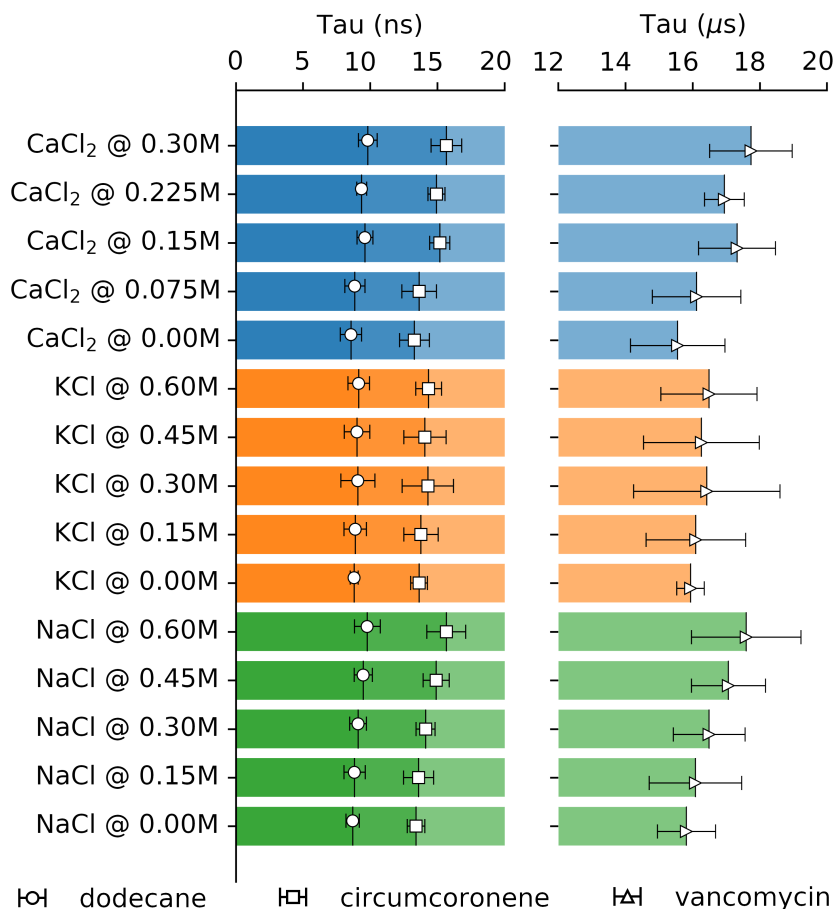
Figure 3.6: Comparison of time of entry in a POPC:Chl=90:10 membrane for different ionic condition. Error bars for 95% confidence interval.

It is well known that ions participate in the lipid membrane packing by the introduction of electrostatic interaction at the hydrophilic region, and sometimes by forming ion bridges between charged groups [18, 101, 8]. These interactions can influence the behavior of the membrane surface dynamics and thus may affect the permeation behavior of the membrane as well.

To estimate such interactions, here I introduce the POPC:cholesterol=90:10 membranes to different ions at different concentrations. For three types of ions of $CaCl_2$, KCl, NaCl, the Cl^- concentrations were sampled evenly at five level between $0\,M$ and $0.6\,M$. Membranes at these different ionic conditions were relaxed and processed using the same protocol as in Chapter 2 and the result was presented in Figure 3.6, using three particles of dodecane, circumcoronene and vancomycin and

model particles. About 20% of increasing permeation time was found for membranes at higher ion concentration, indicating that the presence of ions further facilitated the lipid packing at the hydrophilic region, making the membrane less permeable.
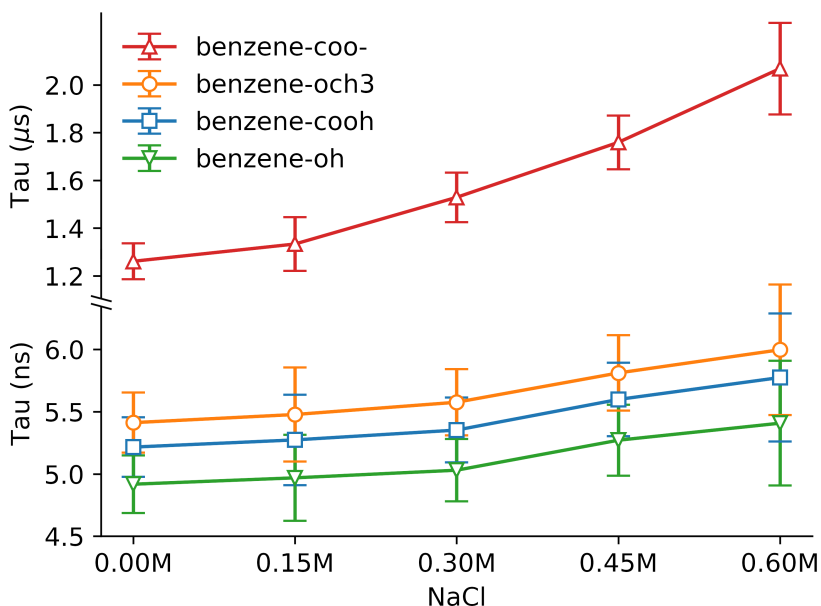
Figure 3.7: Comparison of time of entry in a POPC:Chl=90:10 membrane for benzene derivatives at different ionic condition. Error bars for 95% confidence interval.

Combining both effects on the particle and membrane, Figure 3.7 shows the increase of time of entry with high ionic strength for the three benzene derivatives. Though from Figure 3.5, the increase in *logP* for the three derivatives at high ion concentration favors faster permeation, the increase of the stiffness of the lipid packing dominates the overall permeation behavior, resulting in a reduced rate of the permeation process for all four particles.

CHAPTER 4

Study of COVID-19 Drug Permeability using LDA model

The global health crisis of the COVID-19 epidemic has caused millions of infections and hundreds of thousands of human death. The ongoing study on the drug discovery for treating COVID-19 has derived many drug candidates targeting various viral bait and human processes. These drugs often need to permeate through multiple layers of biological membranes to reach their targets located inside cells, for which an easy and fast model for screening drug permeability and bioavailability is needed for the drug design.

Here using the LDA model introduced in this thesis, I study the permeation of a wide range of molecules in multiple biological membranes including organelle membranes of mammalian cells and the viral membrane of the COVID-19. The time of permeation was estimated for 66 drug candidates for treating COVID-19 based on the list compiled by Gordon *et al.* [30]. Results showed 3 orders of magnitude of difference in permeation time among drug candidates at different membranes, ranging from $10\,\mathrm{ns}$ to $10\,\mathrm{\mu s}$. Further comparison among membranes showed that the time of permeation in COVID-19 viral membrane was generally 50% longer than the endoplasmic reticulum (ER), though the viral lipids were originated from the ER membrane of the host cell. The increase of stiffness of the viral membrane is likely due to the presence of highly-dense transmembrane proteins on the viral membrane, since the increase of permeation reduces to 10% as compared to the ER membrane when the viral membrane is simulated without the protein. The comparison among membranes also shows the time of permeation in the plasma and lysosome

membrane being 3 to 4-fold longer than the viral membrane, implying that drugs permeate faster to virion envelopes than the mammalian cells.

4.1 Building the molecular structure of COVID-19 viral membrane

Transmembrane Protein

COVID-19 spike protein is a type I transmembrane protein.

Cryo-EM structure from Wrapp *et al* [97].

Coronaviral membrane with/without spike protein.

Mammalian membranes of multiple organelles.

Membrane

Drugs

List of **79 drugs candidates** compiled by Gordon *et al* [29].

Structures and properties based on data available at PubChem.

Permeation

Time of permeation of drugs at different membranes were estimated by **LDA model** [1],

Figure 4.1: Flow and data source used in this work of COVID-19 drug database.

Based on the current understanding of the COVID-19 from morphological and biochemical observations, the structure of the COVID-19 virus has a pleiomorphic appearance with an envelope of lipid membrane of $80\,\mathrm{nm}$ to $120\,\mathrm{nm}$ in diameter forms its outer shell [34]. The lipid shell has a rough surface containing highly-dense membrane proteins about $100\,\mathrm{nm}^2$ to $200\,\mathrm{nm}^2$ per protein of transmembrane proteins (estimated from a viral envelope diameter of $80\,\mathrm{nm}$ to $120\,\mathrm{nm}$ [34] and an approximate number of 800 transmembrane proteins per virion [38]). Inside the shell is the nucleocapsid phosphoproteins bonded to its RNA genome.

Here I introduced the viral membrane in the LDA model by studying the dynamics of the viral membrane with transmembrane protein using MD simulations. The viral membrane composition is derived from the ER membrane of the host cell, while higher ratio of PI/PS was detected by

van Genderen *et al.* [95] with statistical significance. Table B.1 showed the number of lipids for the viral membrane.
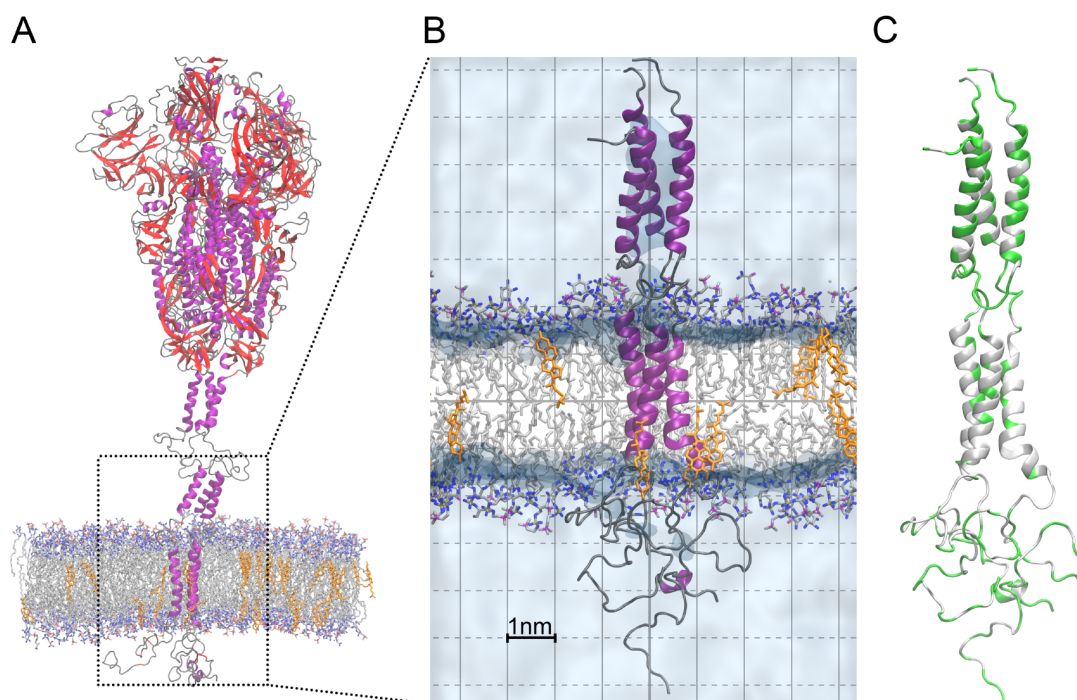
Figure 4.2: Structural diagram of the coronaviral membrane bonded with the COVID-19 spike protein. A) The full-sized spike protein in the coronaviral membrane. Protein colored according to secondary structure (purple for alpha helix, red for beta-sheet, and gray for random coils). On phospholipids, carbon are shown in gray, nitrogen in red, oxygen in blue, and phosphate in tan; cholesterol is shown uniformly in orange. Hydrogen atoms were omitted for clarity. B) The transmembrane region of the spike protein in the coronaviral membrane. C) The transmembrane region of the spike protein colored by the residue type. Non-polar residues are colored in white, while polar residues are in green.

Inside the membrane, I inserted the spike protein of the COVID-19. The spike protein is a type-I transmembrane protein formed by three identical chains, which for coronavirus is responsible for the fusion of viral membrane to the host cell plasma membrane, which is the essential step for the viral infection [6]. It is also the most abundant and noticeable membrane protein on the viral membrane. The typical appearance of the coronaviruses is found from the $20\,\text{nm}$-long spikes emanated from the viral envelope which are directly visible from viral EM images [34]. While the cryo-EM structure of the spike protein of COVID-19 was found by Wrapp *et al.* [105] and available from the Research Collaboratory for Structural Bioinformatics (RCSB) Protein Databank (PDB id

"6vsb"), the transmembrane region of the spike protein was not included in this cryo-EM structure due to the experimental limitation. To complete the transmembrane region of the spike protein, I took also the predicted structure of the spike protein from C-I-TASSER model [40], and appended the transmembrane region to the cryo-EM structure. The steps for merging the two structures were detailed in the methodology.

The structure of the spike protein bonded with the viral membrane was presented in Figure 4.2A. The main spike of the upper part from Figure 4.2A was link to the transmembrane region through the heptad-repeat regions of alpha-helices in their structure. The heptad-repeated region from residue 1146 to 1209 contained repeated polar/non-polar residues. The intertwining of three chains was held by the hydrophobic contact of the non-polar residues [10].

The transmembrane regions were the residue 1210 to 1235 of each chain. These residues were all non-polar except the 1215:TYR, 1219:GLY, and 1223:GLY. The transmembrane regions stayed inside the hydrophobic region of the viral membrane through the hydrophobic contact between these non-polar residues and the aliphatic chains of the lipid. Opposite to the heptad-repeat region, the assemble of the transmembrane regions of the three chains was through the charge-charge interaction among the polar residues.

The C-tails as the lower part under the viral membrane were mostly polar residues and formed random coils. The interaction between these charged residues with the lipid head groups stabilized the end of the transmembrane region of the spike protein.

4.2 Predicting the permeability of COVID-19 drug candidates in lipid membranes

In this section, I introduce the study on the permeability of multiple drug candidates in the viral membrane as developed in Section 4.1 and the mammalian membranes from Section 3.2.2. The viral membranes were prepared in two ways, one with the spike protein and another without, in order to compare the effect of the transmembrane proteins on permeation.
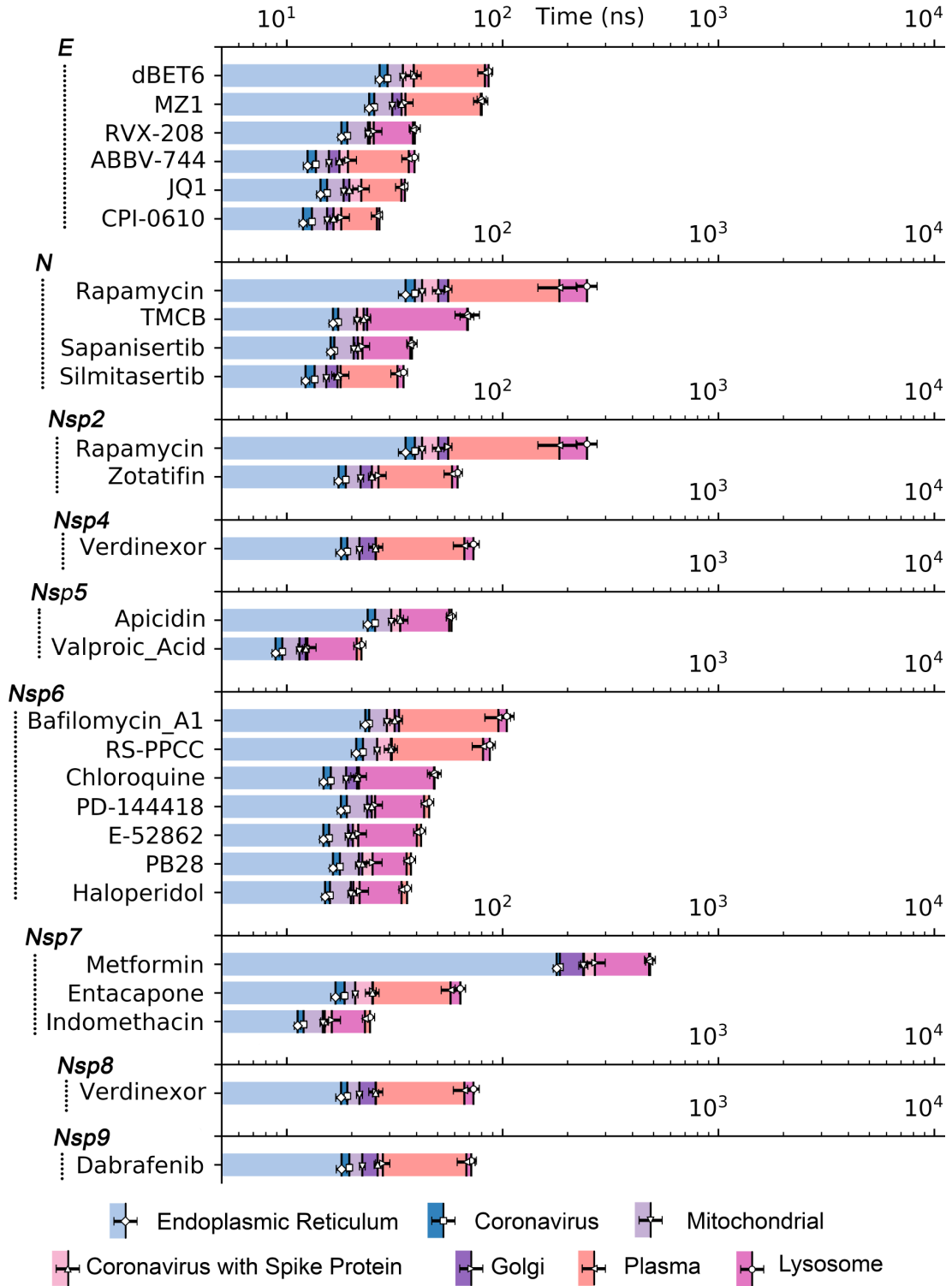
42

Figure 4.3: Time of permeation for drug candidates at different organelle membranes, grouped by viral baits. Error bars present one standard deviation.
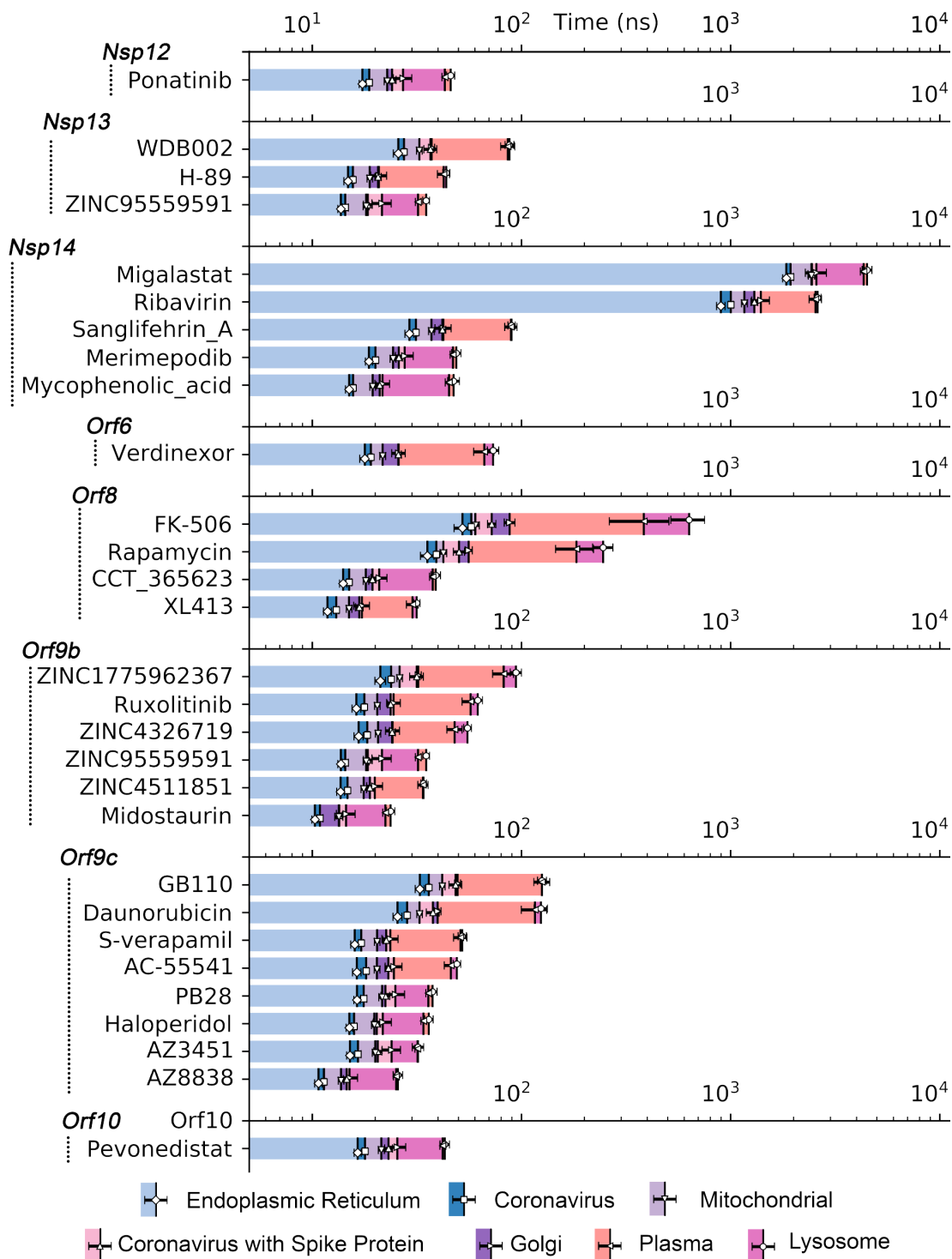
Figure 4.4: (Appended to Figure 4.3) Time of permeation for drug candidates at different organelle membranes, grouped by viral baits. Error bars present one standard deviation.
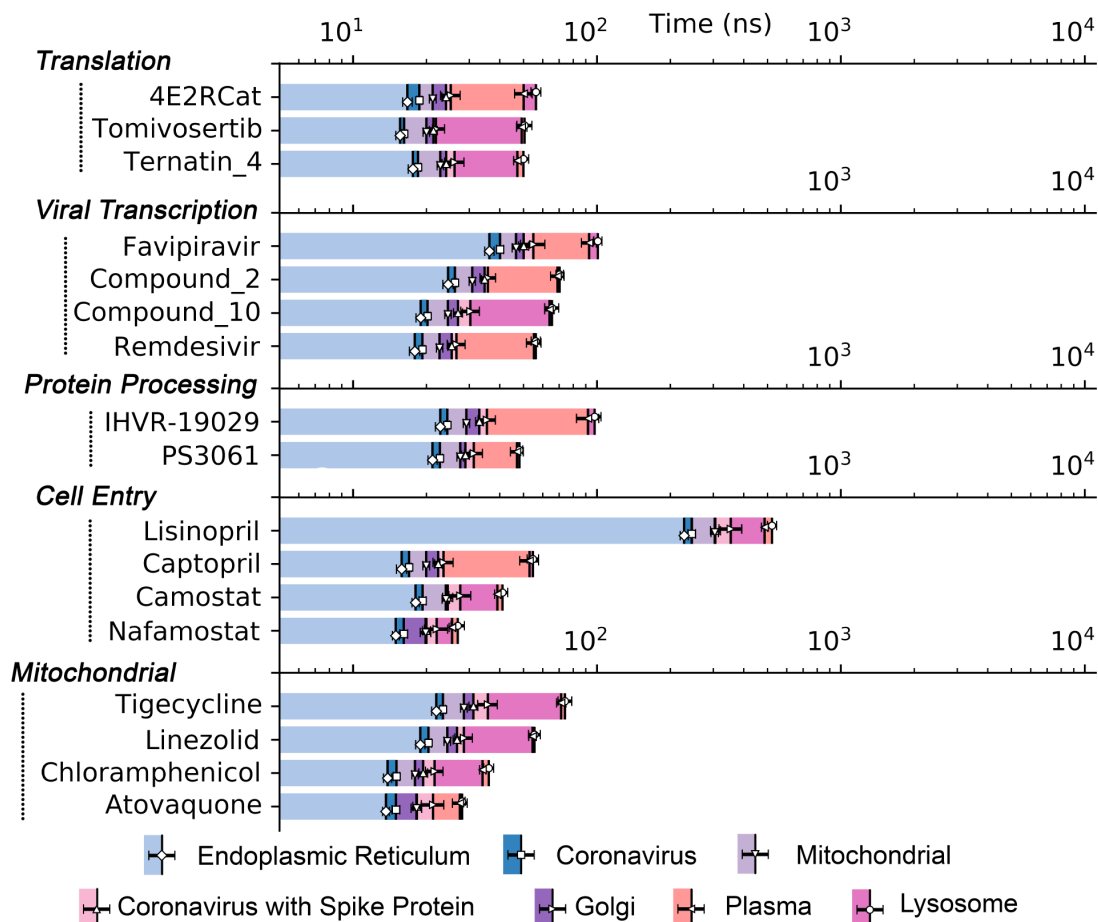
Figure 4.5: Time of permeation for drug candidates at different organelle membranes, grouped by related mammalian processes. Error bars present one standard deviation.

A list of 66 drugs compiled by Gordon *et al.* [30] was introduced to this study. With the known chemical compositions of a drug, the properties of the drug molecule were acquire from multiple sources, as 1) the size feature of the particle was acquired from the protocol introduced from Section 3.1, 2) the experimental partition coefficient was acquired from PubChem, or if not available, from the prediction of XLogP3 model [15].

The permeation model predicted for each pair of a combination of membrane and drug and the predicted time of entry was enlisted in Figure 4.3, Figure 4.4 and Figure 4.5, where the reported the time of entry for 66 drug candidates was grouped by their viral baits, or if viral baits unknown, by their related human processes.

The result showed that both the variation of the lipid composition and the protein profile in-
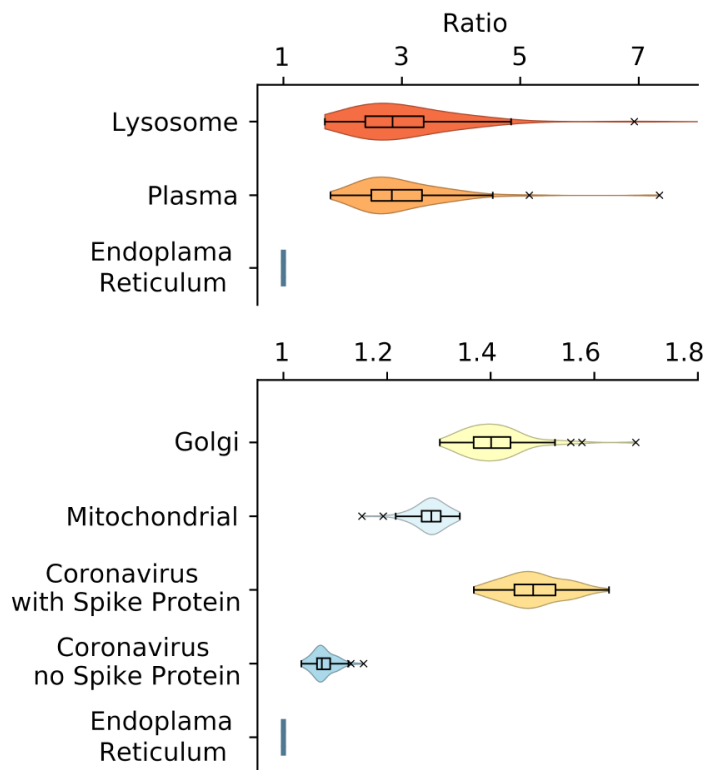
Figure 4.6: Ratios of times of entry for drugs in different membranes. Time of entry in ER membrane was chosen as reference.

creased the stiffness of the COVID-19 viral membrane, compared to the endoplasmic reticulum where the viral membranes are formed. Still, the stiffness of the viral membrane was 3 folds lower than the plasma membrane and lysosomes (see Figure 4.6), which implies the possibility of developing drugs that have virus target (*e.g.*, the nucleocapsid phosphoprotein, the viral RNA genome, and the viral membrane itself) with low permeability into mammalian cells.

While the target of this work was not to make strong suggestions about the candidates for the cure of COVID-19, here this work not only provided insight on the ability of several candidates to reach their target membranes, but also offered a simple way for researchers to estimate the membrane permeability of new candidates (all data required for the model are available in the Appendix B).

CHAPTER 5

Methodology

5.1   MD simulations

I used NAMD [76] version 2.13 with CHARMM Force Field [46] version 36 for lipids, CHARMM General Force Field [97] for simulating the NPs and TIP3P [57] for water molecules. CGenFF [98] software was used to assist in the production of the needed topology files. The initial placement of the membrane's 120 POPC and 12 cholesterol molecules (60 and 6 on each leaflet, respectively) and 8280 water molecules was performed with the CHARMM-GUI membrane builder [45].

All MD simulations were performed with a timestep of $2\,\mathrm{fs}$ while keeping all the C-H and O-H bonds rigid *via* the SHAKE algorithm [80]. Long range electrostatic interactions were modeled with the particle mesh Ewald method [20] using a $0.1\,\mathrm{nm}$ grid spacing, a tolerance of 1E-6 and cubic interpolation, and cubic periodic boundary conditions were applied. Temperature was kept constant at $310\,\mathrm{K}$ using a Langevin thermostat [55] with a time constant of $1\,\mathrm{ps}$, while pressure was kept at $101.325\,\mathrm{kPa}$ using Langevin piston method [60, 24] with period of $50\,\mathrm{fs}$ and $25\,\mathrm{fs}$ decay. To account for the intrinsic anisotropy of the system, the production simulations were performed in the NPsT ensemble, where the x and y dimensions of the periodic system (coplanar with the membrane) are allowed to vary independently from the z dimension. Non-bonded short-range interactions where smoothly switched to 0 between 1 and $1.2\,\mathrm{nm}$ with a X-PLOR switch function.

Membranes were equilibrated for a total of $30\,\mathrm{ns}$, following $50\,\mathrm{ns}$ to $200\,\mathrm{ns}$ ns of production run. The membranes were assumed to be at equilibrium once the time average of the area per

lipid in a NPsT simulations was varying less than 10%, as shown in figures from Section A.1. The surface density dynamics for each of these membranes was analyzed on the production simulations.

The permeation dynamics were studied by placing the different molecule (2 nm) away from the membrane's head groups. To stop the molecules from diffusing too far away from the membrane, I imposed a harmonic potential that pushes the particles towards the membrane when its distance from the membrane interface exceeded 2 nm. I ran 16 simulations for the cys-GQD, 12 for curved-GQD, and 12 for C60, in each case for either 40 ns or until the molecule was embedded in the hydrophobic region of the membrane for at least 1 ns.

VMD [41] and MDAnalysis [64, 31] were used for data analyses and visualization.

5.2 Calculating average time of entry

To estimate the average time of entry for each NP, I plotted the evolution of their distance from the membrane center (see Figure A.18, Figure A.19 and Figure A.20) and collected the time of entry. The green (or yellow for non-entry cases) curve tracks the COM of the NP during the simulation, and the black curve is the COM of the lipid head-groups (including the glycerol group and phosphorous group for POPC, and the 3,4,5-carbons and the oxygen for cholesterol). The time of entry is measured as the time passed from the beginning of the simulation to the intersection of two curves.

Following the assumption that the entrance is a random event, I fitted the collected times with an exponential distribution:

$$P(t)dt = \exp(-\frac{t}{\tau}) \frac{dt}{\tau} \tag{5.1}$$

where τ denote the exponential parameter that has the same unit as t.

In each one of the N independent simulations, the NP can either enter the lipid tails region during the simulation ($t_{sim} = 40$ ns) or not. The likelihood L for n simulations to satisfy $t_i < 40$ ns is given by:

$$L = [\Pi_{i=1}^{n} P(t_i)][P(t_i \geq t_{sim})]^{N-n} \tag{5.2}$$

From Eq. 5.1 and 5.2, I can find the τ that maximize the likelihood:

$$\tau = \frac{t_{sim} \cdot (N - n) + \sum_{i=1}^{n} t_i}{n} \tag{5.3}$$

and the expectation and standard error (from Fisher information) of the time are τ and $\tau/\sqrt{nN}$, respectively.

5.3 Calculating low-density areas

The steps used to define the LDAs and measure their size/shape are presented in the text, but minor additional details are described below.

1. The center for each lipid (Figure 2.7A) is calculated using the center of masses of the heavy atoms near the water/lipid interface (glycerol group for POPC, and top 4 heavy atoms for cholesterol).

2. Based on the center of each lipid, the Voronoi map (Figure 2.7B) is created to calculate the average area for each type of lipid (POPC: $0.603 \, \text{nm}^2$, cholesterol: $0.452 \, \text{nm}^2$).

3. The continuous density map (Figure 2.7C) is created by applying a Gaussian kernel centered on each lipid COM. The height of each kernel is equal to the number of heavy atoms selected for the mapping, while the standard deviation of each kernel depends on the lipid type and is related to its average area by

$$\pi(1.5\sigma)^2 = average\ area \tag{5.4}$$

Final density of atoms per area is compared with the density of water of atoms per volume, using the thickness of one water layer of $0.28 \, \text{nm}$.

4. The local minima on the continuous density map define the centers of each LDA. A threshold of $33 \, \text{nm}^3$ (average water density, considering only the heavy atoms) was used to defines the

border of the LDAs (Figure 2.7D).

5. When neighboring LDAs were connected, I used a watershed algorithm to split them (Figure 2.7E).

6. To sample the size, I started from the LDA's center and for each sampled direction symmetrically extended outwards until one of the two ends intersected the LDA's border, and used that as the maximum length in that direction. For each LDA, I sampled the lengths at 18 unique angles (equally spaced over $180°$ (Figure 2.7F). All the pairs formed by perpendicular directions were considered as a width-and-height pair, and were used to build the final width-height distribution of LDAs (Figure 2.8).

5.4   Experimental setup of GQD leaking in lipid vesicle

GQD encapsulation   GQDs ($2\,nm$ to $8\,nm$ in diameter) were encapsulated in lipid bilayer vesicles using a double emulsion generating microfluidic device as demonstrated previously [58]. Briefly, the water/oil/water double emulsions were made by flow focusing with the inner solution containing the GQDs. The outer solution consisted of $20\,mM$ K-HEPES (pH 7.4), $80\,mM$ KCl, $10\,mM$ MgCl$_2$, 10% PVA (M.W. – 13000 : 23000), 2% glycerol, 1% Poloxamer-188 and $250\,mM$ glucose. The GQD sample was diluted in a buffer with final concentrations of $20\,mM$ K-HEPES (pH 7.4), $80\,mM$ KCl, $1\,mM$ MgCl$_2$, 2% PVA, 2% glycerol, 1% Poloxamer-188 and $180\,mM$ sucrose to match the osmolarities of the solutions on both sides of the vesicle membrane. No significant difference in fluorescence intensity was observed for GQD samples diluted in water when compared to those diluted in the above-mentioned buffer. Lipids (POPC and 18:1 Liss Rhod PE) and cholesterol were purchased from Avanti Polar Lipids Inc. (Alabaster, AL). Liss Rhod PE was added at 0.01% by moles to impart fluorescence to the vesicle membrane for visualization. The formed double emulsion templated vesicles were collected in an imaging chamber made from sticking a glass coverslip on two double-sided tapes fixed onto a glass slide at a certain spacing. The demixing of middle organic phase took place within few minutes of their formation. A 64:36

percentage solution by volume of hexane and chloroform was used for dissolving the lipids as the middle phase.

Imaging An Olympus IX-81 spinning disk confocal microscope was used to image the vesicles encapsulated with GQD samples. Fluorescence images using a GFP filter (ex-486 nm/em-515 nm) were captured at 500 ms exposure with a 60X oil objective (PlanApo, NA:1.42) at time interval of five minutes for 2 h. For vesicle visualization, a TRITC filter (ex-561 nm/em-610 nm) was used at an exposure of 100 ms.

Image analysis All image analysis was carried out using ImageJ. Average fluorescence intensities were measured by drawing rectangular boxes within the interior of the vesicles at different places and taking their mean. Background intensity was calculated using the same approach but with the boxes drawn outside the vesicles in their immediate surroundings. Background subtracted intensities were then normalized with respect to the maximum intensity at time 0. A two-tailed student t-test was carried out with a significance level of 0.05 to compare the background subtracted intensities for the different lipid compositions between $t = 0$ and $t = 1$ h.

5.5 Calculating free-energy pertubation (FEP)

The FEP simulations were carried out using NAMD [76] version 2.13 with CHARMM General Force Field [97] for simulating the benzene derivatives and TIP3P [57] for water molecules. CGenFF [98] software was used to assist in the production of the needed topology files.

Benzene derivatives were initially put at the center of the simulation box and explicit water molecules were then added to the simulation box to keep at least 4 nm margin between benzene molecules and its images from the periodic boundary condition. Ions were inserted randomly to the system with a minimal distances of 0.5 nm between ions. Water molecules within 0.5 nm radius of each ion are removed to avoid collapse. The dual topology was prepared with the initial state ($\lambda = 0$) of pure solvent and the final state ($\lambda = 1$) of solvent with particle.

Simulations were performed with a timestep of $2\,fs$ while keeping all the C-H and O-H bonds rigid *via* the SHAKE algorithm [80]. Long range electrostatic interactions were modeled with the particle mesh Ewald method [20] using a $0.1\,nm$ grid spacing, a tolerance of 1E-6 and cubic interpolation, and cubic periodic boundary conditions were applied. Temperature was kept constant at $300\,K$ using a Langevin thermostat [55] with a time constant of $1\,ps$, while pressure was kept at $101.325\,kPa$ using Langevin piston method [60, 24] with period of $50\,fs$ and $25\,fs$ decay, while ratios between lengths of boxes along the x, y and z dimensions were kept constant. Non-bonded short-range interactions where smoothly switched to 0 between 1 and $1.2\,nm$ with a X-PLOR switch function. The soft-core potential for van der Waals interactions involving vanishing atoms were progressively and linearly decoupled during $\lambda = 0$ and $\lambda = 1$, where the radius shifting coefficient was set to 5. For electrostatic interaction, the decouple started at $\lambda = 0.5$. Trajectory and free energies were recorded each $2\,ps$ during the simulations.

The systems were initially minimized for 1000 steps and then equilibrated at its initial configuration ($\lambda = 0$) for $1\,ns$. The forward transformation introduced 1000 steps between the $\lambda = 0$ and $\lambda = 1$ and for each step, $4\,ps$ of relaxation was performed, following $16\,ps$ of sampling. The backward transformation started immediately after the forward transformation and used the same setup of 1000 steps and each step of $4\,ps$ of relaxation and $16\,ps$ of sampling.

5.6   Properties of drug for COVID-19

CHARMM General Force Field [97] was used for simulating the drugs molecules. CGenFF [98] software was used to assist in the production of the needed topology files. Each drug molecule was presented at the center of an cubic box of $6\,nm$ in each dimension, containing explicit solvent of water and $0.15\,M$ NaCl.

MD setup for drug simulation was the same as the membrane simulations, except the periodic box was isotropic in each dimension. Each system was minimized for 1000 steps, following $0.5\,ns$ of relaxation and $0.5\,ns$ of production. Trajectories were saved each $20\,ps$. For each frame of

the trajectory from production run, sizes of the drug molecule was measured using the protocol provided by the LDA model [51] and used to calculate the P_{LDA} for this conformation. The average P_{LDA} over all the conformation that was sampled from the production run became the final P_{LDA} for the drug molecule.

The partition coefficients of the drugs molecules in octanol and water were taken from Pub-Chem website if experimental values were available, otherwise the prediction of XLogP3 model [15].

5.7 Building the molecular structures of COVID-19 viral membrane

The spike protein structure in MD was developed from the cryo-EM structure [105] where the main part of residue 27 to 1146 for each of the three chains, and the prediction from C-I-TASSER model [40] for the lower chunk of residue 1147 to 1273. The secondary structure of the alpha helices of the lower chunk was kept, while the random coils were twisted to align the alpha helices to vertical orientation. The residue 1210 to 1235 as the transmembrane region were embedded inside the viral membrane.

CHAPTER 6

Conclusion

In this work, I presented a kinetic model for the permeation of NPs in lipid membranes that captures the atomistic details of the process while retaining the simplicity typical of macroscopic models. The model was built on the observation, based on all-atom simulations, that the permeation process is controlled by the formation of LDAs on the membrane surface. The surface dynamics of the membrane is further discussed from an MD perspective, and it was found that the dynamics of these LDAs is generally independent of the presence of NPs. Based on these findings, I factorized the process of permeation into the independent effects of membrane thermal fluctuation and the characteristics of the particles (size, shape, and solubility in the membrane). A combination of these two factors provides a physical model to predict the time elapsed between the NPs in contact with the membrane and the NP fully emerged in the lipid tails. Under the assumption of local equilibrium, this time also serves as the time constant for the model of permeation with barrier using the first-order dynamic.

The model was tested on carbon nanoparticles of different structures and for the same nanoparticle on different lipid vesicles. Predictions from the model matched quantitatively experimental results and simulations, indicating the success of the underlying physical model.

6.1 Impact

The LDA model provides a new perspective into the kinetics of the membrane permeation process from the surface dynamics fluctuation forming low-density areas. Compared with previous phys-

ical models based on the solubility-diffusivity analysis and Fick's first law of diffusion, the LDA model provides insight on the mechanisms of the barrier effect of the membrane surface due to the presence of dense region of lipid head groups, and for the first time quantitatively estimates the time of permeation of particles through this region. The time of permeation estimated from the model was also compared with experimental result for GQD nanoparticles in various membranes of POPC and cholesterol of different ratio, and showed great agreement within the standard deviation, indicating the success of the LDA model in capturing the physics behind the membrane permeation process. The physics provide by the LDA model helps the knowledge gap between the current diffusion models and the biomembrane permeation process.

One of the advantages of the LDA model is its efficiency. Indeed, the LDA model factorizes the crossing effects of particle and membrane so that the properties of particles and membranes can be estimated independently. The four parameters also allow for the inclusion of data from multiple sources, such as the experimental source of partition coefficients, particle shape measures, and computational sources of the membrane surface dynamics. Once the surface dynamics of a given membrane is collected, the statistics of the membrane low-density areas will be readily applied to each particle using very less computational time, making the model a quick tool for large-scale drug screening at low cost. Although using much less computational time, the predictions from the LDA model are comparable to full-atomistic simulations and agree very well with experiments. These characteristics make the LDA model a significant improvement over the current physical models, such as the solubility-diffusion model about accuracy, and a competitive candidate to the empirical models such as "rule of five", QSAR and QSPR about efficiency.

The predicting capabilities of the LDA model have been applied to various biological membranes. Examples provided in the thesis include different cellular organelles such as plasma membrane, lysosome, mitochondrial, Golgi apparatus, and endoplasmic reticulum, as well as viral envelopes. These characteristics of the model make it specifically relevant to the process of drug design from the screening of drugs with permeation problem during the early stage of drug discovery, to the design designing NPs to target specific sites, and to the prediction of the accumulation of

the drug candidates in specific organs or intracellular compartments, which may aid the prediction of the side effects.

6.2 Future work

Results of this work also suggest directions for further research in this field. The parameters in the model may be further validated through different experimental and theoretical approaches. For example, a membrane with increased tension can induce more low density areas on the membrane surface and may be used to assess the increase in membrane permeability. Experiments such as fluorescent labeling and NMR can be used to probe the surface atom density distributions and lipid mobility [27] (although current labeling techniques can introduce artifacts) while the theoretical models can be employed to describe the thermodynamics underlying the formation of low density areas [107].

Given the complexity of the process that the model tries to capture, there are few aspects that are left to future improvements. Some are related to the model itself, as our approximation of the particle as a rectangular prism, can be substituted with a more accurate surface integral to better utilize the information provided by the NPs' structures. Furthermore, the model can be improved by refining the interactions between the membrane and NPs as they may influence the orientation of NPs as well as the formation and kinetics of the formation of the LDA.

Other improvements in the application of the model can be made by extending it beyond the single permeation events, to include for example statistical variation of the NPs. A straightforward improvement would be to consider a distribution of sizes for the permeant, for example, due to the formation of clusters and aggregates [49, 79, 23]. The model would not need to be fundamentally changed, as aggregates can be treated as larger NPs, but care should be taken to account for different phenomena, like induced-endocytosis, particle aggregates' fragmentation and long-term changes of the membrane. Of note, long term effects of the permeation on the membrane, for example, a change in the mechanical and kinetic properties as well as the formation of long-living

pores [13] [93] have not been included in this discussion. These effects have the potential to drastically affect the permeation process, but their description is dependent on a much larger number of factors that can be the target of future studies.

APPENDIX A

MD Simulations of Membranes and NPs

A.1   Relaxation of membranes
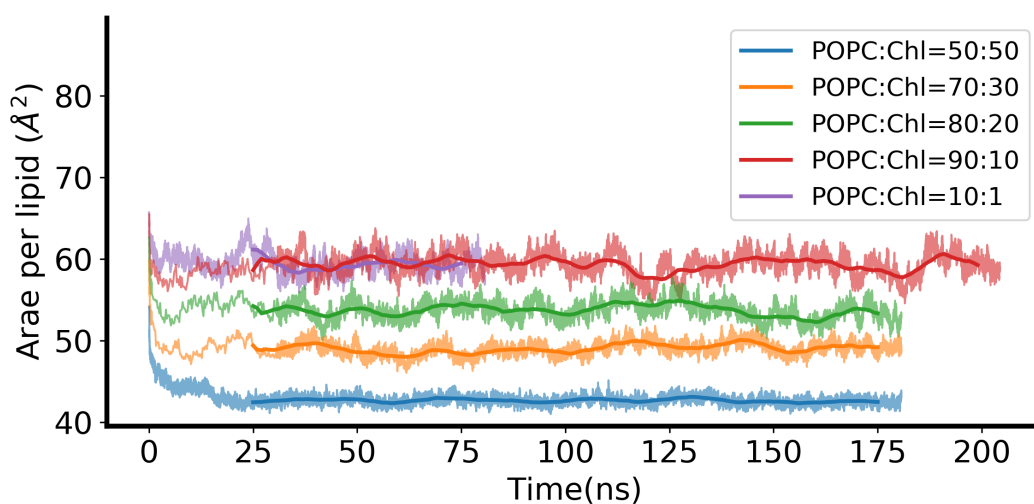
Figure A.1:   The area per lipid over time for the POPC membranes presented in this work. Light lines represent the area per lipids over time for each frame. Dark lines represent the running average of the light line over a 10 ns window.
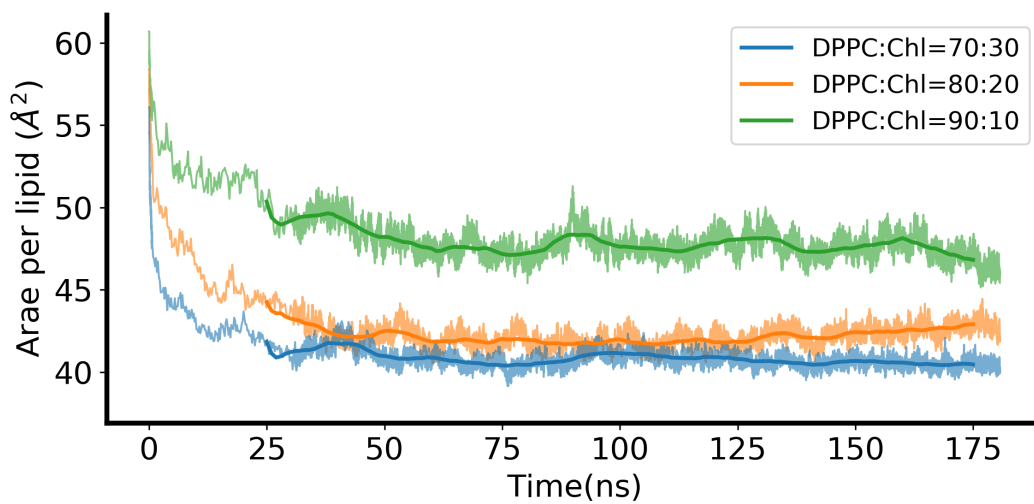
Figure A.2: The area per lipid over time for the DPPC membranes.
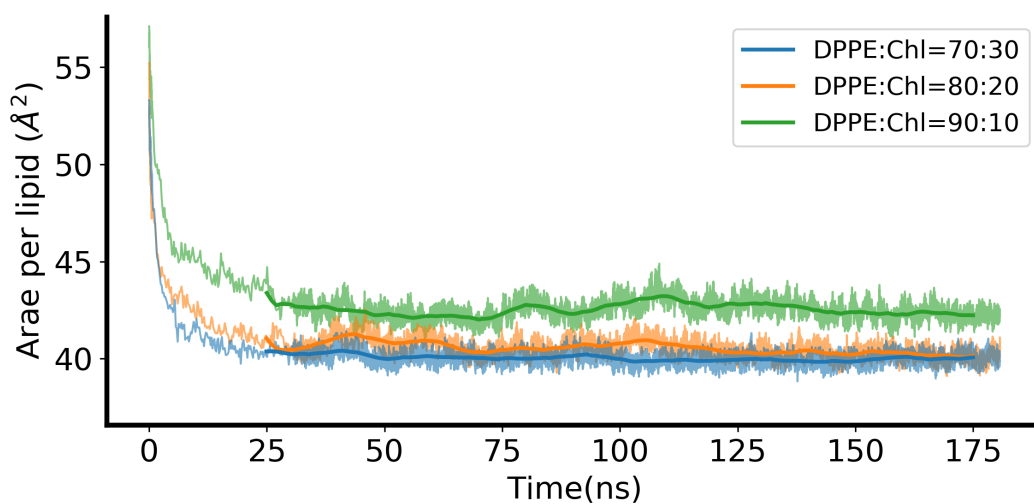
Figure A.3: The area per lipid over time for the DPPE membranes.
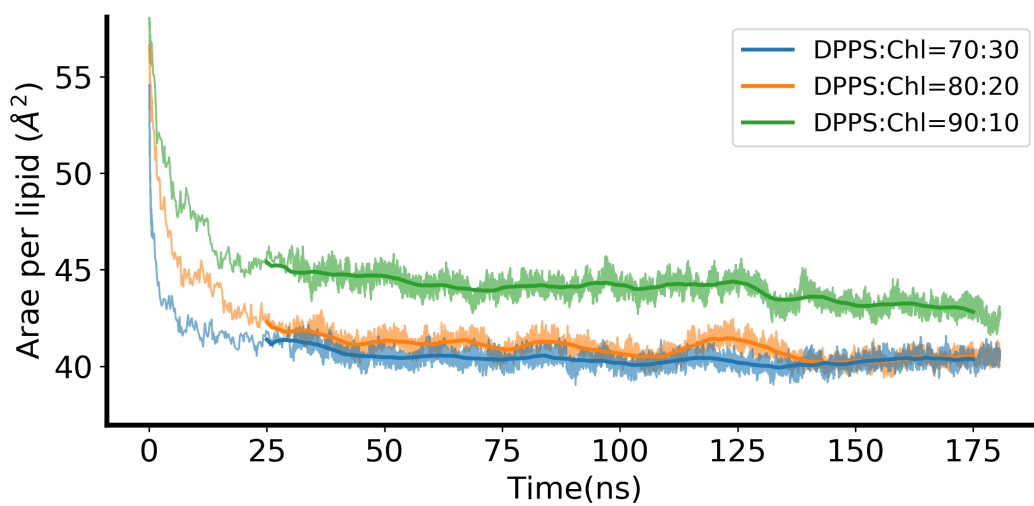
Figure A.4: The area per lipid over time for the DPPS membranes.
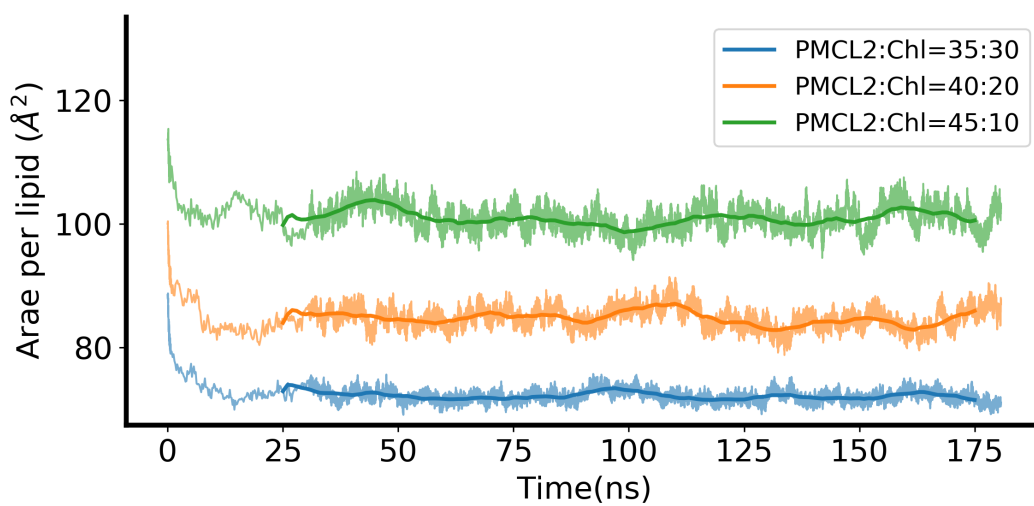
Figure A.5: The area per lipid over time for the PMCL2 membranes.
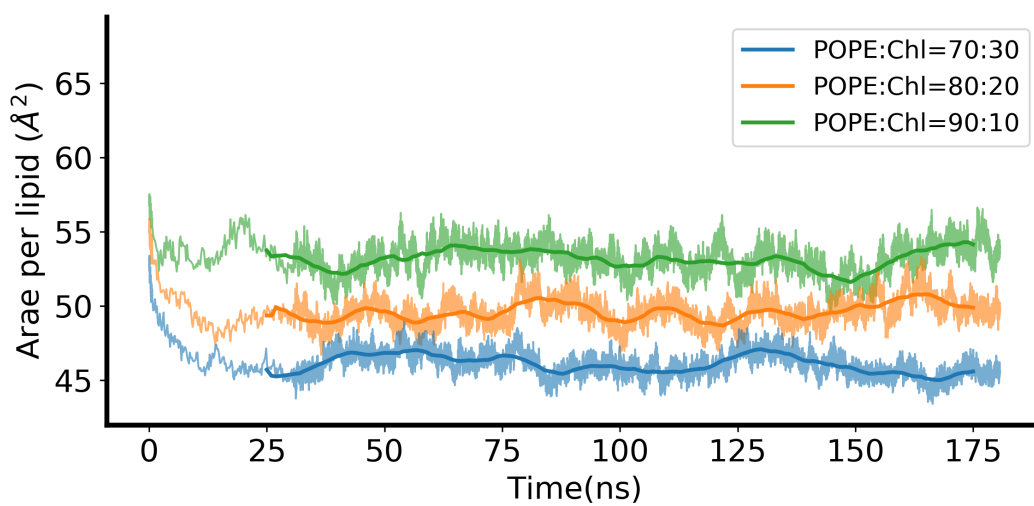
Figure A.6: The area per lipid over time for the POPE membranes.
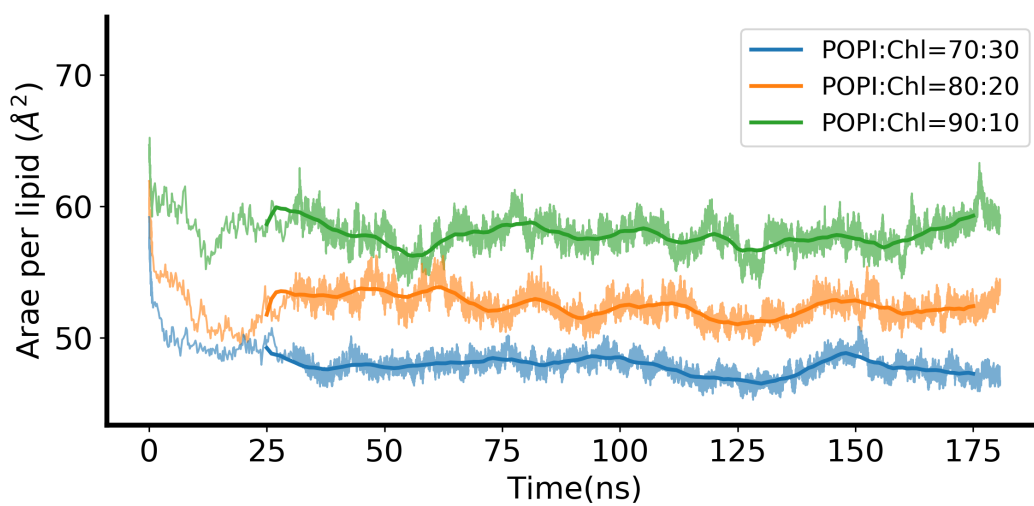
Figure A.7: The area per lipid over time for the POPI membranes.
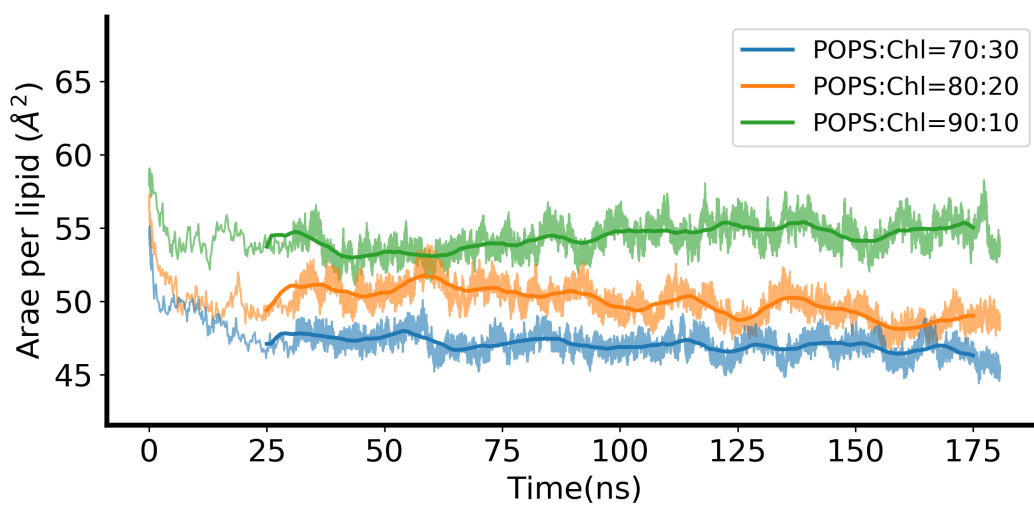
Figure A.8: The area per lipid over time for the POPS membranes.
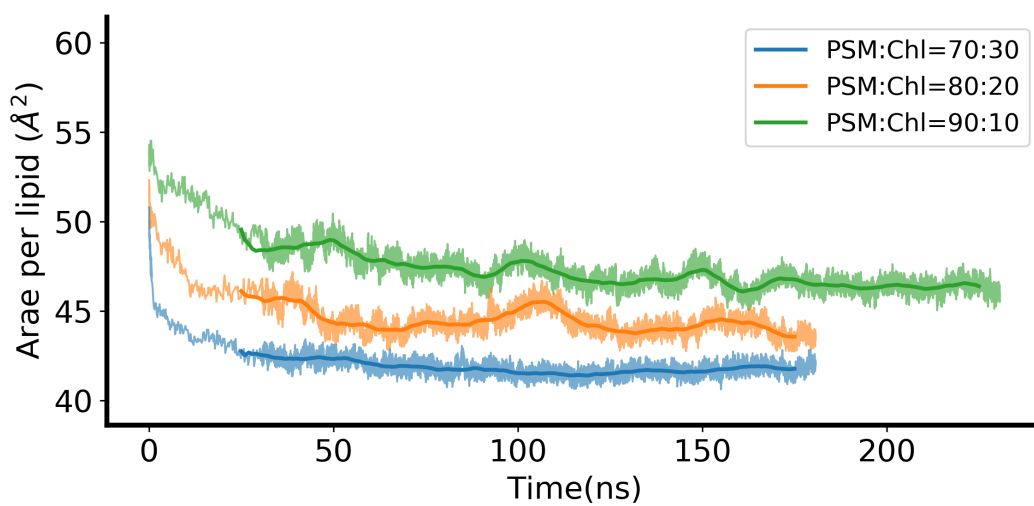
Figure A.9: The area per lipid over time for the palmitoylsphingomyelin (PSM) membranes.
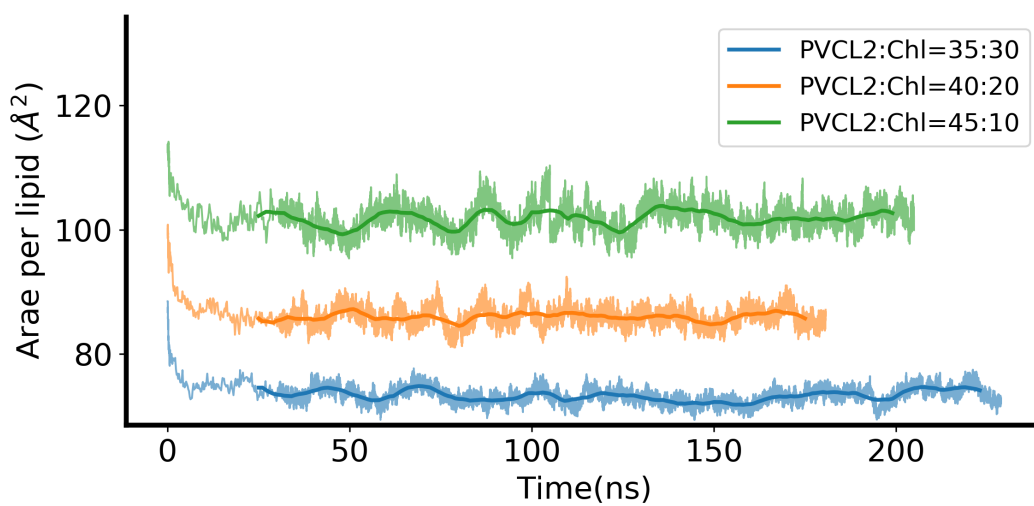
Figure A.10: The area per lipid over time for the PVCL2 membranes.
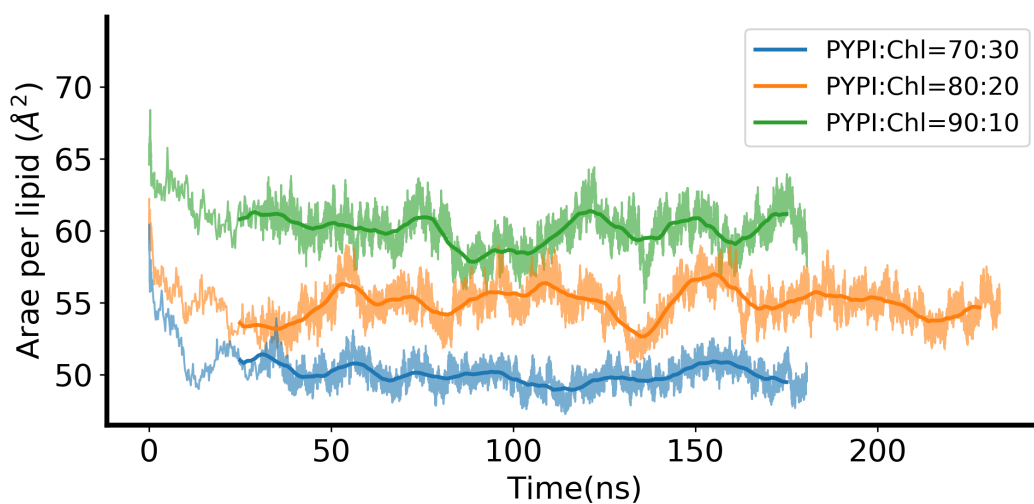
Figure A.11: The area per lipid over time for the PYPI membranes.
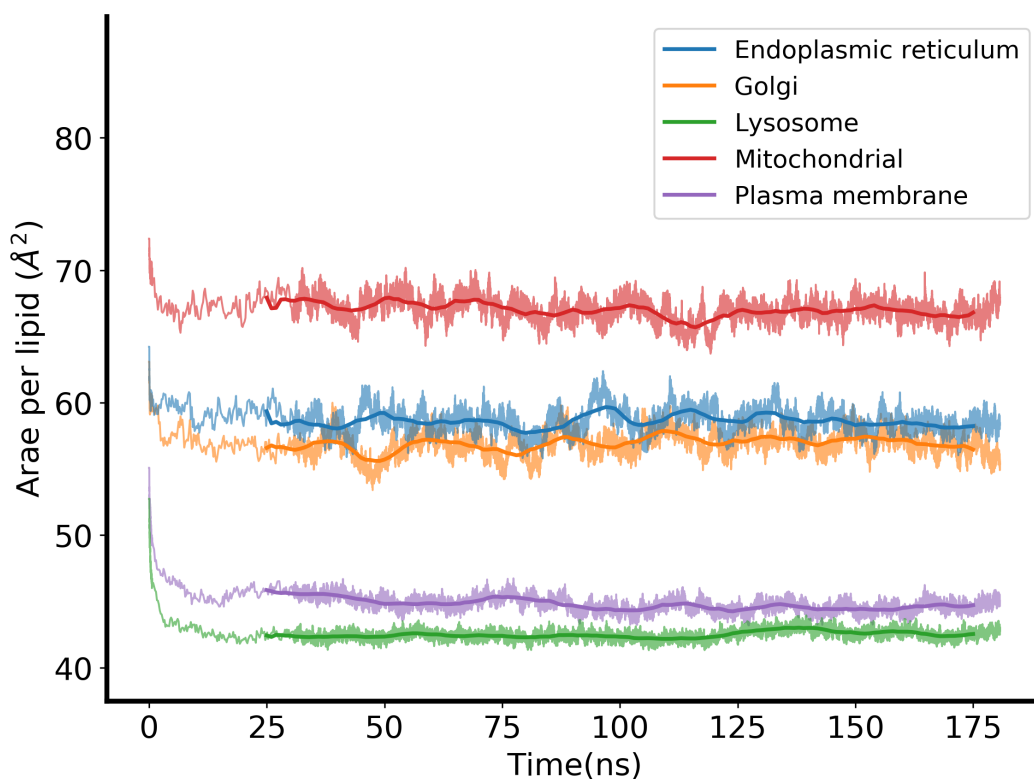
Figure A.12: The area per lipid over time for the mammalian membranes. Membranes were built upon the ratio provided by Horvath *et al.* [39].
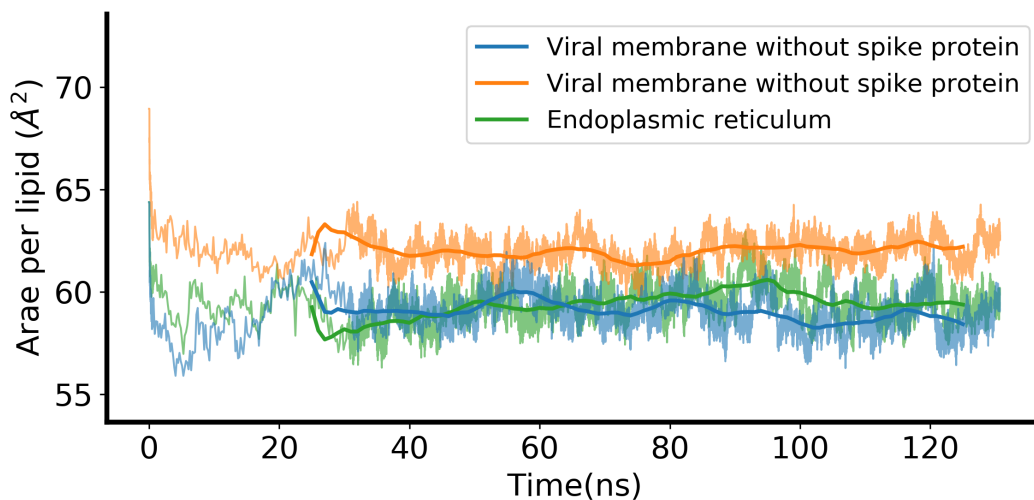
Figure A.13: The area per lipid over time for the coronaviral membranes and endoplasmic reticulum. Membranes were built upon the ratio provided by van Genderen *et al.* [95].
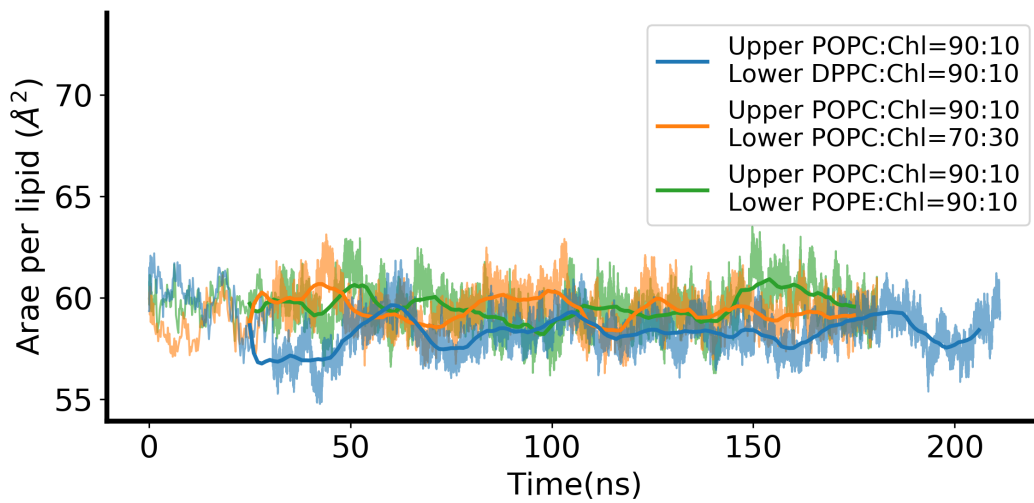
Figure A.14: The area per lipid over time for the asymmetric membranes.
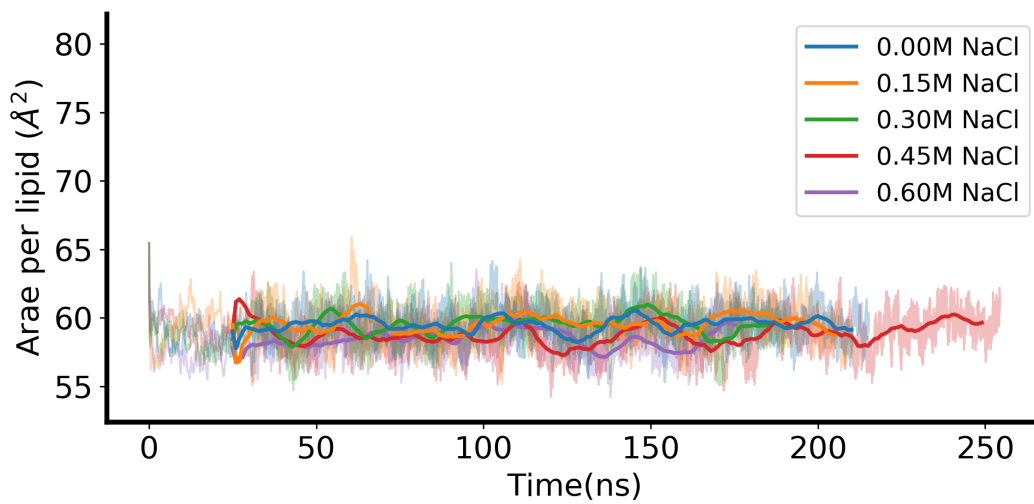
Figure A.15: The area per lipid over time for the POPC:Chl=90:10 membrane at different Na-Clconcentration.
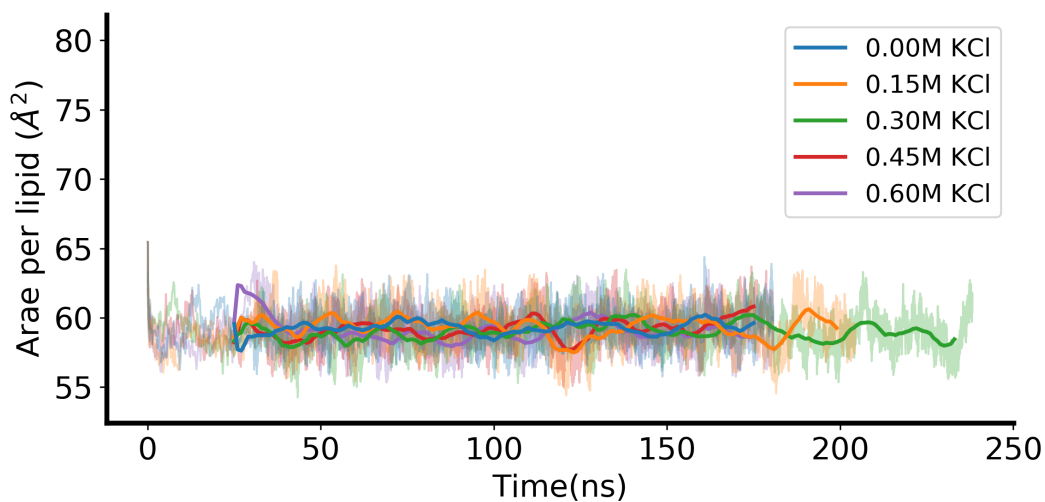
Figure A.16: The area per lipid over time for the POPC:Chl=90:10 membrane at different KClconcentration.
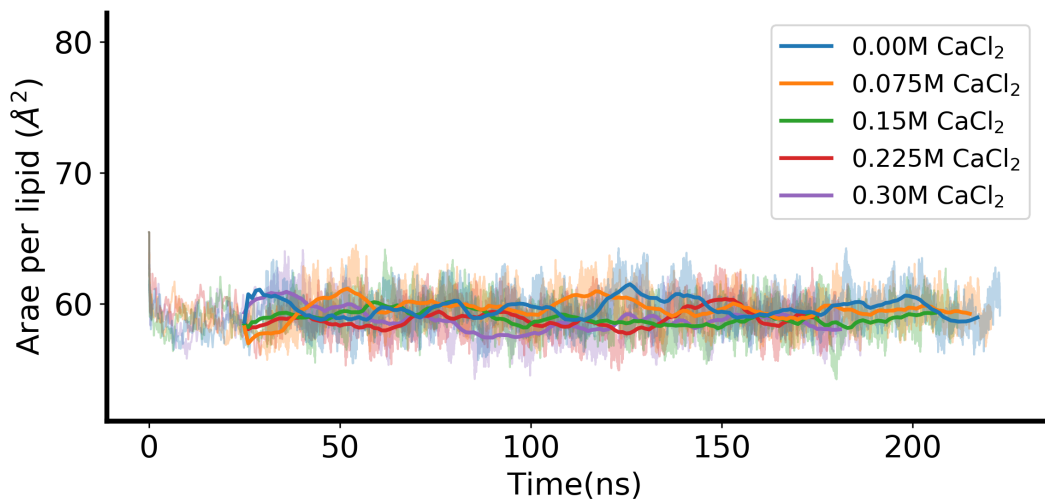
Figure A.17: The area per lipid over time for the POPC:Chl=90:10 membrane at different CaCl$_2$concentration.

A.2   NPs in Membranes
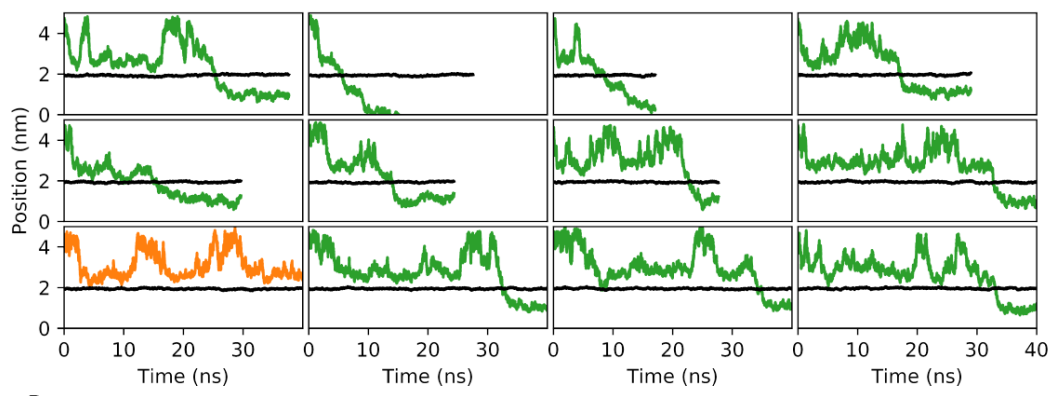
Figure A.18:   12 simulations of C60 with POPC/cholesterol membrane. Green (that entered) and orange (that did not enter) trajectories showed where the C60s were regarding the membrane along the z-axis. The black line showed the surface of the membrane for comparison.
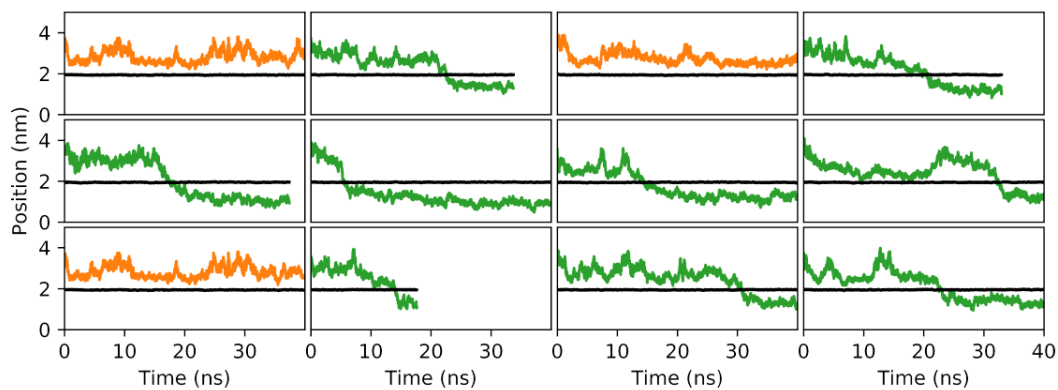
Figure A.19:   12 simulations of curved-GQD with POPC/cholesterol membrane.
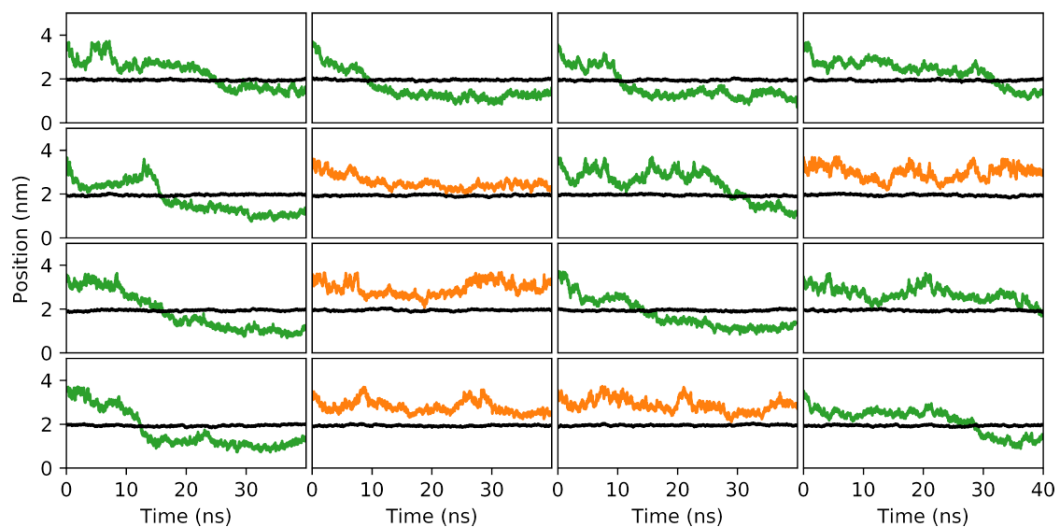
Figure A.20: 16 simulations of cys-GQD with POPC/cholesterol membrane.

APPENDIX B

Permeation Database for COVID-19 Drugs

Table B.1: Lipid composition of membranes[1,2].

Membrane	POPC	POPE	POPI	POPS	PSM	Cholesterol
Endoplasmic Reticulum	72	17	6	4	2	7
Coronavirus wo spike protein	65	10	9	5	4	7
Coronavirus w spike protein	89	13	13	7	5	9

[1] values represent the number of lipid on each leaflet.
[2] based on the ratio provided by van Genderen *et al.* [95].

Table B.2: Parameters of the LDA model for 66 drugs

Drug	logP	P_p^3	P_l^4	P_g^5	P_m^6	P_e^7	P_{cs}^8	P_c^9	τ_p^3	τ_l^4	τ_g^5	τ_m^6	τ_e^7	τ_{cs}^8	τ_c^9
4E2RCat	5.40^2	10.6± 0.3%	10.5± 0.5%	10.7± 0.3%	8.6± 0.3%	2.3± 0.3%	11.2± 0.4%	3.1± 0.5%	18.7± 0.5 ns	25.2± 2.3 ns	16.7± 0.8 ns	24.0± 0.9 ns	56.3± 2.6 ns	21.2± 0.7 ns	50.1± 4.1 ns
ABBV-744	3.90^2	14.2± 0.4%	13.5± 0.5%	14.1± 0.4%	11.6± 0.4%	3.3± 0.4%	14.8± 0.5%	4.3± 0.6%	13.7± 0.3 ns	19.2± 1.8 ns	12.5± 0.6 ns	17.6± 0.7 ns	39.1± 1.7 ns	15.7± 0.5 ns	36.8± 2.6 ns
AC-55541	4.10^2	10.9± 0.3%	10.7± 0.5%	10.9± 0.3%	8.9± 0.3%	2.7± 0.3%	11.6± 0.4%	3.4± 0.5%	18.1± 0.5 ns	24.6± 2.3 ns	16.4± 0.8 ns	23.2± 0.9 ns	49.3± 2.1 ns	20.4± 0.6 ns	46.1± 3.2 ns
AZ3451	6.90^2	11.9± 0.3%	11.0± 0.4%	11.7± 0.2%	10.0± 0.3%	4.1± 0.3%	11.8± 0.3%	4.9± 0.4%	16.6± 0.5 ns	24.0± 2.4 ns	15.2± 0.6 ns	20.6± 0.9 ns	31.9± 1.0 ns	20.0± 0.7 ns	32.1± 2.0 ns
AZ8838	1.80^2	17.1± 0.5%	17.0± 0.7%	16.5± 0.4%	13.9± 0.5%	5.2± 0.5%	16.9± 0.7%	6.1± 0.6%	11.4± 0.3 ns	15.1± 1.4 ns	10.7± 0.4 ns	14.6± 0.5 ns	25.2± 0.8 ns	13.8± 0.4 ns	25.7± 1.3 ns
Apicidin	4.40^2	7.8± 0.3%	8.0± 0.4%	7.7± 0.2%	6.2± 0.2%	2.3± 0.2%	8.0± 0.3%	2.7± 0.3%	25.7± 0.6 ns	33.6± 2.9 ns	23.7± 1.1 ns	33.6± 1.2 ns	56.6± 1.8 ns	30.5± 1.0 ns	58.1± 3.0 ns
Atovaquone	5.80^1	13.0± 0.3%	12.3± 0.4%	13.0± 0.2%	11.2± 0.2%	4.7± 0.3%	12.9± 0.2%	5.7± 0.5%	15.0± 0.6 ns	21.3± 2.2 ns	13.6± 0.5 ns	18.2± 0.9 ns	28.0± 0.8 ns	18.3± 0.7 ns	27.4± 1.9 ns
Bafilomycin A1	6.00^2	8.3± 0.3%	8.5± 0.4%	7.8± 0.3%	6.3± 0.3%	1.3± 0.2%	8.3± 0.4%	1.6± 0.3%	24.1± 0.3 ns	31.7± 2.7 ns	23.1± 1.2 ns	33.2± 1.2 ns	104.6± 8.2 ns	29.1± 1.0 ns	95.8± 13.0 ns
CCT 365623	2.49^2	13.0± 0.4%	12.5± 0.6%	12.7± 0.3%	10.5± 0.3%	3.5± 0.3%	13.0± 0.5%	4.0± 0.5%	15.0± 0.4 ns	20.9± 1.8 ns	14.1± 0.6 ns	19.5± 0.7 ns	37.7± 1.3 ns	18.1± 0.5 ns	39.0± 2.0 ns

Compound															
CPI-0610	3.00[2]	14.8±0.4%	14.4±0.6%	14.8±0.4%	12.3±0.3%	4.8±0.4%	15.1±0.5%	5.9±0.5%	13.1±0.3 ns	17.9±1.6 ns	11.9±0.5 ns	16.5±0.6 ns	26.9±0.8 ns	15.4±0.5 ns	26.2±1.6 ns
Camostat	1.10[2]	11.1±0.3%	10.4±0.4%	10.7±0.2%	9.1±0.3%	3.6±0.3%	10.8±0.3%	4.1±0.4%	19.3±0.6 ns	27.5±2.8 ns	18.1±0.6 ns	24.5±1.2 ns	39.1±1.1 ns	24.0±0.8 ns	41.0±2.1 ns
Captopril	0.34[1]	16.9±0.6%	16.3±0.7%	16.4±0.5%	13.4±0.5%	3.5±0.4%	17.3±0.8%	4.3±0.7%	17.0±0.3 ns	23.5±2.2 ns	15.8±0.8 ns	22.4±0.8 ns	54.7±3.0 ns	20.0±0.6 ns	52.9±4.7 ns
Chloramphenicol	1.14[1]	13.9±0.4%	13.0±0.7%	13.7±0.3%	11.3±0.3%	4.1±0.4%	14.0±0.5%	4.7±0.4%	15.1±0.4 ns	21.6±1.8 ns	13.8±0.5 ns	19.4±0.8 ns	34.0±1.0 ns	18.0±0.5 ns	36.0±1.7 ns
Chloroquine	4.63[1]	12.3±0.4%	12.1±0.6%	12.0±0.4%	9.7±0.4%	2.7±0.3%	12.5±0.6%	3.2±0.5%	16.0±0.3 ns	21.6±1.8 ns	14.8±0.7 ns	21.2±0.7 ns	48.2±2.2 ns	18.8±0.6 ns	48.4±3.6 ns
Compound 10	4.07[2]	9.9±0.4%	8.8±0.4%	9.5±0.3%	7.7±0.3%	2.1±0.2%	9.8±0.4%	2.4±0.3%	20.2±0.5 ns	30.3±2.7 ns	18.9±0.8 ns	26.9±1.1 ns	63.9±2.8 ns	24.5±0.8 ns	65.4±4.3 ns
Compound 2	2.47[2]	7.7±0.3%	7.6±0.5%	7.4±0.2%	6.1±0.3%	1.9±0.2%	7.9±0.4%	2.3±0.3%	26.2±0.5 ns	35.7±2.6 ns	24.5±1.2 ns	34.7±1.1 ns	70.4±2.5 ns	30.8±0.9 ns	68.9±4.4 ns
Dabrafenib	4.80[2]	10.2±0.4%	9.5±0.6%	10.0±0.4%	7.9±0.4%	1.8±0.2%	10.7±0.5%	2.3±0.4%	19.5±0.4 ns	27.9±2.1 ns	18.0±1.0 ns	26.4±1.0 ns	71.7±4.0 ns	22.4±0.7 ns	68.0±6.4 ns
Daunorubicin	1.83[1]	7.2±0.3%	7.3±0.5%	7.2±0.2%	5.4±0.3%	1.1±0.2%	7.6±0.4%	1.4±0.3%	28.5±0.4 ns	37.8±2.7 ns	25.6±1.2 ns	39.8±1.4 ns	124.0±9.2 ns	32.6±1.0 ns	116.1±16.1 ns
E-52862	3.50[2]	12.5±0.4%	12.2±0.5%	12.0±0.3%	10.1±0.3%	3.3±0.3%	12.3±0.4%	4.4±0.4%	15.7±0.4 ns	21.5±1.9 ns	14.8±0.6 ns	20.3±0.8 ns	40.1±1.4 ns	19.3±0.6 ns	41.9±2.1 ns

Entacapone	2.10^2	10.8±0.4%	10.7±0.6%	10.7±0.4%	8.3±0.4%	2.1±0.3%	11.5±0.5%	2.8±0.4%	18.6±0.3 ns	25.0±1.8 ns	16.8±0.9 ns	25.1±0.9 ns	63.8±3.5 ns	20.8±0.6 ns	57.5±5.5 ns
FK-506	3.80^2	3.6±0.3%	3.8±0.5%	3.5±0.3%	2.4±0.2%	0.2±0.1%	4.1±0.3%	0.4±0.1%	57.7±1.7 ns	72.2±3.3 ns	52.3±4.7 ns	88.0±5.2 ns	634.7±116.6 ns	60.3±2.7 ns	384.9±121.9 ns
Favipiravir	-0.60^2	25.4±0.7%	24.9±0.8%	25.3±0.7%	21.1±0.6%	6.5±0.7%	26.4±0.7%	8.5±1.1%	40.1±1.3 ns	54.9±6.3 ns	36.2±1.6 ns	50.1±2.4 ns	100.8±4.0 ns	46.6±1.7 ns	92.8±6.5 ns
GB110	4.30^2	5.6±0.2%	5.6±0.4%	5.6±0.2%	4.3±0.2%	1.0±0.1%	5.9±0.3%	1.3±0.2%	36.1±0.5 ns	48.5±3.4 ns	32.7±1.6 ns	49.6±1.6 ns	125.6±6.2 ns	41.9±1.3 ns	125.5±11.1 ns
H-89	3.50^2	12.5±0.4%	12.5±0.6%	12.0±0.4%	9.9±0.4%	3.0±0.3%	12.5±0.6%	3.7±0.5%	15.7±0.3 ns	20.9±1.8 ns	14.9±0.7 ns	20.7±0.7 ns	43.8±1.7 ns	18.9±0.6 ns	42.5±2.8 ns
Haloperidol	4.30^1	12.4±0.3%	12.0±0.5%	11.8±0.2%	10.1±0.3%	3.8±0.3%	11.9±0.4%	4.3±0.4%	15.9±0.4 ns	21.8±2.1 ns	15.1±0.5 ns	20.4±0.9 ns	34.1±1.0 ns	19.8±0.6 ns	36.2±1.7 ns
IHVR-19029	1.67^1	8.4±0.3%	7.8±0.4%	8.1±0.3%	6.5±0.3%	1.4±0.2%	8.5±0.4%	1.8±0.3%	24.4±0.5 ns	35.4±2.9 ns	22.8±1.0 ns	33.0±1.2 ns	97.8±6.1 ns	29.2±0.9 ns	91.9±9.6 ns
Indomethacin	4.27^1	16.1±0.4%	15.7±0.6%	15.6±0.3%	13.4±0.3%	5.6±0.5%	15.7±0.5%	6.4±0.5%	12.0±0.3 ns	16.2±1.6 ns	11.2±0.4 ns	15.0±0.6 ns	23.1±0.6 ns	14.7±0.5 ns	24.4±1.2 ns
JQ1	4.90^2	12.7±0.4%	11.8±0.5%	12.4±0.3%	10.5±0.3%	3.7±0.3%	12.8±0.5%	4.6±0.5%	15.4±0.4 ns	22.2±1.9 ns	14.4±0.6 ns	19.5±0.8 ns	35.3±1.1 ns	18.4±0.5 ns	34.0±2.1 ns
Linezolid	0.70^2	11.7±0.4%	11.2±0.6%	11.5±0.3%	9.3±0.3%	2.9±0.4%	11.8±0.4%	3.4±0.4%	20.4±0.5 ns	28.5±2.4 ns	18.9±0.8 ns	26.7±1.0 ns	54.5±2.0 ns	24.4±0.8 ns	55.5±3.1 ns

Lisinopril	-1.22[1]	15.0± 0.4%	14.0± 0.5%	14.5± 0.3%	12.4± 0.3%	4.8± 0.4%	14.7± 0.4%	5.4± 0.5%	244.5± 8.9 ns	353.6± 37.7 ns	227.8± 8.4 ns	305.8± 14.6 ns	486.8± 14.4 ns	304.0± 10.8 ns	521.8± 22.9 ns
MZ1	5.00[2]	7.9± 0.3%	7.6± 0.4%	7.5± 0.3%	6.2± 0.3%	1.6± 0.2%	7.9± 0.4%	2.0± 0.3%	25.5± 0.5 ns	35.5± 3.0 ns	24.1± 1.2 ns	34.1± 1.2 ns	80.1± 3.9 ns	30.9± 1.0 ns	79.4± 6.1 ns
Merimepodib	2.10[2]	10.0± 0.3%	9.7± 0.4%	9.7± 0.2%	8.1± 0.3%	2.8± 0.3%	9.9± 0.4%	3.2± 0.3%	20.1± 0.5 ns	27.7± 2.7 ns	18.7± 0.7 ns	26.0± 1.1 ns	47.2± 1.6 ns	24.4± 0.8 ns	48.9± 2.5 ns
Metformin	-1.30[2]	23.7± 0.6%	22.0± 0.7%	22.1± 0.4%	19.1± 0.7%	5.8± 0.6%	22.3± 0.8%	6.9± 0.8%	184.2± 6.1 ns	267.8± 31.0 ns	178.0± 6.6 ns	236.6± 11.6 ns	477.9± 18.6 ns	238.3± 8.3 ns	481.8± 28.0 ns
Midostaurin	4.80[2]	17.5± 0.4%	17.3± 0.6%	16.8± 0.3%	14.9± 0.3%	5.8± 0.5%	17.0± 0.5%	6.5± 0.6%	10.9± 0.3 ns	14.5± 1.5 ns	10.3± 0.3 ns	13.4± 0.6 ns	22.4± 0.7 ns	13.5± 0.4 ns	23.7± 1.1 ns
Migalastat	-2.30[2]	21.7± 0.6%	22.1± 0.7%	20.5± 0.5%	17.8± 0.5%	6.1± 0.6%	21.0± 0.8%	7.1± 0.8%	1.9± 0.1 µs	2.6± 0.3 µs	1.8± 0.1 µs	2.4± 0.1 µs	4.3± 0.2 µs	2.4± 0.1 µs	4.5± 0.2 µs
Mycophenolic acid	3.20[2]	12.5± 0.4%	12.1± 0.6%	11.8± 0.3%	9.8± 0.4%	2.9± 0.3%	12.2± 0.5%	3.3± 0.4%	15.7± 0.3 ns	21.7± 1.7 ns	15.1± 0.6 ns	21.0± 0.8 ns	45.2± 2.0 ns	19.5± 0.6 ns	47.5± 3.1 ns
Nafamostat	2.00[2]	12.3± 0.3%	12.0± 0.4%	12.0± 0.2%	10.4± 0.2%	5.2± 0.4%	12.0± 0.3%	5.8± 0.4%	16.1± 0.6 ns	22.0± 2.4 ns	15.0± 0.5 ns	19.8± 1.0 ns	25.5± 0.7 ns	20.0± 0.8 ns	26.9± 1.7 ns
PB28	5.40[2]	11.2± 0.3%	10.6± 0.4%	10.9± 0.2%	9.2± 0.3%	3.6± 0.3%	11.0± 0.3%	4.2± 0.4%	17.7± 0.6 ns	25.0± 2.6 ns	16.4± 0.6 ns	22.4± 1.1 ns	36.0± 1.0 ns	21.6± 0.8 ns	37.7± 1.8 ns
PD-144418	3.50[2]	10.5± 0.3%	10.3± 0.6%	10.1± 0.2%	8.4± 0.3%	3.0± 0.3%	10.2± 0.4%	3.4± 0.3%	19.0± 0.5 ns	25.7± 2.1 ns	17.8± 0.7 ns	24.8± 1.0 ns	43.3± 1.3 ns	23.6± 0.8 ns	45.8± 2.2 ns

PS3061	7.29[2]	8.8±0.3%	8.6±0.4%	8.5±0.2%	7.2±0.2%	2.7±0.2%	8.8±0.4%	3.3±0.3%	22.7±0.6 ns	31.3±2.7 ns	21.2±0.9 ns	28.9±1.1 ns	48.1±1.5 ns	27.5±0.8 ns	47.0±2.9 ns
Pevonedistat	1.70[2]	11.3±0.3%	10.6±0.4%	11.1±0.3%	9.1±0.3%	3.2±0.3%	11.3±0.4%	3.7±0.4%	17.9±0.5 ns	25.6±2.5 ns	16.5±0.6 ns	23.2±1.0 ns	42.1±1.4 ns	21.4±0.7 ns	43.1±2.2 ns
Ponatinib	4.10[2]	10.6±0.3%	9.8±0.4%	10.3±0.2%	8.6±0.3%	3.0±0.3%	10.5±0.3%	3.4±0.4%	18.8±0.6 ns	27.2±2.7 ns	17.4±0.6 ns	24.1±1.1 ns	43.1±1.4 ns	22.9±0.8 ns	45.9±2.1 ns
RS-PPCC	3.50[2]	8.9±0.4%	8.8±0.6%	8.6±0.3%	6.8±0.3%	1.5±0.2%	9.2±0.5%	1.9±0.3%	22.6±0.3 ns	30.4±2.1 ns	21.0±1.1 ns	30.7±1.0 ns	87.3±5.2 ns	26.2±0.8 ns	81.2±8.9 ns
RVX-208	2.30[2]	10.4±0.3%	10.5±0.5%	10.1±0.2%	8.6±0.2%	3.4±0.3%	10.1±0.4%	4.0±0.4%	19.1±0.5 ns	25.3±2.3 ns	17.9±0.7 ns	24.3±1.0 ns	38.5±1.2 ns	23.8±0.8 ns	39.3±2.3 ns
Rapamycin	6.00[2]	5.2±0.3%	5.4±0.4%	5.2±0.3%	3.8±0.3%	0.5±0.1%	5.8±0.4%	0.9±0.2%	39.3±0.8 ns	50.4±3.0 ns	35.6±2.7 ns	56.1±2.3 ns	246.4±27.5 ns	42.4±1.6 ns	183.3±37.7 ns
Remdesivir	1.90[2]	10.4±0.3%	10.1±0.5%	10.2±0.3%	8.3±0.3%	2.4±0.3%	10.7±0.4%	2.9±0.4%	19.3±0.4 ns	26.6±2.2 ns	17.9±0.9 ns	25.4±0.9 ns	56.2±2.4 ns	22.6±0.7 ns	55.2±3.8 ns
Ribavirin	-1.85[1]	15.0±0.5%	14.6±0.7%	15.1±0.5%	12.0±0.5%	3.6±0.4%	15.7±0.7%	4.5±0.6%	1.0±0.0 µs	1.4±0.1 µs	898.3±41.6 ns	1.3±0.0 µs	2.6±0.1 µs	1.2±0.0 µs	2.5±0.2 µs
Ruxolitinib	2.10[2]	11.2±0.4%	10.8±0.6%	11.1±0.4%	8.8±0.4%	2.1±0.3%	11.7±0.5%	2.8±0.4%	17.8±0.3 ns	24.5±1.8 ns	16.3±0.8 ns	23.7±0.8 ns	61.9±3.3 ns	20.5±0.6 ns	57.3±5.2 ns
S-verapamil	3.80[2]	11.5±0.4%	11.1±0.5%	11.2±0.3%	9.1±0.3%	2.5±0.3%	11.6±0.5%	3.1±0.4%	17.2±0.4 ns	23.6±2.1 ns	16.0±0.7 ns	22.6±0.8 ns	52.3±2.4 ns	20.4±0.6 ns	51.2±3.7 ns

Compound														
Sanglifehrin A	7.30[2]	6.5±0.2%	6.4±0.3%	6.3±0.2%	5.0±0.2%	1.5±0.2%	6.6±0.3%	1.8±0.2%	31.3±0.6 ns	42.4±3.7 ns	29.2±1.5 ns	41.9±1.5 ns	89.8±3.7 ns	37.2±1.2 ns	89.2±6.1 ns
Sapanisertib	1.70[2]	12.1±0.4%	11.9±0.6%	11.4±0.3%	9.8±0.3%	3.6±0.3%	11.8±0.5%	4.2±0.4%	16.6±0.4 ns	22.5±1.8 ns	16.0±0.6 ns	21.4±0.7 ns	37.4±1.2 ns	20.5±0.6 ns	38.1±2.1 ns
Silmitasertib	4.40[2]	14.4±0.4%	14.5±0.6%	14.4±0.4%	11.8±0.3%	3.8±0.4%	15.2±0.5%	4.8±0.6%	13.5±0.4 ns	17.8±1.6 ns	12.2±0.5 ns	17.2±0.7 ns	34.8±1.5 ns	15.3±0.5 ns	32.7±2.3 ns
TMCB	4.40[2]	11.4±0.5%	11.6±0.6%	10.9±0.3%	8.8±0.4%	1.9±0.3%	11.2±0.6%	2.3±0.5%	17.3±0.2 ns	22.7±1.8 ns	16.4±0.7 ns	23.6±0.8 ns	68.5±5.0 ns	21.2±0.8 ns	69.2±9.0 ns
Ternatin 4	4.40[2]	10.7±0.3%	10.2±0.4%	10.2±0.3%	8.6±0.3%	2.8±0.3%	10.5±0.4%	3.1±0.4%	18.5±0.4 ns	26.1±2.4 ns	17.6±0.8 ns	24.1±0.9 ns	47.2±1.7 ns	22.8±0.7 ns	49.9±2.5 ns
Tigecycline	1.10[2]	9.3±0.3%	8.2±0.4%	8.9±0.2%	7.2±0.3%	2.0±0.2%	9.2±0.4%	2.3±0.3%	23.4±0.6 ns	35.7±3.3 ns	21.9±0.9 ns	31.2±1.3 ns	71.3±3.2 ns	28.5±0.9 ns	74.0±4.8 ns
Tomivosertib	1.30[2]	12.7±0.4%	12.6±0.6%	12.0±0.3%	10.1±0.4%	2.8±0.3%	12.5±0.6%	3.3±0.5%	16.2±0.3 ns	21.9±1.8 ns	15.6±0.6 ns	21.4±0.8 ns	49.2±2.4 ns	20.0±0.6 ns	50.5±3.6 ns
Valproic Acid	2.75[1]	19.7±0.6%	19.9±0.7%	19.3±0.4%	16.2±0.5%	6.2±0.6%	19.6±0.8%	7.0±0.7%	9.6±0.2 ns	12.5±1.2 ns	8.9±0.3 ns	12.3±0.5 ns	21.1±0.7 ns	11.5±0.4 ns	22.2±1.1 ns
Verdinexor	4.10[2]	10.4±0.4%	10.2±0.6%	10.1±0.4%	8.0±0.4%	1.8±0.2%	11.0±0.6%	2.4±0.4%	19.1±0.3 ns	25.9±1.9 ns	17.9±1.0 ns	25.8±0.8 ns	73.4±4.6 ns	21.8±0.7 ns	66.6±7.5 ns
WDB002	6.79[2]	7.3±0.3%	7.3±0.5%	7.1±0.3%	5.6±0.3%	1.5±0.2%	7.5±0.4%	1.8±0.3%	27.5±0.5 ns	36.8±2.6 ns	25.8±1.4 ns	37.2±1.2 ns	87.7±4.2 ns	32.5±1.0 ns	86.3±6.7 ns

Compound	LogP														
XL413	3.29[2]	14.8±0.4%	14.8±0.7%	14.8±0.4%	12.1±0.4%	4.1±0.4%	15.4±0.5%	5.2±0.6%	13.1±0.3 ns	17.3±1.5 ns	11.8±0.5 ns	16.8±0.7 ns	31.6±1.1 ns	15.0±0.5 ns	30.2±2.0 ns
ZINC1775962367	4.44[2]	8.4±0.3%	8.5±0.5%	8.5±0.4%	6.5±0.3%	1.4±0.2%	9.2±0.4%	1.9±0.4%	23.9±0.4 ns	31.6±2.4 ns	21.2±1.3 ns	32.2±1.0 ns	94.3±5.8 ns	26.2±0.8 ns	82.2±9.4 ns
ZINC4326719	2.60[2]	10.8±0.4%	10.9±0.6%	10.8±0.4%	8.6±0.3%	2.4±0.3%	11.5±0.4%	3.3±0.5%	18.3±0.4 ns	24.3±1.9 ns	16.7±0.8 ns	24.1±0.8 ns	55.4±2.4 ns	20.7±0.6 ns	48.0±4.0 ns
ZINC4511851	3.41[2]	13.2±0.4%	13.0±0.6%	12.9±0.3%	10.8±0.3%	3.8±0.3%	13.3±0.5%	4.6±0.6%	14.8±0.4 ns	20.0±1.7 ns	13.7±0.6 ns	18.9±0.7 ns	34.1±1.1 ns	17.7±0.5 ns	33.9±1.9 ns
ZINC95559591	5.33[2]	13.5±0.3%	12.1±0.4%	12.9±0.2%	11.0±0.3%	4.1±0.2%	13.0±0.4%	4.5±0.4%	14.4±0.5 ns	21.6±2.3 ns	13.7±0.5 ns	18.5±0.9 ns	32.1±1.0 ns	18.1±0.6 ns	35.1±1.3 ns
Zotatifin	2.40[2]	10.6±0.4%	10.0±0.5%	10.3±0.4%	8.4±0.3%	2.1±0.3%	10.9±0.4%	2.7±0.4%	18.8±0.4 ns	26.6±2.2 ns	17.4±0.9 ns	24.8±0.9 ns	61.9±3.2 ns	22.0±0.7 ns	58.4±4.9 ns
dBET6	5.00[2]	6.9±0.3%	7.0±0.4%	6.8±0.2%	5.4±0.2%	1.5±0.2%	7.1±0.3%	1.9±0.3%	29.3±0.6 ns	38.8±3.2 ns	27.0±1.3 ns	38.8±1.3 ns	86.2±3.9 ns	34.5±1.1 ns	82.9±6.2 ns

[1] These partition coefficients were taken from PubChem.

[2] These partition coefficients were taken from XLogP3 model [15].

[3] parameters for plasma membrane.

[4] parameters for lysosome membrane.

[5] parameters for Golgi membrane.

[6] parameters for mitochondrial membrane.

[7] parameters for endoplasmic reticulum membrane.

[8] parameters for coronavirus membrane with spike protein.

[9] parameters for coronavirus membrane without spike protein.

BIBLIOGRAPHY

[1] A. Al-Nahain, J. E. Lee, I. In, H. Lee, K. D. Lee, J. H. Jeong, and S. Y. Park. Target Delivery and Cell Imaging Using Hyaluronic Acid-Functionalized Graphene Quantum Dots. *Mol. Pharmaceutics*, 10(10):3736–3744, 2013.

[2] P. F. Almeida and T. E. Thompson. Lateral Diffusion in the Liquid Phases of Dimyristoylphosphatidylcholine/Cholesterol Lipid Bilayers : A Free Volume Analysis. *Biochemistry*, 31(29):6739–6747, 1992.

[3] B. Antonny, L. Vamparys, S. Vanni, R. Gautier, P. Fuchs, C. Etchebest, and G. Drin. Amphipathic Lipid Packing Sensor Motifs: Probing Bilayer Defects with Hydrophobic Residues. *Biophys. J.*, 104(3):575–584, 2013.

[4] P. H. Barry and J. M. Diamond. Effects of Unstirred Layers on Membrane Phenomena. *Physiol. Rev.*, 64(3):763–872, 1984.

[5] M. Beck-Broichsitter, O. M. Merkel, and T. Kissel. Controlled Pulmonary Drug and Gene Delivery Using Polymeric Nano-Carriers. *J. Controlled Release*, 161(2):214–224, 2012.

[6] S. Belouzard, J. K. Millet, B. N. Licitra, and G. R. Whittaker. Mechanisms of Coronavirus Cell Entry Mediated by the Viral Spike Protein. *Viruses*, 4(6):1011–1033, 2012.

[7] D. Bemporad, J. W. Essex, and C. Luttmann. Permeation of Small Molecules Through A Lipid Bilayer: A Computer Simulation Study. *J. Phys. Chem. B*, 108(15):4875–4884, 2004.

[8] P. Blasco, D. S. Patel, O. Engström, W. Im, and G. Widmalm. Conformational Dynamics of the Lipopolysaccharide from Escherichia coli O91 Revealed by Nuclear Magnetic Resonance Spectroscopy and Molecular Simulations. *Biochemistry*, 56(29):3826–3839, 2017.

[9] M. F. Brown, A. A. Ribeiro, and G. D. Williams. New View of Lipid Bilayer Dynamics from 2H and 13C NMR Relaxation Time Measurements. *Proc. Natl. Acad. Sci. U. S. A.*, 80(14):4325–4329, 1983.

[10] P. Chambers, C. R. Pringle, and A. J. Easton. Heptad Repeat Sequences are Located Adjacent to Hydrophobic Regions in Several Types of Virus Fusion Glycoproteins. *J. Gen. Virol.*, 71(12):3075–3080, 1990.

[11] R. Chang and A. Violi. Insights into the Effect of Combustion-Generated Carbon Nanoparticles on Biological Membranes: A Computer Simulation Study. *J. Phys. Chem. B*, 110(10):5073–5083, 2006.

[12] S. Chattopadhyay. Aerosol Generation Using Nanometer Liposome Suspensions for Pulmonary Drug Delivery Applications. *J. Liposome Res.*, 23(4):255–267, 2013.

[13] J. Chen, H. Peng, X. Wang, F. Shao, Z. Yuan, and H. Han. Graphene Oxide Exhibits Broad-Spectrum Antimicrobial Activity Against Bacterial Phytopathogens and Fungal Conidia by Intertwining and Membrane Perturbation. *Nanoscale*, 6(3):1879–1889, 2014.

[14] M. L. Chen, Y. J. He, X. W. Chen, and J. H. Wang. Quantum-Dot-Conjugated Graphene as A Probe for Simultaneous Cancer-Targeted Fluorescent Imaging, Tracking, and Monitoring Drug Delivery. *Bioconjugate Chem.*, 24(3):387–397, 2013.

[15] T. Cheng, Y. Zhao, X. Li, F. Lin, Y. Xu, X. Zhang, Y. Li, R. Wang, and L. Lai. Computation of Octanol-Water Partition Coefficients by Guiding an Additive Nodel with Knowledge. *J. Chem. Inf. Model.*, 47(6):2140–2148, 2007.

[16] J. Comer and K. Tam. Lipophilicity Profiles: Theory and Measurement. *Pharmacokinetic Optimization in Drug Research*, 1:275–304, 2001.

[17] H. Cui, E. Lyman, and G. A. Voth. Mechanism of Membrane Curvature Sensing by Amphipathic Helix Containing Proteins. *Biophys. J.*, 100(5):1271–1279, 2011.

[18] B. Cunningham, J. Shimotake, W. Tamura-Lis, T. Mastran, W.-M. Kwok, J. Kauffman, and L. Lis. The Influence of Ion Species on Phosphatidylcholine Bilayer Structure and Packing. *Chem. Phys. Lipids*, 39:20–30, 1986.

[19] P. Dames, B. Gleich, A. Flemmer, K. Hajek, N. Seidl, F. Wiekhorst, D. Eberbeck, I. Bittmann, C. Bergemann, T. Weyh, L. Trahms, J. Rosenecker, and C. Rudolph. Targeted Delivery of Magnetic Aerosol Droplets to the Lung. *Nat. Nanotechnol.*, 2(8):495–499, 2007.

[20] T. Darden, D. York, and L. Pedersen. Particle Mesh Ewald: An Nlog(N) Method for Ewald Sums in Large Systems. *J. Chem. Phys.*, 98(12):10089–10092, 1993.

[21] F. De Meyer and B. Smit. Effect of Cholesterol on the Structure of a Phospholipid Bilayer. *Proc. Natl. Acad. Sci. U. S. A.*, 106(10):3654–3658, 2009.

[22] G. Duan, Y. Zhang, B. Luan, J. K. Weber, R. W. Zhou, Z. Yang, L. Zhao, J. Xu, J. Luo, and R. Zhou. Graphene-Induced Pore Formation on Cell Membranes. *Sci. Rep.*, 7:42767(November 2016):1–12, 2017.

[23] P. Elvati, E. Baumeister, and A. Violi. Graphene Quantum Dots: Effect of Size, Composition and Curvature on Their Assembly. *RSC Adv.*, 7(29):17704–17710, 2017.

[24] S. E. Feller. Constant Pressure Molecular Dynamics Simulation-the Langevin Piston Method. *J. Chem. Phys.*, 103:4613–4621, 1995.

[25] A. Filippov, G. Orädd, and G. Lindblom. The Effect of Cholesterol on the Lateral Diffusion of Phospholipids in oriented bilayers. *Biophys. J.*, 84(5):3079–3086, 2003.

[26] M. Fujikawa, K. Nakao, R. Shimizu, and M. Akamatsu. Qsar study on permeability of hydrophobic compounds with artificial membranes. *Bioorganic & medicinal chemistry*, 15(11):3756–3767, 2007.

[27] B. K. K. Fung and L. Stryer. Surface Density Determination in Membranes by Fluorescence Energy Transfer. *Biochemistry*, 17(24):5241–5248, 1978.

[28] N. M. Garrido, A. J. Queimada, M. Jorge, E. A. Macedo, and I. G. Economou. 1-Octanol / Water Partition Coefficients of N -Alkanes from Molecular Simulations of Absolute Solvation Free. *J. Chem. Theory Comput.*, 5:2436–2446, 2009.

[29] S. Gelperina, K. Kisich, M. D. Iseman, and L. Heifets. The Potential Advantages of Nanoparticle Drug Delivery Systems in Chemotherapy of Tuberculosis. *Am. J. Respir. Crit. Care Med.*, 172(12):1487–1490, 2005.

[30] D. E. Gordon, G. M. Jang, M. Bouhaddou, J. Xu, K. Obernier, M. J. O'Meara, J. Z. Guo, D. L. Swaney, T. A. Tummino, R. Huettenhain, R. M. Kaake, A. L. Richards, B. Tutuncuoglu, H. Foussard, J. Batra, K. Haas, M. Modak, M. Kim, P. Haas, B. J. Polacco, H. Braberg, J. M. Fabius, M. Eckhardt, M. Soucheray, M. J. Bennett, M. Cakir, M. J. McGregor, Q. Li, Z. Z. C. Naing, Y. Zhou, S. Peng, I. T. Kirby, J. E. Melnyk, J. S. Chorba, K. Lou, S. A. Dai, W. Shen, Y. Shi, Z. Zhang, I. Barrio-Hernandez, D. Memon, C. Hernandez-Armenta, C. J. Mathy, T. Perica, K. B. Pilla, S. J. Ganesan, D. J. Saltzberg, R. Ramachandran, X. Liu, S. B. Rosenthal, L. Calviello, S. Venkataramanan, J. Liboy-Lugo, Y. Lin, S. A. Wankowicz, M. Bohn, P. P. Sharp, R. Trenker, J. M. Young, D. A. Cavero, J. Hiatt, T. L. Roth, U. Rathore, A. Subramanian, J. Noack, M. Hubert, F. Roesch, T. Vallet, B. Meyer, K. M. White, L. Miorin, O. S. Rosenberg, K. A. Verba, D. Agard, M. Ott, M. Emerman, D. Ruggero, A. García-Sastre, N. Jura, M. von Zastrow, J. Taunton, A. Ashworth, O. Schwartz, M. Vignuzzi, C. D'Enfert, S. Mukherjee, M. Jacobson, H. S. Malik, D. G. Fujimori, T. Ideker, C. S. Craik, S. Floor, J. S. Fraser, J. Gross, A. Sali, T. Kortemme, P. Beltrao, K. Shokat, B. K. Shoichet, and N. J. Krogan. A SARS-CoV-2-Human Protein-Protein Interaction Map Reveals Drug Targets and Potential Drug- Repurposing. *BioRxiv*, 2020.

[31] R. J. Gowers, M. Linke, J. Barnoud, T. J. E. Reddy, M. N. Melo, S. L. Seyler, J. Domanski, D. L. Dotson, S. Buchoux, I. M. Kenney, and O. Beckstein. MDAnalysis: A Python Package for the Rapid Analysis of Molecular Dynamics Simulations. *Proc. 15th Python Sci. Conf.*, Scipy:98–105, 2016.

[32] R. Gozalbes, M. Jacewicz, R. Annand, K. Tsaioun, and A. Pineda-Lucena. Qsar-based permeability model for drug-like compounds. *Bioorganic & medicinal chemistry*, 19(8):2615–2624, 2011.

[33] S. E. A. Gratton, P. A. Ropp, P. D. Pohlhaus, J. C. Luft, V. J. Madden, M. E. Napier, and J. M. DeSimone. The Effect of Particle Design on Cellular Internalization Pathways. *Proc. Natl. Acad. Sci. U. S. A.*, 105(33):11613–11618, 2008.

[34] C. A. M. D. Haan and P. J. M. Rottier. Molecular Interactions in the Assembly of Coronaviruses. *Adv. Virus Res.*, 64:165–230, 2005.

[35] T. Harayama and H. Riezman. Understanding the Diversity of Membrane Lipid Composition. *Nat. Rev. Mol. Cell Biol.*, 19(5):281–296, 2018.

[36] W. K. Hastings. Monte Carlo Sampling Methods Using Markov Chains and Their Applications. *Biometrika*, 57(1):97–109, 1970.

[37] W. Hayduk and W. D. Buckley. Effect of Molecular Size and Shape on Diffusivity in Dilute Liquid Solutions. *Chem. Eng. Sci.*, 27(11):1997–2003, 1972.

[38] B. G. Hogue and D. A. Brian. Structural proteins of human respiratory coronavirus OC43. *Virus Res.*, 5:131–144, 1986.

[39] S. E. Horvath and G. Daum. Lipids of mitochondria. *Prog. Lipid Res.*, 52(4):590–614, 2013.

[40] X. Huang, R. Pearce, and Y. Zhang. Computational Design of Peptides to Block Binding of the SARS-CoV-2 Spike Protein to Human ACE2. *bioRxiv*, page 2020.03.28.013607, 2020.

[41] W. Humphrey, A. Dalke, and K. Schulten. VMD - Visual Molecular Dynamics. *J. Mol. Graphics*, 14(1):33–38, 1996.

[42] W. C. Hung, M. T. Lee, F. Y. Chen, and H. W. Huang. The Condensing Effect of Cholesterol in Lipid Bilayers. *Biophys. J.*, 92(11):3960–3967, 2007.

[43] B. B. Issack and G. H. Peslherbe. Effects of Cholesterol on the Thermodynamics and Kinetics of Passive Transport of Water Through Lipid Membranes. *J. Phys. Chem. B*, 119(29):9391–9400, 2015.

[44] Y. Jing, Y. Zhu, X. Yang, J. Shen, and C. Li. Ultrasound-Triggered Smart Drug Release from Multifunctional Core-Shell Capsules One-Step Fabricated by Coaxial Electrospray Method. *Langmuir*, 27(3):1175–1180, 2011.

[45] S. Jo, T. Kim, V. G. Iyer, and W. Im. CHARMM-GUI: A Web-Based Graphical User Interface for CHARMM. *J. Comput. Chem.*, 29(1):1859–1865, 2008.

[46] J. B. Klauda, R. M. Venable, J. A. Freites, J. W. O. Connor, D. J. Tobias, C. Mondragon-ramirez, I. Vorobyov, A. D. Mackerell, and R. W. Pastor. Update of the CHARMM All-Atom Additive Force Field for Lipids: Validation on Six Lipid Types. *J. Phys. Chem. B*, 2:7830–7843, 2010.

[47] A. Laio and M. Parrinello. Escaping free-energy minima. *Proc. Natl. Acad. Sci. U. S. A.*, 99(20):12562–12566, 2002.

[48] P. R. Leroueil, S. A. Berry, K. Duthie, G. Han, V. M. Rotello, D. Q. McNerny, J. R. Baker, B. G. Orr, and M. M. B. Holl. Wide Varieties of Cationic Nanoparticles Induce Defects in Supported Lipid Bilayers. *Nano Lett.*, 8(2):420–424, 2008.

[49] L. Liang, Z. Kong, Z. Kang, H. Wang, L. Zhang, and J. W. Shen. Theoretical Evaluation on Potential Cytotoxicity of Graphene Quantum Dots. *ACS Biomater. Sci. Eng.*, 2(11):1983–1991, 2016.

[50] C. A. Lipinski, F. Lombardo, B. W. Dominy, and P. J. Feeney. Experimental and computational approaches to estimate solubility and permeability in drug discovery and development settings. *Advanced drug delivery reviews*, 23(1-3):3–25, 1997.

[51] C. Liu, P. Elvati, S. Majumder, Y. Wang, A. P. Liu, and A. Violi. Predicting the Time of Entry of Nanoparticles in Lipid Membranes. *ACS Nano*, 13(9):10221–10232, 2019.

[52] J. J. Liu, X. L. Zhang, Z. X. Cong, Z. T. Chen, H. H. Yang, and G. N. Chen. Glutathione-Functionalized Graphene Quantum Dots as Selective Fluorescent Probes for Phosphate-Containing Metabolites. *Nanoscale*, 5(5):1810–1815, 2013.

[53] Q. Liu, B. Guo, Z. Rao, B. Zhang, and J. R. Gong. Strong Two-Photon-Induced Fluorescence from Photostable, Biocompatible Nitrogen-Doped Graphene Quantum Dots for Cellular and Deep-Tissue Imaging. *Nano Lett.*, 13(6):2436–2441, 2013.

[54] Z. Liu, J. T. Robinson, X. Sun, and H. Dai. PEGylated Nano-Graphene Oxide for Delivery of Water Insoluble Cancer Drugs - Supplementary Information. *J. Am. Chem. Soc.*, 130(33):10876–10877, 2008.

[55] R. J. Loncharich, B. R. Brooks, and R. W. Pastor. Langevin Dynamics of Peptides: the Frictional Dependence of Isomerization Rates of *N*-Acetylalanyl-*N'*–Methylamide. *Biopolymers*, 32(5):523–535, 1992.

[56] D. Luo and S. Mark, W. Synthetic DNA Delivery Systems. *Nat. Biotechnol.*, 18:33–37, 2000.

[57] A. D. MacKerell, D. Bashford, M. Bellott, R. L. Dunbrack, J. D. Evanseck, M. J. Field, S. Fischer, J. Gao, H. Guo, S. Ha, D. Joseph-McCarthy, L. Kuchnir, K. Kuczera, F. T. K. Lau, C. Mattos, S. Michnick, T. Ngo, D. T. Nguyen, B. Prodhom, W. E. Reiher, B. Roux, M. Schlenkrich, J. C. Smith, R. Stote, J. Straub, M. Watanabe, J. Wiórkiewicz-Kuczera, D. Yin, and M. Karplus. All-Atom Empirical Potential for Molecular Modeling and Dynamics Studies of Proteins. *J. Phys. Chem. B*, 102(18):3586–3616, 1998.

[58] S. Majumder, J. Garamella, Y. L. Wang, M. Denies, V. Noireaux, and A. P. Liu. Cell-Sized Mechanosensitive and Biosensing Compartment Programmed with DNA. *Chem. Commun.*, 53(53):7349–7352, 2017.

[59] S. S. Mansy. Membrane Transport in Primitive Cells. *Cold Spring Harb. Perspect. Biol.*, 2(8), 2010.

[60] K. Martyna, Tobias. Constant Pressure Molecular Dynamics Algorithms. *J. Chem. Phys.*, 101(September):4177–4189, 1994.

[61] J. C. Mathai, S. Tristram-Nagle, J. F. Nagle, and M. L. Zeidel. Structural Determinants of Water Permeability Through the Lipid Membrane. *J. Gen. Physiol.*, 131(1):69–76, 2008.

[62] H. Meyer. Which Characteristic of the Anesthetic Causes Its Narcotic Effect? (translated from German). *Arch. für Exp. Pathol. und Pharmakologie*, 42:109–118, 1899.

[63] P. Meylan, WM; Howard. Atom/Fragment Contribution Method for Estimating Octanol-Water Partition Coefficients. *J. Pharm. Sci.*, 84(1):83–92, 1995.

[64] N. Michaud-Agrawal, E. J. Denning, T. B. Woolf, and O. Beckstein. MDAnalysis: A Toolkit for the Analysis of Molecular Dynamics Simulations. *J. Comput. Chem.*, 32(10):2319–2327, 2011.

[65] S. Mitragotri, P. A. Burke, and R. Langer. Overcoming the Challenges in Administering Biopharmaceuticals: Formulation and Delivery Strategies. *Nat. Rev. Drug Discovery*, 13(9):655–672, 2014.

[66] S. Mitragotri, M. E. Johnson, D. Blankschtein, and R. Langer. An Analysis of the Size Selectivity of Solute Partitioning, Diffusion, and Permeation Across Lipid Bilayers. *Biophys. J.*, 77(3):1268–1283, 1999.

[67] I. Moriguchi, H. Shuichi, Q. Liu, I. Nakagome, and Y. Matsushita. Simple Method of Calculating Octanol/Water Partition Coefficient. *Chem. Pharm. Bull.*, 40(1):127–130, 1992.

[68] J. F. Nagle, J. C. Mathai, M. L. Zeidel, and S. Tristram-Nagle. Theory of Passive Permeability Through Lipid Bilayers. *J. Gen. Physiol.*, 131(1):77–85, 2008.

[69] J. F. Nagle and S. Tristram-Nagle. Structure of Lipid Bilayers. *Biochim. Biophys. Acta - Rev. Biomembr.*, 1469(3):159–195, 2000.

[70] S. Ong, H. Liu, and C. Pidgeon. Immobilized-Artificial-Membrane Chromatography: Measurements of Membrane Partition Coefficient and Predicting Drug Membrane Permeability. *J. Chromatogr. A,*, 728:113–128, 1996.

[71] E. Overton. On the General Osmotic Properties of the Cell, Their Probable Origin,and Their Significance for Physiology (translated from German). *Vierteljahresschr. Naturforsch. Ges. Zürich*, 44:88–135, 1899.

[72] J. Pan, T. T. Mills, S. Tristram-Nagle, and J. F. Nagle. Cholesterol Perturbs Lipid Bilayers Nonuniversally. *Phys. Rev. Lett.*, 100(19):1–4, 2008.

[73] G. Parisio, M. Stocchero, and A. Ferrarini. Passive Membrane Permeability: Beyond the Standard Solubility-Diffusion Model. *J. Chem. Theory Comput.*, 9(12):5236–5246, 2013.

[74] S. Paula, A. Volkov, and D. Deamer. Permeation of halide anions through phospholipid bilayers cccurs by the solubility-diffusion mechanism. *Biophysical journal*, 74(1):319–327, 1998.

[75] L. Peliti and S. Leibler. Effects of Thermal Fluctuations on Systems with Small Surface Tension. *Phys. Rev. Lett.*, 54(15):1690–1693, 1985.

[76] J. C. Phillips, R. Braun, W. Wang, J. Gumbart, E. Tajkhorshid, E. Villa, C. Chipot, R. D. Skeel, L. Kalé, and K. Schulten. Scalable Molecular Dynamics with NAMD. *J. Comput. Chem.*, 26(16):1781–1802, 2005.

[77] E. M. Pridgen, F. Alexis, and O. C. Farokhzad. Polymeric Nanoparticle Drug Delivery Technologies for Oral Delivery Applications. *Expert Opin. Drug Delivery*, 12(9):1459–1473, 2015.

[78] A. E. Rabideau and B. L. Pentelute. Delivery of Non-Native Cargo into Mammalian Cells Using Anthrax Lethal Toxin. *ACS Chem. Biol.*, 11(6):1490–1501, 2016.

[79] K. A. Russ, P. Elvati, T. L. Parsonage, A. Dews, J. A. Jarvis, M. Ray, B. Schneider, P. J. Smith, P. T. Williamson, A. Violi, and M. A. Philbert. C60 Fullerene Localization and Membrane Interactions in RAW 264.7 Immortalized Mouse Macrophages. *Nanoscale*, 8(7):4134–4144, 2016.

[80] J. P. Ryckaert, G. Ciccotti, and H. J. Berendsen. Numerical Integration of the Cartesian Equations of Motion of A System with Constraints: Molecular Dynamics of N-Alkanes. *J. Comput. Phys.*, 23(3):327–341, 1977.

[81] B. J. Schulz, K. Binder, M. Müller, and D. P. Landau. Avoiding Boundary Effects in Wang-Landau Sampling. *Phys. Rev. E*, 67(6):2, 2003.

[82] W. Shi, H. Fan, S. Ai, and L. Zhu. Preparation of Fluorescent Graphene Quantum Dots from Humic Acid for Bioimaging Application. *New J. Chem.*, 39(9):7054–7059, 2015.

[83] J. D. Smith, L. D. Morton, and B. D. Ulery. Nanoparticles as Synthetic Vaccines. *Curr. Opin. Biotechnol.*, 34:217–224, 2015.

[84] B. Song, H. Yuan, C. J. Jameson, and S. Murad. Role of Surface Ligands in Nanoparticle Permeation Through A Model Membrane: A Coarse-Grained Molecular Dynamics Simulations Study. *Mol. Phys.*, 110(18):2181–2195, 2012.

[85] H. Sun, N. Gao, K. Dong, J. Ren, and X. Qu. Graphene Quantum Dots-Band-Aids Used for Wound Disinfection. *ACS Nano*, 8(6):6202–6210, 2014.

[86] N. Suzuki, Y. Wang, P. Elvati, Z.-B. Qu, K. Kim, S. Jiang, E. Baumeister, J. Lee, B. Yeom, J. H. Bahng, J. Lee, A. Violi, and N. A. Kotov. Chiral Graphene Quantum Dots. *ACS Nano*, 10(2):1744–1755, 2016.

[87] I. V. Tetko and V. Y. Tanchuk. Application of Associative Neural Networks for Prediction of Lipophilicity in ALOGPS 2.1 Program. *J. Chem. Inf. Comput. Sci.*, 42(5):1136–1145, 2002.

[88] Z. Tian, X. Yao, K. Ma, X. Niu, J. Grothe, Q. Xu, L. Liu, S. Kaskel, and Y. Zhu. Metal–Organic Framework/Graphene Quantum Dot Nanoparticles Used for Synergistic Chemo- and Photothermal Therapy. *ACS Omega*, 2(3):1249–1258, 2017.

[89] V. P. Torchilin. Multifunctional, Stimuli-Sensitive Nanoparticulate Systems for Drug Delivery. *Nat. Rev. Drug Discovery*, 13(11):813–827, 2014.

[90] J. Torrie, G. M Valleau. Nonphysical Sampling Distributions in Monte Carlo Free-Energy Estimation: Umbrella Sampling. *J. Comput. Phys.*, 23:187, 1977.

[91] Y. Tu, M. Lv, P. Xiu, T. Huynh, M. Zhang, M. Castelli, Z. Liu, Q. Huang, C. Fan, H. Fang, and R. Zhou. Destructive Extraction of Phospholipids from Escherichia Coli Membranes by Graphene Nanosheets. *Nat. Nanotechnol.*, 8(8):594–601, 2013.

[92] P. Vader, E. A. Mol, G. Pasterkamp, and R. M. Schiffelers. Extracellular Vesicles for Drug Delivery. *Adv. Drug Delivery Rev.*, 106:148–156, 2016.

[93] S. Vaidyanathan, K. B. Anderson, R. L. Merzel, B. Jacobovitz, M. P. Kaushik, C. N. Kelly, M. A. Van Dongen, C. A. Dougherty, B. G. Orr, and M. M. Banaszak Holl. Quantitative Measurement of Cationic Polymer Vector and Polymer-PDNA Polyplex Intercalation into the Cell Plasma Membrane. *ACS Nano*, 9(6):6097–6109, 2015.

[94] L. Vamparys, R. Gautier, S. Vanni, W. D. Bennett, D. P. Tieleman, B. Antonny, C. Etchebest, and P. F. Fuchs. Conical Lipids in Flat Bilayers Induce Packing Defects Similar to that Induced by Positive Curvature. *Biophys. J.*, 104(3):585–593, 2013.

[95] I. L. van Genderen, G. J. Godeke, P. J. M. Rottier, and G. van Meer. The Phospholipid Composition of Enveloped Viruses Depends on the Intracellular Membrane through Which They Bud. *Biochem. Soc. Trans.*, 23:523–526, 1995.

[96] J. E. Vance and D. E. Vance. *Biochemistry of Lipids, Lipoproteins and Membranes*. Elsevier, 2008.

[97] K. Vanommeslaeghe, E. Hatcher, C. Acharya, S. Kundu, S. Zhong, J. Shim, E. Darian, O. Guvench, P. Lopes, I. Vorobyov, and A. D. Mackerell. CHARMM General Force Field: A Force Field for Drug-Like Molecules Compatible with the CHARMM All-Atom Additive Biological Force Fields. *J. Comput. Chem.*, 31(4):671–690, 2010.

[98] K. Vanommeslaeghe and A. D. MacKerell. Automation of the CHARMM General Force Field (CGenFF) I: Bond Perception and Atom Typing. *J. Chem. Inf. Model.*, 52(12):3144–3154, 2012.

[99] S. L. Veatch and S. L. Keller. Seeing Spots: Complex Phase Behavior in Simple Membranes. *Biochim. Biophys. Acta - Mol. Cell Res.*, 1746(3):172–185, 2005.

[100] R. M. Venable, A. Krämer, and R. W. Pastor. Molecular dynamics simulations of membrane permeability. *Chemical reviews*, 119(9):5954–5997, 2019.

[101] S. V. Verstraeten, L. V. Nogueira, S. Schreier, and P. I. Oteiza. Effect of Trivalent Metal Ions on Phase Separation and Membrane Lipid Packing: Role in Lipid Peroxidation. *Arch. Biochem. Biophys.*, 338(1):121–127, 1997.

[102] J. S. Wadia, R. V. Stan, and S. F. Dowdy. Transducible TAT-HA Fusogenic Peptide Enhances Escape of TAT-Fusion Proteins After Lipid Raft Macropinocytosis. *Nat. Med.*, 10(3):310–315, 2004.

[103] v. d. S. Walt, J. L. Sch, J. Nunez-iglesias, Francois Boulogne, J. D. Warner, N. Yager, E. Gouillart, and T. Yu. scikit-Image : Image Processing in Python. *PeerJ*, 2e(453):1–18, 2014.

[104] F. Wohnsland and B. Faller. High-Throughput Permeability PH Profile and High-Throughput Alkane/Water Log P with Artificial Membranes. *J. Med. Chem.*, 44(6):923–930, 2001.

[105] D. Wrapp, N. Wang, K. S. Corbett, J. A. Goldsmith, C. L. Hsieh, O. Abiona, B. S. Graham, and J. S. McLellan. Cryo-EM Structure of the 2019-nCoV Spike in the Prefusion Conformation. *Science*, 367(6483):1260–1263, 2020.

[106] T.-x. Xiang. Translational diffusion in lipid bilayers: dynamic free-volume theory and molecular dynamics simulation. *The Journal of Physical Chemistry B*, 103(2):385–394, 1999.

[107] T. X. Xiang and B. D. Anderson. Phospholipid Surface Density Determines the Partitioning and Permeability of Acetic Acid in DMPC:cholesterol Bilayers. *J. Membr. Biol.*, 148(2):157–167, 1995.

[108] T. X. Xiang and B. D. Anderson. Permeability of Acetic Acid Across Gel and Liquid-Crystalline Lipid Bilayers Conforms to Free-Surface-Area Theory. *Biophys. J.*, 72(1):223–237, 1997.

[109] T. X. Xiang and B. D. Anderson. Influence of Chain Ordering on the Selectivity of Dipalmitoylphosphatidylcholine Bilayer Membranes for Permeant Size and Shape. *Biophys. J.*, 75(6):2658–2671, 1998.

[110] L. Zhang, H. Zhu, T. I. Oprea, A. Golbraikh, and A. Tropsha. Qsar modeling of the blood–brain barrier permeability for diverse organic compounds. *Pharmaceutical research*, 25(8):1902, 2008.

[111] H. Zhao, Y. Chang, M. Liu, S. Gao, H. Yu, and X. Quan. A Universal Immunosensing Strategy Based on Regulation of the Interaction Between Graphene and Graphene Quantum Dots. *Chem. Commun.*, 49(3):234–236, 2013.

[112] F. Zocher, D. Van Der Spoel, P. Pohl, and J. S. Hub. Local Partition Coefficients Govern Solute Permeability of Cholesterol-Containing Membranes. *Biophys. J.*, 105(12):2760–2770, 2013.

[113] I. Zucker, J. R. Werber, Z. S. Fishman, S. M. Hashmi, U. R. Gabinet, X. Lu, C. O. Osuji, L. D. Pfefferle, and M. Elimelech. Loss of Phospholipid Membrane Integrity Induced by Two-Dimensional Nanomaterials. *Environ. Sci. Technol. Lett.*, 4(10):404–409, 2017.

[114] J. A. Zuris, D. B. Thompson, Y. Shu, J. P. Guilinger, J. L. Bessen, J. H. Hu, M. L. Maeder, J. K. Joung, Z. Y. Chen, and D. R. Liu. Cationic Lipid-Mediated Delivery of Proteins Enables Efficient Protein-Based Genome Editing *in Vitro* and *in Vivo*. *Nat. Biotechnol.*, 33(1):73–80, 2015.